

Tobias Schorr

Assessing the Potential of
Cirrus Cloud Thinning
through Cloud Chamber Experiments
and Parcel Model Simulations

Assessing the Potential of Cirrus Cloud Thinning through Cloud Chamber Experiments and Parcel Model Simulations

Zur Erlangung des akademischen Grades eines
DOKTORS DER NATURWISSENSCHAFTEN (Dr. rer. nat.)
von der KIT-Fakultät für Physik des
Karlsruher Instituts für Technologie (KIT)
angenommene

DISSERTATION

von

M.Sc. Tobias Schorr

1. Referent:

Prof. Dr. Thomas Leisner

2. Korreferentinnen:

Prof. Dr. Corinna Hoose

Ass. Prof. Dr. Isabelle Steinke

Tag der mündlichen Prüfung:

26.01.2024

Abstract

Cirrus cloud thinning (CCT) is a climate engineering approach to achieve regional cooling by reducing the coverage of effectively warming cirrus clouds. Seeding with ice-nucleating particles (INPs) would affect the natural cirrus cloud formation process and is expected to change the cloud properties to a thinner cloud with a shorter lifetime [51]. With cirrus clouds having a warming effect (on average), diminishing these clouds could lead to a surface cooling. The Arctic could particularly benefit from such an intervention, due to regional feedback effects.

In this work cloud chamber experiments and parcel model simulations on CCT are presented. These results contribute to a better understanding of the competition between heterogeneous and homogeneous freezing and will therefore support a more rigorous evaluation of CCT effectiveness.

In our cloud chamber studies, CCT effectiveness is probed by investigating the competition between homogeneous freezing of sulfuric acid solution droplets and heterogeneous ice nucleation by three different seeding agents, i.e. fumed silica, quartz and calcium carbonate. These cloud chamber experiments show that CCT effectiveness (i.e. minimizing the total ice crystal number concentration) is dependent on the ambient temperature and the concentration of the seeding aerosol.

The Lagrangian parcel model MAID (Model for Aerosol and Ice Dynamics) is validated against our experimental results and used to further analyze CCT effectiveness beyond the experimentally accessible parameter space. As part of this work, the model was improved and expanded by a new heterogeneous freezing scheme, internally calculated trajectories and the representation of gravity wave driven fluctuations. After validation we conduct atmospheric CCT simulations with smaller seeding concentrations and slower updraft velocities along adiabatic updraft trajectories. The results show regimes of optimal seeding conditions, as well as regimes with the opposite effect (overseeding). If the updraft trajectories are superimposed with gravity wave driven fluctuations, the characteristics of those regimes become less distinct and the effect of CCT is significantly reduced.

Our results underline the complexity of CCT effectiveness and highlight the sensitivity with regard to variations of the seeding concentration, updraft velocity and gravity wave fluctuations. Due to the strong impact and statistical nature of gravity wave fluctuations a controlled application of CCT is challenging. Yet, a statistical analysis of stochastic updraft fluctuations shows thinned cirrus in 20% to 30% of the scenarios with low to moderate seeding. Our model simulations emphasize the importance of the competition between heterogeneous and homogeneous freezing, as well as gravity wave driven updraft fluctuations.

Kurzfassung

Die Ausdünnung von Zirruswolken („cirrus cloud thinning“, CCT) ist ein Ansatz des aktiven Eingriffs in unser Klimasystem („Climate Engineering“), um eine regionale Abkühlung zu bewirken, indem die Bedeckung grundsätzlich wärmender Zirruswolken reduziert wird. Das Einbringen (Seeding) von eiskleierenden Partikeln (INPs) würde den natürlichen Prozess der Zirruswolkenbildung beeinflussen und voraussichtlich die Wolkeneigenschaften in Richtung einer dünneren Wolke mit kürzerer Lebensdauer verändern [51]. Da Zirren (im Mittel) eine wärmende Wirkung haben, könnte die Verminderung dieser Wolken zu einer Abkühlung der Erdoberfläche führen. Die Arktis könnte aufgrund regionaler Rückkopplungseffekte besonders von einem solchen Eingriff profitieren.

In dieser Arbeit werden Wolkenkammerexperimente und Boxmodellsimulationen zu CCT vorgestellt. Die Ergebnisse tragen zu einem besseren Verständnis des Wettbewerbs zwischen heterogenem und homogenem Gefrieren bei und ermöglichen somit eine genauere Bewertung der Wirksamkeit von CCT.

In unseren Wolkenkammerexperimenten wird die Wirksamkeit von CCT untersucht, indem die Konkurrenz zwischen homogenem Gefrieren von Schwefelsäurelösungströpfchen und heterogener Eisbildung durch drei verschiedene Eiskeimtypen, namentlich pyrogene Kieselsäure, Quarz und Kalziumkarbonat, untersucht wird. Diese Wolkenkammerexperimente zeigen, dass die Wirksamkeit von CCT, genauer die Minimierung der Gesamteiskristallzahlkonzentration, von der Umgebungstemperatur und der Konzentration des Impfaerosols abhängt.

Das Lagrange'sche Boxmodell MAID (Model for Aerosol and Ice Dynamics) wird anhand unserer experimentellen Ergebnisse validiert und zur weiteren Analyse der Wirksamkeit von CCT über den experimentell zugänglichen Parameterraum hinaus verwendet. Im Rahmen dieser Arbeit wurde das Modell überarbeitet und um ein neues heterogenes Gefrierschema, intern berechnete Trajektorien und die Darstellung von Schwerewellen getriebenen Fluktuationen erweitert. Nach der Validierung führen wir atmosphärische CCT-Simulationen mit kleineren Seeding-Konzentrationen und langsameren Aufwindgeschwindigkeiten entlang adiabatischer Aufwind-Trajektorien durch. Die Ergebnisse zeigen sowohl Regime mit optimalen Seeding-Bedingungen als auch Regime mit gegenteiligem Effekt (Overseeding). Werden die Aufwindtrajektorien mit von Schwerewellen verursachten Fluktuationen überlagert, verlieren die Merkmale dieser Regime an Deutlichkeit, und die Wirkung von CCT wird erheblich reduziert.

Unsere Ergebnisse unterstreichen die Komplexität der Wirksamkeit von CCT und verdeutlichen dessen Empfindlichkeit bezüglich Variationen der Seeding-Konzentration, Aufwindgeschwindigkeit und Schwerewellenfluktuationen. Aufgrund des starken Einflusses und der statistischen Natur von Schwerewellenfluktuationen ist eine kontrollierte Anwendung von CCT eine Herausforderung. Eine statistische Analyse der Simulationen

mit stochastisch auftretenden Auftriebsfluktuationen zeigt jedoch, dass bei geringem bis mäßigem Seeding 20 bis 30 % der Zirren ausgedünnt werden. Unsere Modellsimulationen unterstreichen die Bedeutung der Konkurrenz zwischen heterogenem und homogenem Gefrieren sowie der von Schwerewellen getriebenen Auftriebsfluktuationen.

Contents

List of Figures	xiv
List of Tables	xv
Glossary	xvii
Acronyms	xix
Symbols	xxi
1 Introduction	1
2 Background	3
2.1 The atmosphere of Earth	3
2.1.1 Atmospheric updraft mechanisms	7
2.2 Ice nucleation of aerosols	9
2.2.1 Homogeneous ice nucleation	10
2.2.2 Heterogeneous ice nucleation	13
2.3 Cirrus clouds	15
2.3.1 Cirrus formation	15
2.3.2 Cirrus properties	17
2.4 Climate engineering: Cirrus cloud thinning	18
2.4.1 The concept of cirrus cloud thinning	18
2.4.2 The potential of cirrus cloud thinning	18
2.4.3 Cirrus cloud thinning during the Arctic winter	21
3 Methods and Procedures	23
3.1 Seeding aerosol types	23
3.2 The AIDA cloud chamber facility and its instrumentation	24
3.2.1 Pump system	25
3.2.2 Temperature measurement	26
3.2.3 Water measurement	26
3.2.4 Depolarization laser SIMONE	27
3.2.5 Optical particle counters	27
3.2.6 Condensation particle counters	28
3.2.7 Aerosol generation instrumentation	28

3.2.8	Aerosol size distribution measurements	30
3.2.9	Filter sampling and ESEM analysis	31
3.2.10	Standard procedure for our AIDA expansion experiments	32
3.3	AIDA campaign overview	33
3.3.1	Parameter space covered by AIDA campaigns	38
3.4	AIDA data analysis	39
3.4.1	Developed analysis software	40
3.4.2	Aerosol size distribution fitting	42
3.4.3	Separation between heterogeneously and homogeneously formed ice	43
3.4.4	Fit of INAS density parameterizations	44
3.4.5	Cirrus thinning effect in cloud chamber experiments	45
3.5	Cloud chamber wall effects	45
4	MAID – Model for Aerosol and Ice Dynamics	49
4.1	Model features	49
4.1.1	Selectable trajectory types	49
4.1.2	Aerosol particle types	50
4.1.3	Freezing mechanisms	51
4.1.4	Trace gas balancing	52
4.1.5	Diabatic effects	53
4.1.6	Sedimentation	53
4.1.7	Gravity wave driven fluctuations	54
4.2	Model history	54
4.2.1	Model development within this work	55
4.3	Model limitations	56
5	Results and Discussion	57
5.1	Aerosol characterization	58
5.1.1	Filter sampling and ESEM images	58
5.1.2	Size distribution analysis	58
5.2	Ice nucleation in AIDA expansion experiments	60
5.2.1	Homogeneous ice nucleation	60
5.2.2	Heterogeneous ice nucleation	62
5.2.3	Cirrus thinning effect in cloud chamber experiments	62
5.3	MAID validation	66
5.3.1	Cloud chamber wall flux parameterization	66
5.3.2	Model validation against AIDA experiments	68
5.3.3	Ability of MAID to simulate CCT	72
5.3.4	Gravity wave forcing effect on homogeneous freezing	73
5.4	MAID: atmospheric scenarios	76
5.4.1	Scenarios with constant updraft velocities	76
5.4.2	Scenarios with updraft velocity variations	80
6	Summary and Outlook	87

Bibliography	89
A General evaluation methods	97
B AIDA wall flux model	103
C MAID validation for different wall flux implementations	113
D Long tables	119

List of Figures

2.1.1	The Earth’s energy budget.	6
2.1.2	Probability density functions for temperature and updraft velocity fluctuations.	9
2.2.1	Change of Gibbs free energy for the formation of a nucleus.	11
2.2.2	Homogeneous nucleation rate and freezing probability as a function of the water activity criterion Δa_w	12
2.4.1	Schematic drawing on the concept of cirrus cloud thinning.	19
3.2.1	Schematics of the AIDA cloud chamber facility (source: KIT/IMK-AAF).	25
3.2.2	Instrumentation for aerosol generation at AIDA	29
3.3.1	Number concentrations of AIDA experiments with pure aerosol populations as a function of start temperature.	39
3.3.2	Parameter space visualization for mixed aerosols.	40
3.4.1	Schematic of the data flow within the developed software frameworks.	41
3.4.2	Fit parameters of lognormal functions fitted to particle size distributions. The established IDL routines were used in the left panel, the new python-based framework <code>psd_analysis</code> was used on the right. The colors in b) match the legend in a). b) shows beside the combined fits (APS+SMPS) also the the fit of only SMPS for fumed silica and the fit of only APS for quartz and calcium carbonate.	42
4.1.1	Decision graph for MAID trajectories.	50
5.0.1	Schematic of the logical structure in the results chapter.	57
5.1.1	ESEM images for fumed silica and calcium carbonate.	58
5.1.2	Aggregated lognormal fit parameters median diameter and geometric standard deviation for different scenarios.	59
5.2.1	Homogeneous freezing onsets as observed in the AIDA experiments.	61
5.2.2	Ice-nucleating active site densities n_s for fumed silica, quartz and calcium carbonate derived from AIDA experiments.	63
5.2.3	Cirrus cloud thinning in AIDA using quartz as seeding aerosol.	64
5.2.4	Cirrus cloud thinning in AIDA for fumed silica and calcium carbonate as seeding aerosol.	65
5.3.1	Fit of wall flux parameterizations according to the fluid dynamic approach.	67
5.3.2	Fit of wall flux parameterizations according to Cotton et al. [13].	68

5.3.3	Aggregated evaluation metrics about the deviation of the total ice crystal number concentration n_{ice} between MAID results and AIDA experiments.	70
5.3.4	Comparison of selected AIDA expansion experiments with MAID simulations using different wall flux implementations.	71
5.3.5	Simulation of the seeding effect as seen in AIDA using MAID.	72
5.3.6	Effect of updraft velocity with fluctuations on homogeneous ice number concentration.	73
5.3.7	Statistics on the set of model runs with updraft perturbation shown in Figure 5.3.6. Plot a) shows the fraction of model runs in which homogeneous freezing occurs. Plot b) shows the distribution of temperature extremes (min, max) for all model runs.	75
5.4.1	The maximum ice crystal number concentration $n_{\text{ice}}^{\text{max}}$ for different starting temperatures.	77
5.4.2	Maximum ice crystal number concentration and maximum ice water content for pure homogeneous scenarios as a function of static updraft velocity.	78
5.4.3	Comparison of maximum ice crystal number concentrations $n_{\text{ice}}^{\text{max}}$ for scenario sets with different starting pressures.	79
5.4.4	Maximum ice saturation ratio for MAID scenarios with static updrafts.	80
5.4.5	Relative deviation of maximum ice crystal number concentration $n_{\text{ice}}^{\text{max}}$ from the non-seeding scenario at $n_{\text{INP}} = 0$.	81
5.4.6	Analysis of the maximum IWC for model run ensembles at starting temperatures 210 K, 220 K and 230 K.	82
5.4.7	The median of quantitative ice metrics based on 50 model runs with updraft fluctuations.	83
5.4.8	Histograms of $n_{\text{ice}}^{\text{max}}$ (left) and IWC_{max} (right) for three run subsets.	85
A.1.1	Sensitivity of the fractional bias.	100
A.2.1	Savitzky-Golay filter example	101
C.0.1	Aggregated evaluation metrics between MAID and AIDA using the fluid dynamic wall flux implementation in the model.	114
C.0.2	Aggregated evaluation metrics between MAID and AIDA using the wall flux implementation according to Cotton et al. [13] in the model.	115
C.0.3	Aggregated evaluation metrics between MAID and AIDA using the wall flux implementation based on the MBW variation in the model.	116
C.0.4	Aggregated evaluation metrics between MAID and AIDA without any water wall flux consideration in the model.	117

List of Tables

3.1.1 Bulk aerosol samples.	24
3.3.1 Instrumentation used at the AIDA facility during the campaign AWICIT01B.	33
3.3.2 Instrumentation used at the AIDA facility during the campaigns AWICIT02 and AWICIT03.	34
3.3.3 Instrumentation used at the AIDA facility during the campaign AWICIT04.	35
3.3.4 Instrumentation used at the AIDA facility during the campaigns AWICIT05 and AWICIT06.	36
3.3.5 Instrumentation used at the AIDA facility during the campaign TROPIC02.	38
5.3.1 Fit parameters for to parameterize the AIDA water and heat wall flux. . .	69
A.1.1 Comparison metrics and their range.	99
D.0.1 Key information of expansion experiments conducted at the AIDA cloud chamber facility.	120
D.0.2 Key information of reference expansion experiments conducted at the AIDA cloud chamber facility.	133

Glossary

AIDA	”Aerosol Interactions and Dynamics in the Atmosphere”. It is the main cloud chamber at IMK-AAF and will be demolished in early 2024.
APeT	AIDA PCI extractive TDL, a device at the AIDA facility to measure the total water content through absorption of a tunable diode laser.
APicT	AIDA PCI in cloud TDL, a device at the AIDA facility to measure the gas water content through absorption of a tunable diode laser.
ESEM	environmental scanning electron microscope
git	A distributed version control system
IDL	A proprietary programming language, ”Interactive Data Language”
MBW	refers to dew point mirrors from the MBW Calibration AG
NAUA	An aerosol chamber at IMK-AAF. The name is derived from the German ”Nach Atomunfall Atmosphäre”, referring historically to its previous use in nuclear science.
NIXE-CAPS	Novel Ice EXpEriment – Cloud and Aerosol Particle Spectrometer, a cloud particle spectrometer from the group of Martina Krämer at Forschungszentrum Jülich, manufactured by DMT
RBG	rotating brush generator
SIMONE	A depolarization laser scattering device at the AIDA facility providing information about the sphericity of aerosol in the chamber
SSPD	small-scale powder disperser, an instrument from TSI Inc.

Acronyms

a. u.	arbitrary units
AAF	Atmospheric Aerosol Research
APS	aerodynamic particle sizer
ASP	aqueous solution particle
CCN	cloud condensation nuclei
CCT	cirrus cloud thinning
CNT	classical nucleation theory
CPC	condensation particle counter
DMA	differential mobility analyzer
FAE	fractional absolute error
FB	fractional bias
FZJ	Forschungszentrum Jülich
GCM	general circulation model
IMK	Institute for Meteorology
INAS	ice-nucleating active site
INP	ice-nucleating particle
IWC	ice water content
KIT	Karlsruhe Institut for Technology
MAE	mean absolute error
MAID	Model for Aerosol and Ice Dynamics
MARE	mean absolute relative error
ME	mean error
MFC	mass flow controller
MNB	mean normalized bias
OCS	carbonyl sulfide
OPC	optical particle counter

PDF	probability density function
PSD	particle size distribution
SMPS	scanning mobility particle sizer
SQL	structured query language
TDL	tunable diode laser
UTLS	upper troposphere / lower stratosphere
WMO	World Meteorological Organization

Symbols

Symbol	Description	Unit (SI)
A_{ae}	Aerosol surface area	m^2
D_x	Diffusion coefficient for molecules of type x	$\text{m}^2 \text{s}^{-1}$
G	Gibbs free energy	J
J	Nucleation rate coefficient	–
L	Laplace distribution	–
M	Molar mass	kg mol^{-1}
N	Buoyancy frequency or Brunt-Väisälä frequency	s^{-1}
P	Probability	–
R_{spec}	Specific gas constant	$\text{J kg}^{-1} \text{K}^{-1}$
R	Universal gas constant	$\text{J mol}^{-1} \text{K}^{-1}$
S_{ice}	Water vapor saturation ratio with respect to ice	–
S_{liq}	Water vapor saturation ratio with respect to liquid water	–
T_g	Gas temperature	K
T_w	Wall temperature	K
T	Temperature	K
V	Volume	m^3
Γ	Dry adiabatic lapse rate	K m^{-1}
γ	Adiabatic coefficient $\gamma = \frac{c_p}{c_v}$	–
ρ	Mass density	kg m^{-3}
\vec{g}	Gravitational acceleration	m s^{-2}
\vec{w}	Vertical wind velocity (updraft)	m s^{-1}
a_w^i	Ice activity	–
a_w	Water activity	–
c_p	Specific heat capacity at constant pressure	$\text{J kg}^{-1} \text{K}^{-1}$
c_v	Specific heat capacity at constant volume	$\text{J kg}^{-1} \text{K}^{-1}$
d	Diameter	m
k_B	Boltzmann constant	J K^{-1}
m	Mass	kg
n_a	Surface area concentration	$\text{m}^2 \text{m}^{-3}$
n_m	Mass concentration	kg m^{-3}
n_n	Number concentration	$\#/ \text{m}^3$

Symbol	Description	Unit (SI)
n_s	Ice-nucleation active site density	$\#/m^2$
p_w	Water vapor partial pressure	Pa
p_x	Partial pressure of a constituent gas x in a mixture	Pa
$p_{w,0}^{ice}$	Water vapor saturation pressure with respect to ice	Pa
$p_{w,0}^{liq}$	Water vapor saturation pressure with respect to liquid water	Pa
$p_{w,0}^{sol}$	Water vapor saturation pressure over an aqueous solution surface	Pa
$p_{x,0}$	Saturation vapor pressure of a constituent gas x in a mixture	Pa
p	Air pressure	Pa
r	mixing ratio	–
r	Radius	m
t	Time	s
z	Elevation / height	m

Chapter 1

Introduction

The consequences of global warming have become increasingly present in the recent years. The year 2023 is until now the warmest year on record [92] and global mean surface temperature anomalies of the last decade show the strongest warming since the beginning of temperature recordings¹. Hence, debates about the need for climate engineering interventions have been intensifying. Climate engineering, describes active interventions into the Earth system with the objective to decrease adverse effects of climate change. Beside unclear governance, uncertainties about benefits, risks and side effects make climate engineering a highly controversial topic.

Cirrus clouds are high altitude ice clouds with a white, fibrous and partially transparent appearance. Their radiative properties are associated with an effective warming, since they don't reflect much of the incoming sunlight, but effectively hold back outgoing thermal radiation. The idea of [Cirrus cloud thinning \(CCT\)](#) is to add ice-nucleating particles to interfere with the natural cloud formation process, which leads to fewer but bigger ice crystals. Bigger ice crystals have a faster sedimentation velocity, causing a shorter cloud lifetime. Thus, successful seeding would lead to an effective cooling effect. However, modeling studies about the effectiveness of [CCT](#) provide ambiguous and partially contradicting assessments [54, 57, 80, 17, 83, 84].

A main difficulty for cirrus cloud modeling is the representation of the competition between different ice nucleation mechanisms. In addition, recent studies suggest a stronger impact of atmospheric mesoscale (tens of centimeters) fluctuations on the dynamics of cirrus cloud formation than assumed earlier [32, 28]. However such small scale fluctuations are typically not represented in global models. In this work we focus on the interplay between cloud freezing mechanisms and updraft velocity fluctuations.

The methods of this work can be classified in two main categories: laboratory experiments in the [AIDA](#) (Aerosol Interaction and Dynamics in the Atmosphere) cloud chamber

¹Compared to measurements between 1980 and 2015.

facility and parcel model simulations using the [Model for Aerosol and Ice Dynamics \(MAID\)](#).

The [AIDA](#) cloud chamber, located at the [Karlsruhe Institut for Technology \(KIT\)](#) operated at temperatures down to below -40°C to -60°C to simulate cirrus cloud formation in the [upper troposphere / lower stratosphere \(UTLS\)](#). The experiments focus on the competition between homogeneous freezing of sulfuric acid solution droplets and heterogeneous freezing of different ice-nucleating particles.

[MAID](#) is a Lagrangian parcel model for the [UTLS](#) and is tailored towards representing ice nucleation and the balancing of trace gases. It was developed by H. Bunz at [KIT/IMK-AAF](#) [11]. Within the scope of this work the code base was modernized and the functionality extended to allow a better representation of cirrus cloud formation. For model validation constrained simulations are conducted to reproduce the cloud chamber experiments. The model is then applied to simulate atmospheric [CCT](#) scenarios, in particular adiabatic atmospheric updraft trajectories and scenarios with gravity wave driven mesoscale fluctuations.

This work is organized as follows:

[Chapter 2](#) provides the scientific background for this work. It gives an overview on the Earth's atmosphere with its constituents and describes the relevant ice nucleation processes. Moreover the formation dynamics of cirrus clouds and the potential of [CCT](#) are emphasized. [Chapter 3](#) contains a description of the applied methods with a focus on the [AIDA](#) cloud chamber experiments. In [chapter 4](#) the [MAID](#) model is presented. The model development within the context of this work is also highlighted there. In [chapter 5](#) the results are shown and discussed. The chapter starts with the experimental results and shows how they are used to validate the model. Subsequently, the results of model [CCT](#) simulations under atmospheric updraft scenarios are presented and discussed.

A summary of the results and the derived conclusions are given in [chapter 6](#). Moreover, suggestions for follow-up studies are provided and potential benefits for other models are outlined.

Chapter 2

Background

This chapter provides the background and physical fundamentals, which are necessary to comprehend the present work.

In [section 2.1](#) relevant constituents and processes in our atmosphere are addressed. It gives an introduction on atmospheric layers, explains the stratospheric background aerosol and describes mechanisms of vertical dynamics in the atmosphere. Mechanisms in the Earth's radiative budget are also briefly addressed.

[Section 2.2](#) provides fundamentals about the mechanisms of ice nucleation. The section especially explains the basics of homogeneous ice formation of aqueous solution droplets and the concept of ice-nucleating active site densities to describe heterogeneous ice nucleation of other aerosol types.

[Section 2.3](#) puts a focus on cirrus clouds, while differentiating between types of different origin. Their microphysical and macrophysical characteristics are discussed, as well as their global appearance. Further their radiative properties and their contribution to the radiative balance are discussed.

[Section 2.4](#) covers the climate engineering approach called *cirrus cloud thinning*. The concept is explained, while narrowing a potential application particularly on the Arctic. Based on previous studies the anticipated potential of cirrus cloud thinning is discussed, showing a wide spread of literature results with partially contradicting conclusions.

2.1 The atmosphere of Earth

Gases

Our planet is covered by an atmosphere containing various constituents. Molecular nitrogen N_2 , molecular oxygen O_2 and carbon dioxide CO_2 provide more than 99 % of

the atmosphere's volume. Other trace gases, such as water vapor, may be prevalent in much smaller concentrations, yet being highly important for atmospheric processes. Those include chemical reactions, particle formation or radiative contributions.

Airborne particles

Besides the molecular constituents the atmosphere also contains airborne particles called aerosols (see [section 2.2](#)). Their size range is within 1 nm and 10 μm and they can originate from various sources. Common types of natural atmospheric aerosols are dust, sea salt, pollen, plant fragments and biological organic compounds [73]. Volcanic eruptions or wildfires can also be strong singular sources of aerosol, while anthropogenic activities are additional sources for airborne particles, such as soot or agricultural dusts. Depending on the particle composition, atmospheric chemical reactions can happen during their lifetime and alter their properties. Atmospheric aerosol interacts with radiation, can play a role in atmospheric chemistry and is crucial for cloud processes.

Hydrometeors

Aerosol particles can act as [cloud condensation nuclei \(CCN\)](#) or [ice-nucleating particle \(INP\)](#) to form a droplet or an ice crystal. Those *activated* particles grow typically to sizes bigger than aerosols and are therefore named hydrometeors. Once a macroscopic ensemble of hydrometeors reaches a significant optical depth we speak of clouds. The formation and sedimentation of hydrometeor water is a major process in the atmospheric water cycle and would not occur without the activation of aerosol particles.

Atmospheric layers

The atmosphere can be divided into vertically stacked layers of different characteristics. The lowest layer is the troposphere where the majority of weather processes take place. This layer is characterized by a strong mixing of air masses and cloud formation, which causes precipitation. The temperature profile has a positive lapse rate, meaning the temperature decreases with increasing height. The troposphere has an altitude up to 10 km to 15 km depending on the latitude and time of year [73].

The tropopause divides the troposphere and the atmospheric layer above, the stratosphere. As defined by the [World Meteorological Organization \(WMO\)](#) the tropopause is located at the lowest altitude at which the lapse rate decreases to 2 K km^{-1} or less and the lapse rate averaged between this altitude and any altitude within the next 2 km does

not exceed 2 K km^{-1} [23]. Its average height is about 16 km at the equator and about 8 km at the poles [73].

The stratosphere reaches a up to $\sim 45\text{ km}$ to 55 km and the temperature increases with height (negative lapse rate). This temperature profile leads to an enhanced vertical stability, which suppresses convection and slows the transport of wet air from the troposphere into the stratosphere. Therefore the stratosphere is extremely dry.

The atmospheric layers above, mesosphere and thermosphere, are beyond the scope of this work and will not be discussed in here.

Stratospheric aerosol

The typical type of aerosol in the stratosphere are sulfuric acid solution particles, often called stratospheric background aerosol. Those [aqueous solution particles \(ASPs\)](#) consist primarily of H_2O with dissolved H_2SO_4 . The main precursor for stratospheric H_2SO_4 is [carbonyl sulfide \(OCS\)](#). It is a relatively stable molecule and well mixed in the troposphere, so it gets also mixed into the stratosphere within a certain rate, where its mixing ratio decreases with altitude [9, section 12]. In the stratosphere the higher amount of ultraviolet radiation leads to photolysis of [OCS](#), which can oxidate to SO_2 [73]. A second important source of SO_2 are volcanic eruptions, which can transport large amounts of SO_2 into the lower or mid-stratosphere. Further oxidation of SO_2 with OH radicales leads to H_2SO_4 . Depending on the stratospheric concentrations of OH typical SO_2 lifetimes are on the order of days to several weeks [40]. Sulfuric acid is highly hygroscopic and forms aqueous solution particles. These stratospheric sulfuric acid solution particles have a lifetime of a couple of years, due to their small size and since their only sink is gravitational sedimentation [45].

The stratospheric aerosol particles are essentially located in the lower stratosphere, in a layer between the tropopause and a height of 30 km to 35 km. It was first discovered by Junge et al. in 1961 and is therefore called the *Junge layer*.

In the stratosphere the sulfuric solution particles are highly concentrated due to the low gas water content (60 to 80 wt% H_2SO_4 [73]). But they also sediment into the upper troposphere where they can equilibrate to mass mixing ratios of ~ 30 to 40 wt% H_2SO_4 . They play an important role for homogeneous freezing and the formation of cirrus clouds in the [UTLS](#), as discussed in [section 2.2.1](#) and [section 2.3](#).

The Earth's energy budget

The Sun's irradiance provides a continuous flux of energy into the Earth's ecosystem. The mean incoming energy flux is described by the solar constant $S_0 = 1360.8(5) \text{ W m}^{-2}$ [37]. Incoming radiation gets scattered, reflected and absorbed in the Earth's atmosphere and on the surface. Absorbed radiation is converted to thermal energy, which results in increased thermal radiation. The balance of incoming and outgoing radiation regulates our planet's temperature and climate.

Both, incoming and outgoing radiation interact with the atmospheric components, respectively. However, optical phenomena, such as scattering and absorption, depend on the wavelength of the involved light. Incoming solar radiation has its peak in the visible spectrum, contains also ultraviolet components and a wide tail into the infrared spectrum. In contrast, terrestrial thermal radiation consists solely of wavelengths in the infrared band. Therefore each atmospheric component can contribute a net warming positive forcing ($\Delta E > 0$) or a net cooling negative forcing ($\Delta E < 0$) to the Earth's radiative budget.

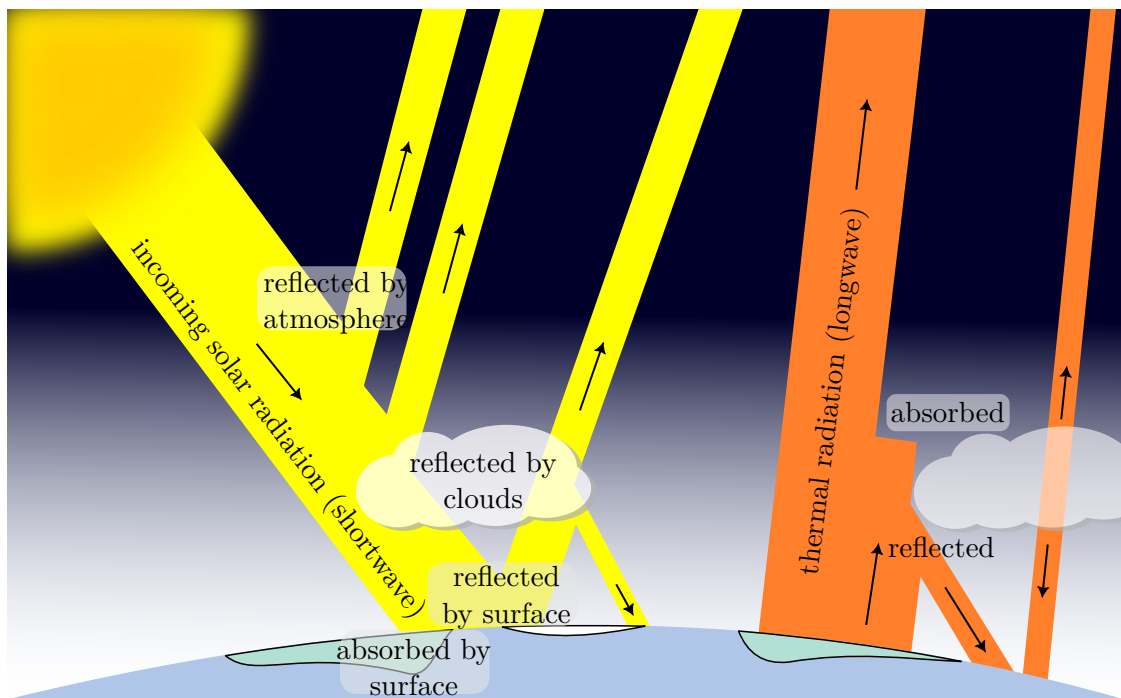


Figure 2.1.1 Schematic visualization of the Earth's energy budget. Only for qualitative discussion, the fluxes are not visualized with quantitatively correct magnitudes.

Figure 2.1.1 visualizes the role of various atmospheric components in the interplay of the radiative budget. A fraction of the incoming solar radiation is absorbed by atmospheric

gases, clouds, and aerosols. The remaining energy reaching the Earth's surface is then either reflected back into space or absorbed. The ability of a surface to reflect light is known as albedo. Snow- or ice-covered surfaces and clouds have a high albedo, whereas dark (e.g. forested) areas or oceans have a low albedo.

The radiative budget is strongly driven by atmospheric components which interact asymmetrical with shortwave incoming radiation and outgoing longwave thermal radiation. A famous example is the greenhouse effect, which is driven by trace gases, such as water vapor, carbon dioxide or methane. Those gases transmit a major fraction of the incoming radiation, but absorb the outgoing thermal radiation, which effectively traps a fraction of the energy in our planetary system.

A similar effect can be considered for clouds. Clouds are capable of reflecting incoming radiation (albedo effect). Yet, at the same time they can prevent thermal radiation from escaping into space. The radiative forcing of most cloud types is negative, so they are effectively cooling the surface. However, an exception are cirrus clouds (see [section 2.3](#)). Their albedo effect towards the incoming solar radiation can typically not outweigh the warming interaction with longwave radiation.

2.1.1 Atmospheric updraft mechanisms

Vertical movement of air, referred to as updraft or downdraft, is a main driver for thermodynamic processes in the atmosphere. The updraft of an air parcel leads to cooling, which in turn can cause other processes, such as nucleation (see [section 2.2](#)). Vertical air movement can have various origins, which lead to different updraft characteristics, respectively.

Frontal lifting can occur when a warm air mass meets another air mass of dense cold air. The warmer air mass can rise over the colder air mass, which results in an updraft at the frontal boundary. Such an updraft can last comparably long and cause slow to moderate updraft velocities w . *Convergence* describes the process when horizontal air flows move towards one another. When they collide the only direction to escape is upwards. *Convective updrafts* can happen when an air parcel takes up heat, which reduces its density. The parcel cools down during its updraft and will rise until it reaches a temperature in equilibrium with its surrounding. Convection can lead to strong updraft velocities w . *Orographic lifts* happen when an air mass moves horizontally over land surfaces with mountains or hills, which force the air towards higher altitudes. Such a scenario can lead to orographic waves, which are stationary waves on the lee side of a topographic barrier (see e.g. [87, section 10.3]).

Another cause of vertical air displacements are (internal) gravity waves [87, section 10.4]. Gravity waves transport momentum from the troposphere to higher atmospheric layers

and can originate from air movement over orographic structures or during convection. For the formation of cirrus clouds the frequency spectrum is important to describe vertical velocity fluctuations in the **UTLS**. Therefore an overview is given in the following.

Gravity waves can have strong amplitudes, compared to synoptic updrafts, and propagate over long distances. Therefore at any coordinate in the atmosphere one must expect (vertical) wind speed fluctuations from a combined spectrum of superimposed internal gravity waves. Using global atmospheric simulations, Barahona, Molod, and Kalesse [4] described the distribution of vertical wind speeds w at the scale being relevant for cirrus formation. They concluded that the standard deviation of the vertical wind speed distribution σ_w is critical for a realistic simulation of cirrus clouds. Podglajen et al. [58] determined the updraft velocities experimentally using data from super pressure balloons, which are able to follow the vertical air motion and resolve a wide range of the frequency spectrum. They derived a **probability density function (PDF)** for vertical wind fluctuations w' , which is close to a (double exponential) Laplace distribution. Kärcher and Podglajen [29] continued on this work and provided a formulation of the gravity wave driven updraft fluctuations w' and the resulting temperature fluctuations T' . The formulation can be integrated into microphysical cloud models. The probability distribution of temperature fluctuations T' is described as a normal distribution

$$N(T', \sigma_T) = \frac{1}{\sqrt{2\pi}\sigma_T} \exp\left(-\frac{T'^2}{2\sigma_T^2}\right) \quad (2.1)$$

with the variance σ_T^2 . The probability distribution of updraft fluctuations w' is approximated with a double-exponential Laplacian

$$L(w', \sigma_w) = \frac{1}{2\mu_w} \exp\left(-\frac{|w'|}{\mu_w}\right) \quad (2.2)$$

with $\sigma_w = \sqrt{2}\mu_w$ and μ_w being the mean value of the updraft speed distribution [29].

A stable atmosphere is fundamental for this approach. Only if an air parcel resides in a stable atmosphere, a vertical displacement leads to a buoyancy force in the direction of its previous stable position. The system can be described as a harmonic oscillator with the Brunt-Väisälä frequency (or buoyancy frequency)

$$N = \sqrt{\frac{g}{T_a} \left(\frac{dT_a}{dz} + \Gamma_d \right)} \quad (2.3)$$

with the gravitational acceleration g , atmospheric temperature T_a , height z and the dry adiabatic lapse rate $\Gamma_d = -\frac{g}{c_p} = -9.8 \text{ °C km}^{-1}$ [73]. In a stable atmosphere ($\frac{dT_a}{dz} > \Gamma_d$) N is a real value and gravity waves can propagate through the atmosphere. The edge case of $\frac{dT_a}{dz} = \Gamma_d$ leads to $N = 0$ and corresponds to the temperature profile of adiabatically ascending air.

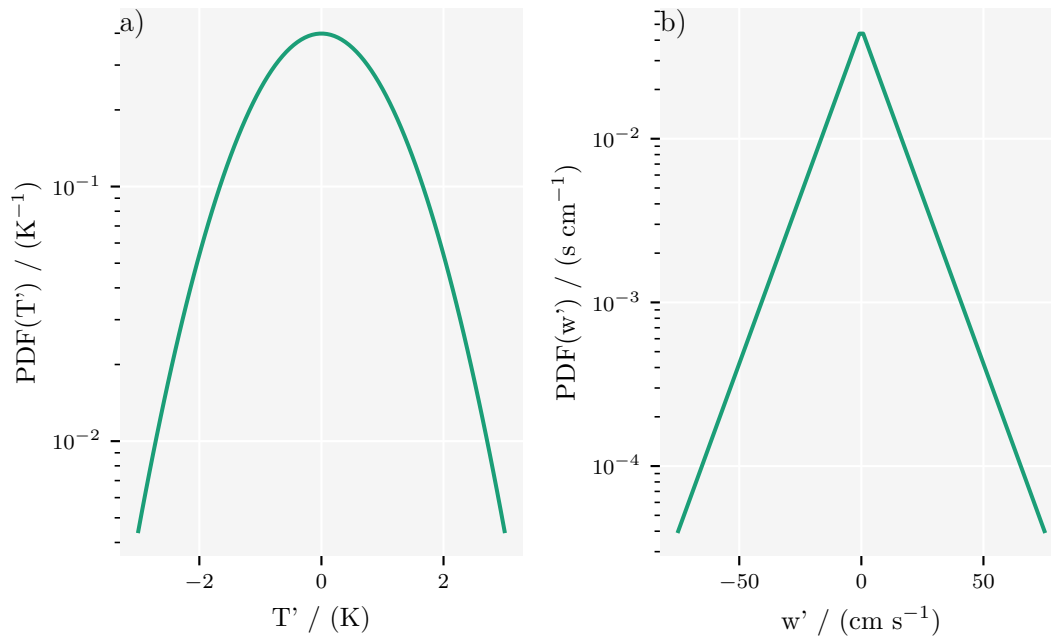


Figure 2.1.2 PDFs for temperature fluctuations T' and updraft velocity fluctuations w' as described by Kärcher and Podglajen [29]. Plot a) describes the probability of temperature fluctuations T' driven by gravity waves as a normal distribution according to equation (2.1). The graph was generated with $\sigma_T = 1$ K. Plot b) describes the probability of updraft velocity fluctuations w' driven by gravity waves as a double exponential Laplacian distribution according to equation (2.2). The graph was generated with $\sigma_w = 15$ cm s⁻¹.

If this implementation is applied in numeric models, the Brunt-Väisälä frequency also serves to determine a characteristic timescale $\tau = \frac{1}{N}$ in which contributions from the $PDF(w')$ (see equation (2.2)) are sampled and included into a model trajectory. An important property of the Lagrangian distribution is that the probability of high argument values is not as small as compared to a Gaussian distribution. This leads to a certain remaining probability of relatively strong updraft fluctuations due to gravity waves, which match with observations.

2.2 Ice nucleation of aerosols

Aerosol particles play an important role in the atmosphere and are crucial for cloud processes. Section 2.2.1 explains the mechanism of liquid aerosol particles to form ice through homogeneous freezing. Section 2.2.2 introduces different modes of heterogeneous freezing and the concept of ice-nucleating active site densities to parameterize the heterogeneous freezing ability of an aerosol.

2.2.1 Homogeneous ice nucleation

Ice nucleation is described as the initial formation of a stable phase of ice within a metastable parent phase of supersaturated water vapor or supercooled liquid water. If the ice nucleation is not aided by a foreign substance it is called *homogeneous* ice nucleation.

Classical nucleation theory (CNT) describes the formation of a nucleus through a change of the Gibbs free energy G . This change ΔG consists of a term driven by the boundary surface ΔG_S and a term being proportional to the volume of the nucleus ΔG_V . The interfacial area of the nucleus is energetically unfavorable, since it increases the Gibbs free energy. However, the volumetric term ΔG_V decreases G and stabilizes the nucleus. Figure 2.2.1 shows a schematic of the two competing contributions to ΔG . The r^2 dependency of the surface term and the r^3 dependency of the negative volume term lead to an energy barrier with a maximum ΔG^* at the critical radius r^* . The nucleus tends to grow or shrink in a way that the system reaches its energetically lowest state. Therefore a nucleus with a radius smaller than r^* is likely to disintegrate, whereas a nucleus larger than r^* will probably initiate a macroscopic ice phase.

The nucleation rate J can be derived from ΔG^* and the temperature T following the proportionality

$$J \propto \exp\left(-\frac{\Delta G^*}{k_B T}\right) \quad (2.4)$$

with the Boltzmann constant k_B . The freezing probability of a liquid droplet to freeze within a time span Δt is

$$P = 1 - \exp(-JV\Delta t) \quad (2.5)$$

with V being volume of the droplet. [45, section 8.1.1]

The classical nucleation theory (CNT) provides a framework to calculate ΔG^* and the nucleation rate J (see e.g. [73, chapter 11]), however the calculated nucleation rates don't match the observations in many cases. This can be partially explained due to a couple of assumptions being made in CNT, such as treating even the smallest nuclei as spherical objects. Therefore we will not look into the exact expressions provided by CNT, but use it just qualitatively to understand the underlying processes.

In the following we will focus on a specific case of homogeneous nucleation: We will look into the phase transition from liquid to ice as it occurs for liquid aerosol particles. To confine the case even further we will look into the homogeneous freezing of ASPs, which are atmospherically relevant in the UTLS.

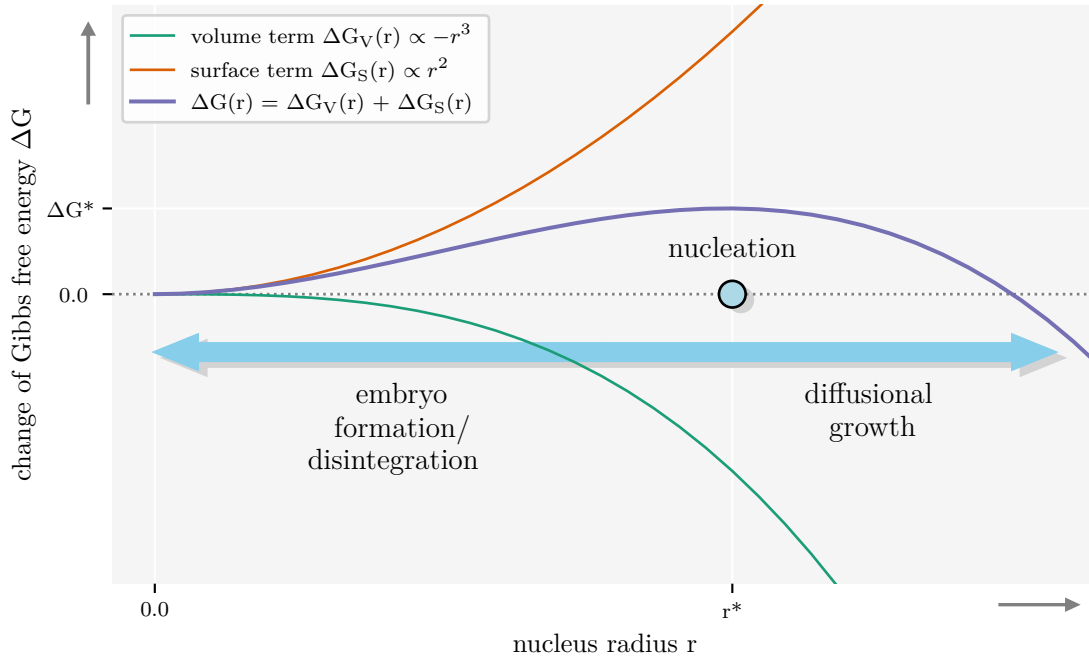


Figure 2.2.1 Change of Gibbs free energy for the formation of a nucleus (visualized as circle). The surface term is proportional to r^2 and increases the Gibbs free energy G . It is dominant for small radii ($r < r^*$). The volume term is proportional to $-r^3$ and reduces the Gibbs free energy. It becomes dominant for radii $r > r^*$. The sum of both terms forms a potential barrier for the nucleation process with the maximum ΔG^* at the critical radius r^* .

To describe the influence of a foreign substance, such as sulfuric acid, in the aqueous solution droplet we introduce the water activity

$$a_w = \frac{p_{w,0}^{sol}}{p_{w,0}^{liq}} \quad (2.6)$$

with the water vapor saturation pressure over the aqueous solution $p_{w,0}^{sol}$ and the same quantity over a surface of pure liquid water $p_{w,0}^{liq}$. The water activity describes the reduction of $p_{w,0}^{liq}$ due to the presence of a dissolved substance. We can define a similar term as ice activity

$$a_w^i = \frac{p_{w,0}^{sol}}{p_{w,0}^{ice}} \quad (2.7)$$

with the water vapor saturation pressure over ice $p_{w,0}^{ice}$ as reference.

Koop et al. [36] were able to show that the homogeneous nucleation rate of an aqueous solution particle can be entirely described by the *water activity criterion*

$$\Delta a_w = a_w - a_w^i \quad (2.8)$$

and provide a parameterization for the homogeneous nucleation rate that is independent of the nature of the solute:

$$\log_{10}(J) = -906.7 + 8502\Delta a_w - 26924\Delta(a_w)^2 + 29180(\Delta a_w)^3. \quad (2.9)$$

Reasonable nucleation rates are found for Δa_w in the range of 0.26 to 0.34.

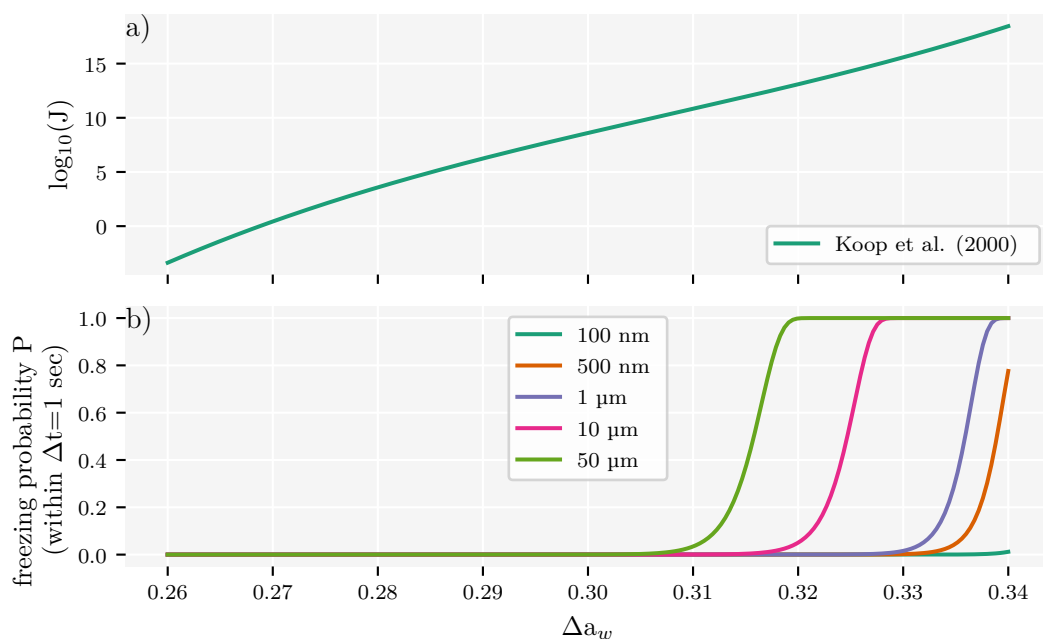


Figure 2.2.2 Homogeneous nucleation rate and freezing probability as a function of the water activity criterion Δa_w . Plot **a)** shows the parameterized homogeneous nucleation rate as formulated in equation (2.9) [36]. Plot **b)** derives the freezing probability of a spherical particle within a time period of 1 second according to equation (2.5) for different radii.

As shown in Figure 2.2.2 the nucleation rate is a very steep function, so changes in Δa_w can lead to strong changes in the freezing probability P .

However, Δa_w is not directly accessible from an experimental perspective. Instead it can be preferred to describe Δa_w with quantities that are experimentally available, such as temperature and the saturation ratio. Under the assumption that the droplets are in equilibrium with their environment we can state

$$p_w^{sol \text{ equil.}} = p_w$$

with the definition of the saturation ratio with respect to ice

$$S_{\text{ice}} = \frac{p_w}{p_{w,0}^{\text{ice}}} \quad (2.10)$$

and insert both expressions into [equation \(2.8\)](#). Hence we can reformulate the water activity criterion as

$$\Delta a_w = \frac{p_{w,0}^{\text{ice}}(T)}{p_{w,0}^{\text{liq}}(T)} \cdot (S_{\text{ice}} - 1) \quad (2.11)$$

which is now a function of the saturation ratio S_{ice} and temperature. The formulations for the saturation vapor pressures are derived from parameterizations and depend only on temperature [55, 56].

The homogeneous nucleation rate and the resulting freezing probabilities shown in [Figure 2.2.2](#) can now also be described as a function of temperature and S_{ice} . Thus, due to the steep nature of J a decrease of temperature and/or an increase of supersaturation can trigger a sudden occurrence of homogeneous freezing. The respective set of critical parameters (T^{crit} , $S_{\text{ice}}^{\text{crit}}$) is often called the homogeneous freezing threshold.

Such a freezing event is highly susceptible to the temporal derivative of the saturation ratio S_{ice} . The faster S_{ice} increases (e.g. by dropping temperature) the more particles of an aerosol population can freeze. Since the freezing probability is proportional to the volume of a particle the biggest droplets tend to freeze first. As long as the supersaturation increases the freezing threshold for an increasing fraction of smaller droplets will also be reached. The end of the homogeneous nucleation mode is reached once the depletion of water vapor from ice crystal growth overcompensates the increase of S_{ice} . With a decrease of S_{ice} , the homogeneous freezing probability quickly drops to insignificant magnitudes.

The band in which S_{ice} triggers homogeneous freezing is typically rather small and within the range of uncertainty. Therefore the observer of an experiment might only be able to derive a single critical freezing threshold for a whole aerosol population.

2.2.2 Heterogeneous ice nucleation

When ice nucleation is aided by a foreign particle or substance it is called *heterogeneous* ice nucleation and can already happen at saturation ratios or supercooling at which ice would not form homogeneously. The process is closely related to heterogeneous condensation nucleation, which, however, will not be covered here. If a solid aerosol particle leads to the formation of an ice crystal, it is called [ice-nucleating particle \(INP\)](#). The nucleation happens on the particle surface, so the nature of the surface is crucial for the ability of a particle to act as an [INP](#). The surface is generally not uniform or smooth,

but characterized by surface defects such as cracks and steps or pores. Such a surface site can facilitate water molecules to arrange as an ice embryo, hence lowering the energy barrier ΔG^* for nucleation. The absolute reduction of ΔG^* depends on the nature of the surface site on the INP surface. The most efficient surface site to nucleate ice defines the freezing property of an individual aerosol particle.

There are currently two hypotheses about the nature of heterogeneous nucleation [45, section 8.1.2.5]. One is the *stochastic* hypothesis, which assumes that heterogeneous nucleation can be described by a nucleation rate (as in equation (2.4)). Such an approach implicates that the probability P of a nucleation event to happen in a metastable environment is just a matter of time. For an aerosol population this approach would mean that the number of activated particles would increase with time while temperature and S_{ice} remain constant.

In contrast, the *deterministic* approach (or *singular hypothesis*) assumes that heterogeneous nucleation depends on a distinct critical temperature and/or supersaturation, based on the activation of specific surface sites. This approach is time-independent and involves the assumption of reproducibility for individual INPs, so they would freeze at the same condition for multiple runs. In the following focus will be on the deterministic approach.

Heterogeneous ice-nucleation modes

Depending on the ambient temperature and supersaturation different mechanisms are dominant for atmospheric heterogeneous ice formation. Contact freezing can happen already at temperatures slightly below the melting point of water when an INP collides with a water droplet. An important mechanism for mixed-phase clouds is immersion freezing, which describes the activation of an INP immersed in a water droplet. Immersion freezing is typically observed between -15°C and the homogeneous freezing threshold of pure water at -38°C . Below -38°C the dominant ice-nucleation mechanism is deposition freezing. It describes ice formation that happens directly from the water vapor gas phase without an intermediate liquid phase. However, it is still part of debate if deposition nucleation might have a preceding condensation with subsequent freezing in surface defects, such as cracks and pores [48]. Deposition nucleation could also be initiated at sites with ice being preserved in surface defects [89, 49]. An extensive overview on heterogeneous ice-nucleation of different INPs was carried out by Hoose and Möhler [24].

Ice-nucleating active site density

The *ice-nucleating active site* (INAS) density n_s is an empirical approach to describe heterogeneous ice formation based on the available aerosol surface area. An INP is

assumed to have a characteristic number density of surface sites which lead to ice-nucleation at defined conditions. The concept is based on early works of Vali [86], while the description as given by Ullrich et al. [85] is used here. It is based on the assumption that the aerosol is of uniform composition and that the aerosol surface area has a certain density of sites which get activated at a certain critical freezing condition.

If a polydisperse aerosol is divided in k size bins, the INAS density n_s is given by

$$n_{\text{ice}} = \sum_{j=1}^k n_{\text{ice},j} = \sum_{j=1}^k n_{\text{ae},j} [1 - \exp(-S_{\text{ae},j} \cdot n_s(T, S_{\text{ice}}))] \quad (2.12)$$

with the number concentration of heterogeneously nucleated ice crystals n_{ice} , aerosol number concentration n_{ae} , surface area of a single aerosol particle S_{ae} , temperature T and saturation ratio with respect to ice S_{ice} [85]. This expression describes the ice, which is formed from an initial number concentration at a certain coordinate in the (T, S_{ice}) space. Note, that n_s is a parametrization referring to an unaltered specific aerosol sample.

INAS densities can be used to describe different heterogeneous freezing modes, such as immersion freezing or deposition freezing. However, parameterizations of n_s are usually given for a limited range in the parameter space and should not be used beyond.

2.3 Cirrus clouds

Cirrus clouds are one of the three basic cloud categories, besides cumulus and stratus clouds [45]. The word *cirrus* is Latin and means wisp or curl, which describes their thin and fibrous appearance. They have a white look and can be partially transparent due to their low water content. Cirrus clouds consist entirely of ice crystals, whose sedimentation can lead to optically visible fall streaks.

The cirrus formation temperature region is below 235 K [38] reaching down to below 190 K. For lower temperatures <190 K decreased detectability becomes apparent in remote sensing data [39]. The median cloud top height ranges from 8 km at the poles to 14 km in the tropics [64].

Cirrus clouds have an average global land area coverage of 22.8%. In the Arctic region averages are on the order of 20% to 45%. [22, Fig. 2-1]

2.3.1 Cirrus formation

Cirrus clouds can be classified into two formation types, namely *in situ origin cirrus* and *liquid origin cirrus*. The in situ origin cirrus type is characterized by a formation below

235 K with ice water content (IWC) originating primarily from the gas phase. Liquid origin cirrus forms optically dense clouds from lifted mixed phase clouds, which glaciates during the updraft into cirrus formation temperature regions. [38]

In general liquid origin cirrus has a higher IWC and is characterized by larger ice crystals [39]. However, a study comparing Arctic cirrus clouds by distinguishing the formation mechanisms could depict in-situ cirrus to be thicker [91].

In this work the scope is limited to in situ origin cirrus. The formation of in situ origin cirrus clouds can be split into two further subclasses, separating between slow and fast updraft velocity with a transition region between 10 cm s^{-1} to 50 cm s^{-1} [38]. Under slow updraft the cloud is characterized by only few and large heterogeneously formed ice crystals. For fast updrafts many ice crystals nucleate homogeneously and grow only to smaller sizes. The differences blur along the cloud lifetime due to ice crystal growth and sedimentation of the largest ice crystals [39].

The main ice nucleation mechanism for the formation of in situ cirrus clouds is homogeneous freezing. In case of INPs being present a combination of homogeneous and heterogeneous freezing can occur. Pure heterogeneously formed cirrus clouds are untypical. The necessary supersaturation is primarily generated by lifting of the air parcel. That can be driven on a large scale along a frontal boundary. On a small scale atmospheric turbulence and fluctuations from convection and gravity waves can lead to a sufficient supersaturation. [22, section 3]

Competition between homogeneous and heterogeneous ice formation

Heterogeneous ice nucleation happens generally before homogeneous ice nucleation rates become relevant (see section 2.2.1 and section 2.2.2). As ice forms heterogeneously, the crystals grow from water vapor and deplete the available water vapor. The number of homogeneously formed ice crystals, however, depends strongly on the slope of S_{ice} . During an updraft scenario, heterogeneous ice nucleation affects the temporal development of S_{ice} and therefore controls the conditions for a potential occurrence of a later homogeneous nucleation mode. Depending on the amount of heterogeneously formed ice the depletion of S_{ice} can either just result in a reduction of homogeneously formed ice or even suppress the homogeneous mode completely.

The competition between heterogeneous and homogeneous freezing is one of the main uncertainties for the representation of cirrus cloud formation in models. While homogeneous freezing is generally described by the formulation of Koop et al. [36], the approaches to implement heterogeneous freezing varies for different models. Studies by Kärcher, Hendricks, and Lohmann were a milestone for the representation of the freezing competition in cirrus models [34, 35, 33]. In this approach, heterogeneous freezing

is represented as immersion freezing and based on a "shifted water activity", similar to the description of homogeneous nucleation rates by Koop et al. [36]. A work from Barahona and Nenes provided parameterizations for the ice crystal number concentration and ice crystal [particle size distribution \(PSD\)](#) of heterogeneous and homogeneous ice, respectively [3]. In an accompanying paper they extended their approach to polydisperse aerosol and utilized a flexible heterogeneous freezing spectrum to describe heterogeneous ice formation [2]. Other works based the representation of heterogeneous freezing on nucleation rates derived by CNT [44]. In this work model simulations investigating the competition between homogeneous and heterogeneous freezing are based on INAS density parameterizations of INPs, as explained in [section 2.2.2](#).

2.3.2 Cirrus properties

The density of cirrus clouds can be expressed by the [IWC](#) or the total ice crystal number concentration. Over the temperature spectrum of 185 K to 245 K the median [IWC](#) lies between 2×10^{-1} ppmv and 4×10^1 ppmv and the median ice crystal number concentration mainly between $1 \times 10^{-4} \text{ cm}^{-3}$ and 5 cm^{-3} [39, Fig. 6].

The lifetime of cirrus clouds formed under fast updrafts have lifetimes of tens of minutes to less than an hour. The lifetime of slow updraft in situ cirrus clouds can have a lifetime in the range of hours to days. [39, section 4.2]

The microphysical structure of cirrus clouds varies widely in terms of ice crystal size and shape. The largest ice crystals reach up to 800 μm for liquid origin cirrus and can come close to 600 μm for in situ origin cirrus [46]. Median diameters reside in the order of tens of μm along the temperature spectrum from 185 K to 245 K [39, Fig. 7c, Fig. 8c, Fig. 8f]. The shapes of the ice crystals vary strongly depending on the ambient conditions and dynamics during the formation of the cirrus cloud. Early studies showed that weaker updrafts lead to ice crystal shapes of hexagonal columns and plates and stronger updrafts lead either to hollow hexagonal columnar shapes or clusters of prismatic crystals joined at a common center (bullet rosettes) [22, section 4 d.]. However, other in situ balloon-borne measurements could hardly find any plates [91].

The microphysical properties of cirrus clouds, such as number concentration, size and shape of ice crystals vary widely. Balloon-borne measurements showed that a part of this spread can be explained by differentiating between in situ origin and liquid origin cirrus [91, 90]. Yet, the large uncertainties and spreads regarding the number and shape of ice crystals hinder the progress of understanding the radiative properties of cirrus clouds.

Optical properties

Cirrus clouds play a significant role for the Earth's radiation budget, also driven by their large spatial extent [22].

Krämer et al. quantified the radiative forcing of cirrus clouds depending on their formation type [38, Fig. 5]. Slow updraft in situ origin cirrus has a small optical depth, which results in a slight net warming effect of $\leq 1.5 \text{ W m}^{-2}$. Fast updraft in situ origin cirrus has a larger optical depth and a stronger net radiative forcing of 2 W m^{-2} to 10 W m^{-2} . However the thickest cirrus can change the sign of its forcing and switches to a small net cooling effect. Liquid origin cirrus has the largest optical depths and has therefore a strong negative radiative forcing of -15 W m^{-2} to -250 W m^{-2} .

To determine the radiative properties of cirrus clouds the ice crystal number concentration or *IWC* is as important as the shape and size of the ice crystals [93]. However, especially for small ice crystals $< 100 \mu\text{m}$ there is a considerable uncertainty about their shape and scattering properties.

2.4 Climate engineering: Cirrus cloud thinning

Here cirrus cloud thinning is introduced and discussed with a specific emphasis on the Arctic.

2.4.1 The concept of cirrus cloud thinning

CCT is based on the idea that the presence of *INPs* during the formation of a cirrus clouds leads to bigger and fewer ice crystals. The heterogeneous ice formation happens before homogeneous freezing sets in and can therefore deplete the water vapor to suppress homogeneous freezing (see section 2.3.1). These bigger ice crystals have a faster fall velocity, which leads to a shorter cloud lifetime. With respect to the net warming radiative properties of cirrus clouds, this concept is proposed to reduce the warming effect of cirrus clouds by enhancing the amount of outgoing longwave radiation. The concept of *CCT* was introduced by Mitchell and Finnegan [51] stating that the seeding effect could lead to a forcing of -2.8 W m^{-2} .

2.4.2 The potential of cirrus cloud thinning

The potential of *CCT* was investigated through multiple modeling studies, which led to inconclusive results. Thus, the current knowledge about *CCT* is ambiguous.

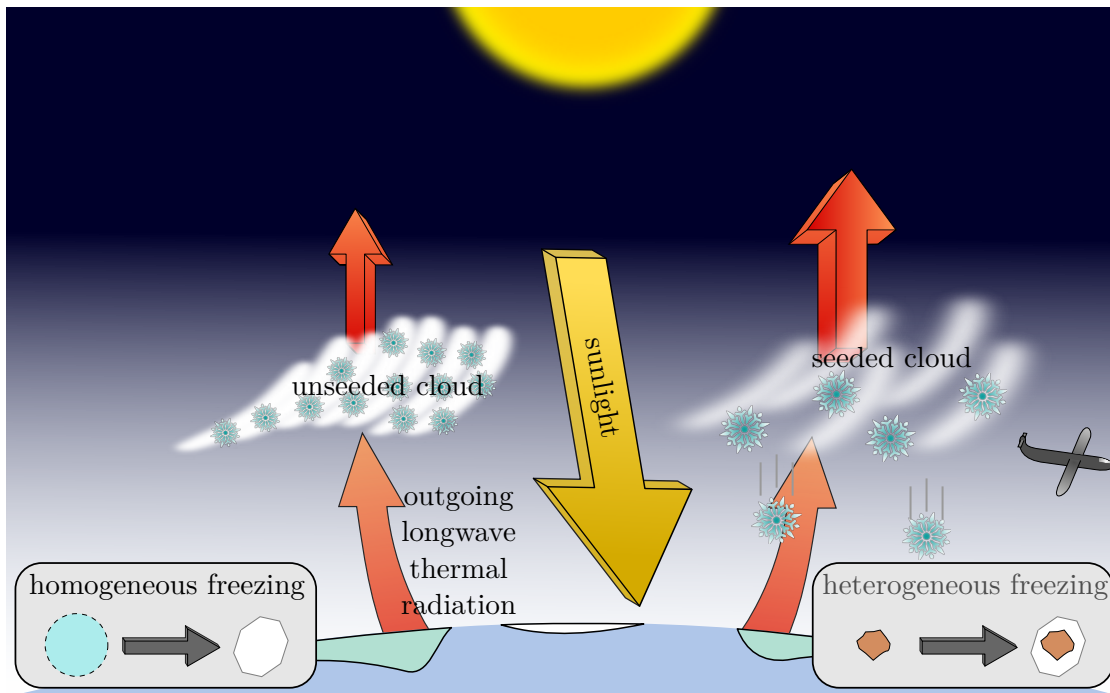


Figure 2.4.1 Schematic drawing on the concept of cirrus cloud thinning. Cirrus seeding leads to thinner clouds with bigger ice crystals. Due to the increase fall velocity the cloud lifetime is reduced. This could reduce the net positive forcing of cirrus clouds and enhance the amount of outgoing thermal radiation.

A modeling study by Storelvmo et al. [80] in 2013 states that CCT has the potential to compensate the effect of human activities on climate, while holding the risk of overseeding causing the opposed effect. In a followup study they showed that seeding in specific regions can lead to more efficient results compared to global seeding and concluded a potential net surface cooling of 1.4°C [79]. The study points out that cooling is strongest at high latitudes and could therefore be useful to prevent Arctic sea ice loss. A modeling study by Kuebbeler et al. [42] in 2014 derived a net forcing of -0.94 W m^{-2} on a global scale, being most pronounced in the tropics and northern mid latitudes. Another modeling study by Muri et al. [54] in 2014 represented cirrus cloud thinning as increased ice crystal sedimentation velocity and concluded a global net forcing of -1.55 W m^{-2} . They also emphasized the side effect of changes in atmospheric circulation and precipitation. In contrast a modeling study by Penner, Zhou, and Liu [57] could not show a significant amount of negative forcing. Only for a single scenario with constrain to slow updrafts and excluding preexisting ice could show a forcing of -0.74 W m^{-2} . A study by Kristjánsson, Muri, and Schmidt [41] in 2015 examined CCT with respect to the impact on the hydrological cycle and found an enhanced moisture availability in low-latitude land regions and a strengthening of the Indian monsoon. Jackson, Crook,

and Forster [26] represented CCT in a model study through increased ice crystal fall speed velocities and concluded a radiative forcing of -2 W m^{-2} .

Those studies have in common that they don't have the competition of homogeneous and heterogeneous freezing implemented. However, the competition between heterogeneous and homogeneous ice nucleation is crucial for the seeding approach. Recent model studies using the ECHAM-HAM general circulation model (GCM) takes the competition between homogeneous and heterogeneous freezing into account. Using this model, a study by Gasparini and Lohmann [16] in 2016 found the radiative effect of cirrus clouds to be $+5.7 \text{ W m}^{-2}$, which is large enough to provide a substantial potential for climate engineering measures. However, the simulations did not show a significant climatic effect by CCT. Moreover, globally uniform seeding showed an increased cloud cover because efficient INP convert large fractions of supersaturated clear-sky areas to cirrus clouds. With respect to the clouds scattering properties a shift towards smaller ice crystals was observed, which outweighs the effect of reduced ice crystal number concentrations. In a later modeling study ECHAM-HAM was compared to the CESM-CAM5 model (used in some of the studies mentioned above) for a scenario of CCT in an atmosphere with $1.5 \times \text{CO}_2$. Both model differ significantly in their cirrus representation and the achieved forcing varied by more than a factor of two between -1.8 W m^{-2} (CESM) and -0.8 W m^{-2} (ECHAM-HAM). In contrast to other studies the precipitation generally decreased. Additionally the study could show on the one hand that CCT decreases the frequency of the most extreme precipitations globally, but on the other hand shifts the locations of extreme precipitations shifted towards the Sahel and Central America. Improvements on the microphysical scheme of the ECHAM-HAM model reduced a strong positive forcing of overseeding scenarios, but did not lead to the conclusion that CCT might be a feasible climate engineering strategy on a global scale [83]. A recent study by Tully et al. [83] investigated the subject further by not applying the seeding globally, but only along flight tracks of commercial airlines. The results, however, did not show a significant cooling effect for moderate seeding, but positive forcing from overseeding.

Instead of applying a globally uniform seeding concentration Liu and Shi [43] (2021) used a flexible seeding concentration by calculating an optimal seeding concentration. with their new method they resulted in a global cooling effect of -1.36 W m^{-2} , compared to -0.27 W m^{-2} and 0.35 W m^{-2} for uniform seeding concentrations of 20 l^{-1} and 2000 l^{-1} , respectively.

In a model study by Gruber et al. [19] CCT was applied using the ICON-ART model with a comparably high resolution. In comparison to other modeling studies the simulation was narrowed to a very specific geographical region (the Arctic). The study observed a decrease in of the ice crystal number concentration, leading to increased outgoing thermal radiation. Moreover, sedimentation of ice crystals led to a decrease of mixed-phase clouds, which, in case of the Arctic winter, led to additional negative forcing. However, designing the seeding scenario in a way to suppress the homogeneous freezing onset was less effective than seeding everywhere, since even with the creation of additional cirrus

clouds the homogeneous freezing was generally suppressed. This finding is in contrast to other model scenarios which found positive forcing from overseeding.

In summary, the literature on CCT is partially contradictory. Cirrus cloud microphysics are not well quantified and parameterized, hence all models lack a suitable representation. The actual cooling effect, as well as possible side effects are still a matter of debate.

2.4.3 Cirrus cloud thinning during the Arctic winter

The effect of global warming varies for different regions and has a strong effect in the Arctic compared to the global average. The causes are not fully understood and climate models underestimate the rise of surface temperature and decline of sea ice [72]. Based on the period between 1979 and 2021, a recent study showed that the Arctic warmed nearly four times faster than the globe on average [61]. The extent of the Arctic sea ice has declined by 43% in the 41-year period of record between 1979 and 2019 [1] and has since decreased in each month of the year [25, section 9.3.1].

A couple of self-amplifying feedback effects, known as polar amplification or Arctic amplification, make the Arctic especially vulnerable to increasing temperatures. Melting of sea ice leads to a decreased albedo of the surface, which leads to an increase of the surface temperature. Melting of perma-frost soil triggers the release of the greenhouse gases CO₂ and methane, which intensifies the greenhouse effect. On a broader scale, warming of the air causes a weakening of the polar vortex, which shields the Arctic from warm air from lower latitudes during winter. A weakening, or even a collapse, of the polar vortex leads to high temperatures in the Arctic. An increasing amount of melting ice causes changes in the Arctic ocean circulations, leading to an increased mixing with warmer sea water from the Atlantic ocean, which enhances the melting of sea ice.

CCT could be especially efficient during the Arctic winter to mitigate some of the afore mentioned effects on increasing temperatures. The method is expected to work especially with respect to in situ origin cirrus which is the predominant form of cirrus in the Arctic [91, 90]. While the radiative effect of a cloud during daytime is the net sum of cooling through its albedo effect and warming by trapping outgoing longwave radiation, only the warming contribution remains during nighttime. Due to the high latitude the Arctic winter is a period with strongly reduced sunlight, which enhances the potential effective cooling of CCT. When irradiating sunlight is not present, even a possible side effect to also reduce mixed-phase cloud coverage, as modeled by Gruber et al. [19], could contribute to a negative forcing.

Based on the specific motivation to save the Arctic from the dramatic effects of climate change, CCT could potentially attenuate the consequences of global warming and Arctic amplification effects.

Chapter 3

Methods and Procedures

This chapter presents methods and experimental procedures, which were used in this work.

[Section 3.1](#) provides information about the different sample types, which were used as seeding aerosol in our experiments.

In [section 3.2](#) the [AIDA](#) cloud chamber facility is described. This section also includes a description of the instrumentation and the standard procedure for expansion experiments.

[Section 3.4](#) gives information about the analysis of data, which was gathered at the [AIDA](#) facility.

Finally, [section 3.5](#) describes the calculation of the interaction between the [AIDA](#) cloud chamber walls and the contained gas. Two different approaches of wall flux parameterizations are introduced. In a later step the derived wall fluxes can be used to model processes in the chamber.

3.1 Seeding aerosol types

Three different bulk aerosol samples were used as [CCT](#) seeding agents, namely amorphous silica, calcium carbonate and quartz. A brief overview on the samples is given in [Table 3.1.1](#).

An aerosol potentially used for [CCT](#) has to fulfill several criteria. Most importantly, the seeding aerosol should not harm the environment and needs to be non-toxic. A low price and high availability are beneficial if a future large scale application might be considered.

The fumed silica bulk powder sample was bought from SIGMA-ALDRICH® (catalog number S5505) [75]. It has a white appearance, a fluffy structure and is relatively difficult

Table 3.1.1 The bulk aerosol samples used in our experiments. Basic key information is provided, respectively.

	fumed silica	quartz	calcium carbonate
chem. formula	SiO ₂	SiO ₂	CaCO ₃
internal abbrev.	Sil	BCR	CaCO3
structure	amorphous	crystalline	crystalline
density	0.0368 g cm ⁻³ (bulk)	2.6190(65) g cm ⁻³	2.93 g cm ⁻³
specific surface area	200(25) m ² g ⁻¹	–	–
reference	[75]	[74]	–

to handle, since it is strongly susceptible to electrostatic charging. In accordance with its fluffy structure it comes with a comparably low bulk density of 36.8 mg cm⁻³. It is composed of submicron-sized spheres, which are to 40 % to 60 % fused into 100 nm to 200 nm long chains [75, data sheet]. The particle size is stated as 0.2 µm to 0.3 µm.

Our quartz sample was part of a program by the European Community Bureau of Reference (BCR) in 1979 to create quartz reference powders for calibration of particle sizing instruments. It was stored at KIT/IMK-AAF under dry and constant temperature conditions for an unknown period of time. The sample has the identification number 66 and we used batch number 1853. According to the data sheet 90 % of the material is within a size range of 0.35 µm to 2.5 µm. The data sheet is stored at KIT/IMK-AAF and a digital version is not available.

The calcium carbonate bulk sample was sourced from SIGMA-ALDRICH® (SKU: 310034-500G) [74]. Besides its density no further relevant information could be obtained from the data sheet.

3.2 The AIDA cloud chamber facility and its instrumentation

The AIDA (Aerosol Interaction and Dynamics in the Atmosphere) cloud chamber facility is the core of the research infrastructure at the department IMK-AAF at the KIT. Section 3.2 shows schematic drawings of the facility. A detailed description of the chamber is available in Möhler et al. [52]. However, a specific technical publication about the facility is not available.

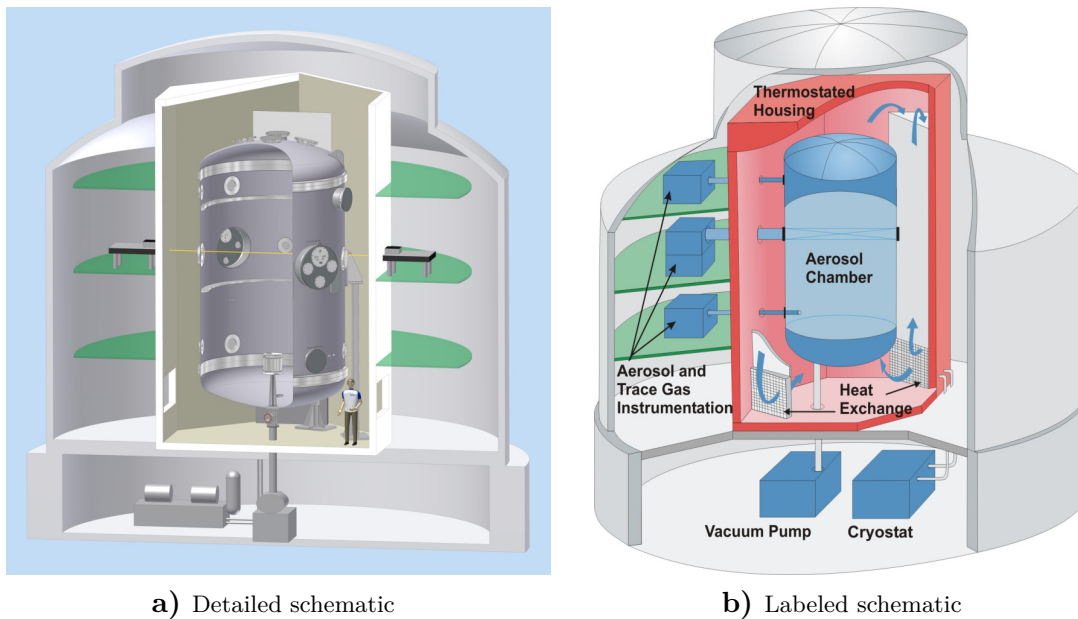


Figure 3.2.1 Schematics of the AIDA cloud chamber facility (source: KIT/IMK-AAF).

The chamber is a cylindrical vessel with a height of 7 m, a diameter of 4 m and rounded heads. The volume of the aluminum vessel is 84 m^3 . It has 2 cm thick walls and can be evacuated to a final pressure of about 0.01 hPa. [52]

The chamber is passively cooled through a thermal housing. Temperature is measured by a set of sensors distributed across the chamber. A fan at the center bottom enforces a mixing of air to prevent strong vertical temperature gradients.

Several mechanical pumps with adjustable pump speeds can be used for expansion cooling of the interior. Such expansion cooling simulates the updraft of an air parcel in the real atmosphere. Thus, dynamic cloud formation processes can be investigated in a controlled laboratory environment.

3.2.1 Pump system

The facility has strong mechanical pumps, which can be used to evacuate the cloud chamber. For the majority of the conducted experiments pump two (P2) was used. If faster cooling was desired, the stronger pump one (P1) was also used, however, it produces more vibrations.

A variation of pump rates corresponds to different cooling rates. However the cooling is not adiabatic due to an emerging heat flux from the chamber walls. The heat flux is

driven by the temperature difference to the chamber wall, which stays at almost constant temperature while the gas cools down. The effect of the heat flux can be minimized by reducing the time of an expansion through faster cooling. However, slower updrafts are often atmospherically more relevant and improve the time resolution of observed cloud formation processes. We chose a pump power of P2 80% for most of our experiments. With this pump rate the temperature change at typical homogeneous freezing onsets translates to approximately 3 m s^{-1} .

3.2.2 Temperature measurement

The temperature measurement is based on two sets of thermocouple sensors. A vertical and a horizontal chain of each 11 temperature sensors measure the independently. The temperature considered the mean gas temperature T_g is derived from averaging over a selection of temperature sensors. A delay of 3 s is considered for the thermocouple sensors at atmospheric pressure. We account for this delay in the data analysis.

The wall temperature is also measured at multiple vertically distributed positions. The average wall temperature T_w is derived by averaging a specified fraction of those sensors. Gas and wall temperatures are measured with an accuracy of $\pm 0.3 \text{ K}$ [53]. At mixed conditions the temperature variability in the chamber is less than $\pm 0.2 \text{ K}$ [53] and rarely exceeds $\pm 0.3 \text{ K}$ for fast expansions [5].

3.2.3 Water measurement

The water content in the chamber is measured with four independent instruments.

Three of those instruments are based on the absorption of a [tunable diode laser \(TDL\)](#), which is tuned to a wavelength of 1370 nm matching a spectral line of water. The instrument [APicT](#) (AIDA PCI in cloud TDL) uses an open-path [TDL](#) beam through the chamber. The instrument is available in two different version, with the laser beam following a single-path through the chamber or crossing the chamber multiple times. The multi-path [TDL](#) system relies on a mirror system, to accomplish the increased path length. A typical path length is 80 m. The estimated uncertainty of the multi-path [TDL](#) system is $\pm 5\%$. The multi-path [APicT](#) is much more sensitive, however the single-path version is more robust with respect to vibrations. Due to the high sensitivity of the mirror system on vibrations from the mechanical pumps we generally apply a Savitzky-Golay filter on the data. Extensive information about the multi-path [APicT](#) can be found in Fahey et al. [15, appendix A1].

The instrument [APeT](#) (AIDA PCI extractive TDL) works similarly, but the laser beam doesn't cross the chamber. Air from the chamber is sampled with a flow of $5 \text{ l}_{\text{std}} \text{ min}^{-1}$ to

$10 \text{ l}_{\text{std}} \text{ min}^{-1}$ into a measurement volume, where the TDL system measures the absorption within the sample volume. The volume is located outside the thermal housing and at room temperature. If the sampled air includes droplets or ice crystals from the cold cloud chamber, they evaporate inside the warm sample volume. Therefore APeT measures the total water content. The uncertainty is $\geq 5\%$ and the accuracy is 100 ppb.

The total water content is also measured by a commercial dew point mirror instrument (MBW CALIBRATION™ MODEL 373-LX™) [59]. According to the data sheet the device is capable of measuring down to -95°C , however in reality a good signal gets already difficult at -60°C . It has an accuracy of $\pm 3\%$ and a precision of $\pm 1.5\%$ [15].

3.2.4 Depolarization laser SIMONE

SIMONE is a depolarization laser instrument, detecting the scattered light from the 1.8° (forward scattering) and 187.2° (backward scattering) angle. The backwards scattered light is analyzed with respect to the linear and perpendicular polarization components. The instrument is well described in a paper by Schnaiter et al. [67].

In context of this work we use the scatter data from SIMONE only qualitatively. As a real time in-situ instrument we can detect sudden changes in the aerosol or ice crystal population without any time delay. Therefore the instrument is well suited to determine the onset of homogeneous freezing modes. As soon as homogeneous freezing sets in, the scattering properties of the particles in the chamber change rapidly, which can be detected as a kink in the scatter intensity data. However, this approach comes to its limits in case of strong freezing competition and blurring freezing onsets.

3.2.5 Optical particle counters

To detect particles in the AIDA cloud chamber we use a set of two optical particle counter (OPC) sensors (welas2100 and welas2300, Palas GmbH). The models are internally and in the following called welas1 and welas2. The OPC system samples air from the chamber with a specified mass flow. In the sensor is an optical detection volume, where every particle that crosses is illuminated by a white light. The light scattered at an angle of $90(12)^\circ$ is transferred with an optical fiber to a control unit where it is detected and enhanced by a photomultiplier. More technical details can be derived from the doctoral thesis of Thea Schiebel (2017 at KIT/IMK-AAF).

The two sensors operate in two different but overlapping size ranges, so a broad size spectrum can be observed. However, a calibration to derive the exact sizes of ice crystals is not available. Therefore the size information from the OPC system can only be

considered as an indication. Particle number concentrations derived by the **OPCs** have an relative uncertainty of $\pm 20\%$

Both sensors are connected to the **AIDA** cloud chamber through vertical sampling lines and are located in the thermal housing beneath the chamber.

To be noted, the particle number concentration of `welas1` shows unexplainable high values, thus a correction factor is applied. The correction factor has been chosen in such way, that the number concentration of both sensors fits for particles which are in the detection range of both sensors. Since the correction factor is not well justified, if possible the data from `welas2` should be used instead.

3.2.6 Condensation particle counters

Condensation particle counters (CPCs) measure particle number concentrations. Within the **AIDA** setup they are located outside the thermal housing and sample air through a sampling lines from the chamber. They evaporate butanol and create an internally supersaturated environment in which particles from the sampled air flow activate to droplets. This increases their scattering intensity, which makes them easily detectable when being illuminated. By knowing the flow rate and counting the scatter events the device can derive the number concentration of particles.

The AIDA facility has multiple **CPC** models, which have different technical characteristics. For our experiments we used a CPC-3010 from TSI® company (discontinued since 2006). The relative uncertainty is considered as $\pm 10\%$.

3.2.7 Aerosol generation instrumentation

The aerosol populations in our experiments were generated through different techniques. The aerosol bulk samples were dispersed using either a rotating brush generator (**RBG**) or a small-scale particle disperser (**SSPD**). Aerosol populations of **ASPs** were generated using a self-made sulfuric acid vaporizer. The instruments are briefly introduced in the following.

Rotating brush generator

The **RBG** is an instrument from Palas GmbH to disperse bulk powder samples (model RBG-1000). In operation a stamp moves upwards through a cell with a defined speed

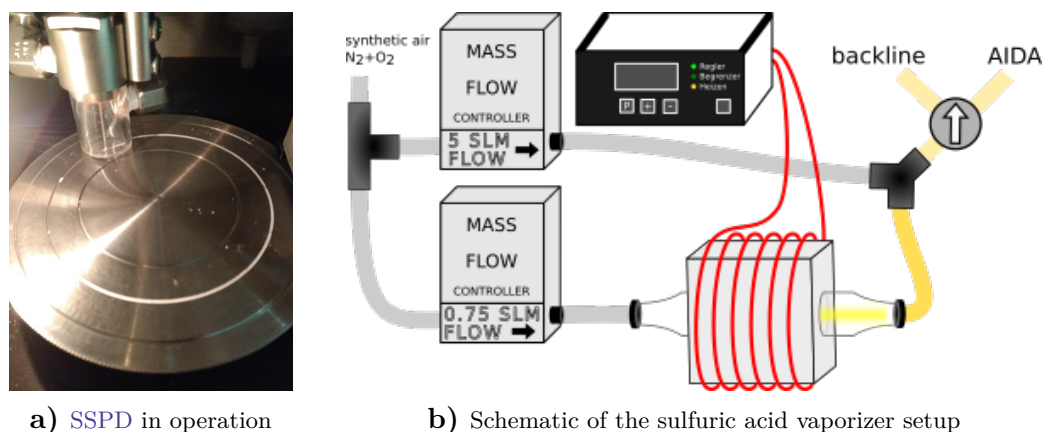


Figure 3.2.2 Instrumentation for aerosol generation at AIDA. Subfigure a) shows the rotating plate of the SSPD with quartz aerosol. Subfigure b) shows a schematic of the setup for the generation of sulfuric acid ASP.

and pushes the bulk sample continuously into a rotating mechanical brush. The brush disperses the aerosol into a stream of clean synthetic air. The operator can control the speed of the stamp, the rotation frequency of the brush and the air flow. In this work standard settings of 1200 rpm for the brush and a flow of synthetic air at $8 \text{ l}_{\text{std}} \text{ min}^{-1}$ with 0.7 hPa were applied. Depending on the aerosol type a stamp speed of 5 mm h^{-1} to 30 mm h^{-1} was used.

Two cyclones (internally called cyclone2 and cyclone3) were placed behind the RBG to filter larger aerosol particles before being dispersed into the chamber.

Small-scale particle disperser

The SSPD (model 3433, TSI®) is used to disperse bulk powder samples. The plate rotates and ensures that the bulk aerosol is moved under a nozzle which sucks the aerosol in. The nozzle is encircled by a sheath flow of dry air to ensure that the nozzle doesn't suck in the humid air from the laboratory. The aerosol uptake of the nozzle can be controlled by specifying a differential pressure. The nozzle input and the sheath flow have to be adjusted in the right proportion so only the aerosol and dry air from the sheath flow are received. A photo of the SSPD during operation is shown in Figure 3.2.2a. Two cyclones (internally called cyclone2 and cyclone3) were placed behind the SSPD to filter larger aerosol particles before being dispersed into the chamber.

Compared to the RBG, the SSPD provides better control to achieve low aerosol number concentrations.

Sulfuric acid vaporizer

Sulfuric acid solution particles are produced with the sulfuric acid vaporizer. A schematic of a possible setup is shown in [Figure 3.2.2b](#).

Highly concentrated sulfuric acid is heated in a glass tube to around 140 K. The sulfuric acid evaporates in the glass tube and a flow of synthetic air transports it off. H_2SO_4 is highly hygroscopic and nucleates to aqueous droplets with at very low water vapor. Once the evaporated H_2SO_4 reaches an environment with water vapor an aerosol distribution forms.

In [Figure 3.2.2b](#) the setup is shown, which was most commonly used in the conducted experiments. One flow goes through the H_2SO_4 reservoir and the other flow has the purpose to dilute the flow before it enters the humid environment of our aerosol chamber [AIDA](#). For the early campaigns an un-optimized setup without the dilution flow was used.

3.2.8 Aerosol size distribution measurements

The dispersed aerosol populations were characterized at the [AIDA](#) cloud chamber according to their [PSD](#). Therefore [aerodynamic particle sizer \(APS\)](#) and [scanning mobility particle sizer \(SMPS\)](#) instruments were used.

Aerodynamic particle sizer

An [APS](#) can measure the aerodynamic diameter of aerosol by determination of its terminal settling velocity.

The used [APS](#) instrument (model APS-3321, TSI®) is internally labeled APS3. It covers the size range from 0.5 μm to 20 μm .

For the conversion from the aerodynamic diameter to the volume-equivalent sphere diameter the aerosol particle density and a valid estimate for the dynamic shape factor must be known. The dynamic shape factor is typically between 1.1 and 1.6. The dynamic shape factor has to be estimated from comparisons to size distributions derived from other techniques (e.g. from an [SMPS](#)).

Scanning mobility particle sizer

A scanning mobility particle sizer (**SMPS**) measures the mobility diameter of dispersed particles. It is a combination of a **differential mobility analyzer (DMA)** with a **CPC**. The **DMA** separates the particles of a sampled air flow according to their mobility, by ionizing the particles and guiding them through an electric field. The remaining particles of a certain mobility are then counted using the **CPC**. By varying the electric field a size spectrum can be probed. The **SMPS** can measure particles with a mobility diameter between 0.014 μm and 0.82 μm .

Size distribution measurements from **APS** and **SMPS** can be merged after conversion to a volume-equivalent sphere diameter. With the combination of both instruments it is possible to cover a broad size range for aerosol particles.

A **SMPS** model 3071 A from TSI® company (discontinued since 1999) was used. The device is internally labeled 'SMPS2'. The **CPC** in this setup was also a CPC-3010 as mentioned in [section 3.2.6](#). It should be noted, that the **SMPS** showed artifacts for number concentrations below 10 cm^{-3} . The measured data showed multiple random bins with an unreasonably high number concentrations. Therefore, the **SMPS** size distribution measurements are neglected when possible and only the **APS** data is used. However, fumed silica showed such a small size distribution that is necessary to include also the **SMPS**, into the analysis.

3.2.9 Filter sampling and ESEM analysis

Filters of dispersed aerosol samples were collected from the **AIDA** cloud chamber. A filter with fumed silica was sampled from **AIDA** during the campaign AWICIT01B. For calcium carbonate two filters of dried and untreated CaCO_3 were analyzed. The two filters were sampled from **AIDA** during the campaign AWICIT04. A filter for quartz has not been sampled, since this aerosol type was added at a later stage (starting with AWICIT05) and no further **ESEM** image analysis was planned at this point.

The Whatman® Nuclepore™ filters with a pore size of 0.2 μm were sampled with a mass flow rate of $2\text{ l}_{\text{std}}\text{ min}^{-1}$ through a filter holder..

Microscopy images were taken with an environmental scanning electron microscope (**ESEM**), which has a size resolution down to tens of nanometers. The images are shown in [section 5.1.1](#) and provide an impression of the surface structure of the aerosol particles.

3.2.10 Standard procedure for our AIDA expansion experiments

In this section the steps of standard AIDA expansion experiments are described. Systematic deviations for specific campaigns are listed afterwards.

Cleaning cycle First the chamber has to be cleaned, which is accomplished through multiple flushes with synthetic air. After a cleaning program the chamber is filled with a specified amount of water vapor and synthetic air containing oxygen and nitrogen.

Check for contaminations The CPC is used to check if the chamber is clean. A concentration around 0.1 cm^{-3} is a typical background at clean conditions. If the contamination is considered too high a reference activation can be conducted. Therefore the pumps are started to quickly increase the saturation ratio in the chamber in order to remove all available INPs from the system. Once they nucleated to ice crystals they sediment out quickly.

Start and calibrate SIMONE A background check is conducted for 2 min to 5 min to adjust SIMONE to the current level of remaining background contamination.

Injection of aerosol If heterogeneous INPs are desired for the experiment, they are introduced using the RBG or the SSPD. In parallel the evolution of the arising aerosol number concentration is monitored with the CPC. To generate sulfuric acid solution droplets the sulfuric acid vaporizer is used.

Size distribution measurement of solid aerosol After each injection of into the chamber measurements with the APS and SMPS are conducted simultaneously. Typically a second backup measurement is performed.

Expansion experiment Starting the pumps sets the beginning of an expansion experiment. Once the cloud formation is over the operator can stop the pumps, shut down the instrumentation and start a cleaning cycle for the next run. Typically a daily series of 2 to 3 experiments can be conducted.

3.3 AIDA campaign overview

Seven measurement campaigns were conducted at the AIDA cloud chamber facility between March 2017 and August 2019. The objectives and characteristics of each campaign are described in the text below, respectively. Since the procedures developed over time the provided information is important for any inter-comparability between the individual campaigns and experiments. A complete list of all AIDA expansion experiments with the important key parameters can be found in Table D.0.1 of appendix D.

Campaign AWICIT01B

Table 3.3.1 Instrumentation used at the AIDA facility during the campaign AWICIT01B.

Measured quantity	Instrumentation
temperature & pressure	AIDA logging system
gas water content	APicT
total water content	MBW, APeT
forward/backward scattering	SIMONE
aerosol number concentration	CPC3010-1
optical particle counter	sensor welas1 sensor welas2 (partially unstable)
INP dispersion	RBG with cyclones 2 & 3
H ₂ SO ₄ dispersion	H ₂ SO ₄ vaporizer (directly into AIDA)
aerosol size distribution	APS-3, SMPS-2

In the first campaign AWICIT01B¹ the deposition freezing behavior of fumed silica, the homogeneous ice-nucleation of sulfuric acid ASPs were investigated. and performed first experiments on the competition between both freezing modes. The chamber was operated at temperatures in the range of 210 K to 230 K and pump rates varied between 50 % to 80 % power of pump 2 (P2). A list of the instruments used during this campaign is provided in Table 3.3.1.

For the generation of ASPs the H₂SO₄ vaporizer was used. The H₂SO₄ vaporizer was set to operate at temperatures in the range of 139 °C to 142 °C. The synthetic air first flushes continuously over the heated H₂SO₄ reservoir into the return line. It turned out that the number concentration of ASPs couldn't be well controlled through this technique.

¹The suffix *B* derives from a re-initialization of the campaign that was necessary due to a software issue.

While aiming for 50 cm^{-3} , often high [ASP](#) number concentrations of several hundred cm^{-3} were reached. The size distribution wasn't reproducible through this technique and varied between a single size mode or a bimodal size distribution.

The [OPC](#) sensor *welas2* didn't work stable for three experiments (IDs 3608, 3625 and 3628). For those experiments the analysis of [OPC](#) data is limited to sensor *welas1*. After the campaign it turned out that the mixing fan of the chamber might have worked only with reduced power during the campaign. This fits to deviations seen in comparison to other campaigns when calculating the heat and water flux from the chamber walls (see [section 5.3.1](#)). The fan was repaired after the campaign.

Within this first campaign a number of experiments with a well pronounced separation of heterogeneous and homogeneous freezing (e.g. exp. ID 3610) could be conducted.

Campaigns [AWICIT02](#) and [AWICIT03](#)

Table 3.3.2 Instrumentation used at the [AIDA](#) facility during the campaigns [AWICIT02](#) and [AWICIT03](#).

Measured quantity	Instrumentation
temperature & pressure	AIDA logging system
gas water content	APicT
total water content	MBW , APeT
forward/backward scattering	SIMONE
aerosol number concentration	CPC3010-1
optical particle counter	sensor <i>welas1</i> sensor <i>welas2</i> (with control unit of <i>welas3</i>)
INP dispersion	RBG with cyclones 2 & 3
H_2SO_4 dispersion	H_2SO_4 vaporizer (directly into NAUA)
aerosol size distribution	APS-3 , SMPS-2

The campaigns [AWICIT02](#) and [AWICIT03](#) are discussed together since they were conducted with a very similar setup and with just a break of less than one month in between. The objective was to observe [AIDA](#) expansion experiments with competition of heterogeneous and homogeneous freezing under systematic parameter space variations. Starting temperatures, pump rates and the number concentrations of [INPs](#) and [ASPs](#) were varied. The starting temperatures were 210 K, 220 K and 230 K and pump rates were either 50 % or 80 % using pump 2 (P2).

A different method to generate ASPs was tested, because in the previous campaign the number concentration was hard to control and the aerosol size distributions couldn't be reliably reproduced. For AWICIT02 and AWICIT03 the H₂SO₄ vaporizer was attached to our smaller aerosol chamber NAUA, which was prepared with a clean and dry atmosphere. The vaporizer was used at NAUA as described for AWICIT01B and the chamber served as an reservoir for ASPs. A small differential pressure between NAUA and AIDA transferred the ASPs through a pipe from NAUA to AIDA. Through this technique the ASP number concentration could be controlled nicely.

In contrast to the first campaign, the ASP size distributions showed much smaller particles in the range of 20 nm to 30 nm. The competition between heterogeneous and homogeneous freezing could not be well characterized since the INP number concentration turned out to be too high in many experiments.

Campaign AWICIT04

Table 3.3.3 Instrumentation used at the AIDA facility during the campaign AWICIT04.

Measured quantity	Instrumentation
temperature & pressure	AIDA logging system
gas water content	APicT
total water content	MBW, APeT
forward/backward scattering	SIMONE (maintenance in between)
aerosol number concentration	CPC3010-1
optical particle counter	sensor welas1 (overload errors, switched to welas3 control unit), sensor welas2
INP dispersion	RBG (replaced stamp seal on 2018-01-18), cyclones 2 & 3
H ₂ SO ₄ dispersion	H ₂ SO ₄ vaporizer (diluted into AIDA)
aerosol size distribution	APS-3 (some runs lost due to software crashes) SMPS-2

For this campaign the method to generate ASPs was modified once more. The chamber NAUA wasn't used any more as aerosol reservoir. The new setup is comparable to the one in campaign AWICIT01B, but with an additional gas line diluting the H₂SO₄ gas mixture with another flow of synthetic air. A mass flow controller (MFC) regulates the flow through the heated H₂SO₄ reservoir and another MFC is used for the dilution flow. After some tests a flow of 0.75 l_{std} was chosen for the former and 5 l_{std} for the latter.

With a valve one can direct the flow either into the return line or into the AIDA chamber. Before opening the valve to the chamber a stable flow into the return line was ensured. With this technique the ASP number concentration increased slow enough that a value of 50 cm^{-3} could be realized within $\pm 10\%$. The ASP size distribution showed larger particles compared to the previous technique using NAUA as intermediate reservoir. The size distributions turned out to be well reproducible.

During AWICIT04 expansion experiments with reproducible ASP backgrounds and various INP number concentrations were conducted. The starting temperature was varied between 210 K, 220 K and 230 K. Furthermore it was investigated if the ice-activity of the INPs is affected by drying the aerosol bulk sample. Therefore a fraction of the CaCO_3 sample was dried for one week at 60°C in the oven. However, no significant effect regarding the ice-activity during AIDA expansion experiments could be seen.

During the campaign filter samples were collected with the dried and the untreated CaCO_3 aerosol from the chamber. Also a comparison with the ESEM did not show to any significant differences between the two filter samples.

Two catch-up experiments investigating pure homogeneous freezing were conducted two month after the main campaign period (exp. IDs 3895 and 3896). In the meantime SIMONE had received improvements, which however doesn't affect the general comparability to previous experiments.

Campaigns AWICIT05 and AWICIT06

Table 3.3.4 Instrumentation used at the AIDA facility during the campaigns AWICIT05 and AWICIT06.

Measured quantity	Instrumentation
temperature & pressure	AIDA logging system
gas water content	APicT (instable at low temp)
total water content	MBW, APeT
forward/backward scattering	SIMONE
aerosol number concentration	CPC3010-1
optical particle counter	sensor welas1 sensor welas2
INP dispersion	SSPD with cyclones 2 & 3
H_2SO_4 dispersion	H_2SO_4 vaporizer (diluted into AIDA)
aerosol size distribution	APS-3, SMPS-2

With campaign AWICIT05 quartz was added as third INP and started to use the SSPD to disperse the bulk powder samples into AIDA (see section 3.2.7). In comparison to the RBG the number concentration of the INPs could be controlled better using the SSPD. For most of the experiments of AWICIT05 an issue introducing humid air from the lab into the aerosol flow persisted. Starting with exp. ID 4032 the setup was modified to first flush the aerosol flow into the return line before opening the valve to the AIDA cloud chamber, which solved the issue of initial ice-nucleation events when opening the valve to the chamber. Especially for the lower temperatures at ~ 210 K the sheath flow has to be strong enough to shield humid air effectively. If the sheath flow isn't strong enough humidity from the lab can enter the aerosol air flow and leads to cloud formation when entering the cold chamber atmosphere.

Based on reliable and reproducible procedures to create INP- and ASP PSDs the campaigns AWICIT05 and AWICIT06 led to a highly valuable dataset about the competition between heterogeneous and homogeneous freezing.

For experiments at 210 K a slow but steady increase in the number concentration after introducing sulfuric acid into the chamber could be observed. During exp. ID 3989 the particle formation was tracked from 50 cm^{-3} to 150 cm^{-3} within 2 h. Within this period 14 combined PSD measurements were performed with the APS and SMPS. A new particle mode forming could be seen in the SMPS size range between 20 nm and 50 nm, which couldn't be explained at that time. However, while having the intentionally introduced aerosol particles in the chamber the new particle mode couldn't be observed to affect the ice-nucleation observed in the experiments. Therefore the experiments are analyzed without paying respect to the new particle mode. Later the explanation was found that the amount of water added during chamber preparation was too much, creating an ice spot where local supersaturation could lead to new particle formation. In a later campaign (unrelated to this work) the added water content was reduced which solved the issue.

Campaign TROPIC02

Motivated by overlapping scientific objectives the campaign TROPIC02 was conducted in cooperation with another PhD student, Julia Schneider, and partners from [Forschungszentrum Jülich \(FZJ\)](#) from the group around Martina Krämer. One of the main goals was to conduct experiments filling gaps in the parameter space, which were yet open from the previous campaigns. In comparison to the previous campaigns the chamber was also operated at 200 K and 205 K. Moreover the effect of pump rate variations was investigated.

The procedures for aerosol generation were conducted as described for the campaigns AWICIT05 and AWICIT06.

Table 3.3.5 Instrumentation used at the [AIDA](#) facility during the campaign TROPIC02.

Measured quantity	Instrumentation
temperature & pressure	AIDA logging system
gas water content	APicT
total water content	MBW , APeT
forward/backward scattering	SIMONE
aerosol number concentration	CPC3010-1
optical particle counter	sensor welas1 sensor welas2 NIXE-CAPS (external device, from FZ Jülich)
INP dispersion	SSPD with cyclones 2 & 3
H ₂ SO ₄ dispersion	H ₂ SO ₄ vaporizer (diluted into AIDA)
aerosol size distribution	APS-3 , SMPS-2

The group from [FZJ](#) had brought their instrument [NIXE-CAPS](#), which is a cloud particle spectrometer. It can detect the phase and size of cloud particles within sizes from 0.6 μm to 900 μm . Multiple technical problems occurred with the connection between [NIXE-CAPS](#) and [AIDA](#), hence its data could not be quantitatively included into the presented work. However the instrument data indicated a significant source of water in the system, which motivated to model the water flux from iced inner chamber walls (see [section 5.3.1](#)).

During TROPIC02 the new particle formation after introducing H₂SO₄ particles at temperatures $\leq 210\text{K}$ could be observed again. Still, this interfered neither with the scientific objectives nor with the data analysis and could be solved in a later campaign.

3.3.1 Parameter space covered by [AIDA](#) campaigns

Within seven measurement campaigns 168 expansion experiments were conducted, without counting reference activations.

To investigate the competition between heterogeneous and homogeneous freezing mainly the temperature, the [INP](#) number concentration and the [INP](#) type were varied. For a broader base of comparable experiments the parameters of [ASP](#) number concentration and pump rate were kept fixed for most experiments. They were only varied for a minor subset, so allow also model comparisons to experiments in this extended area of the parameter space.

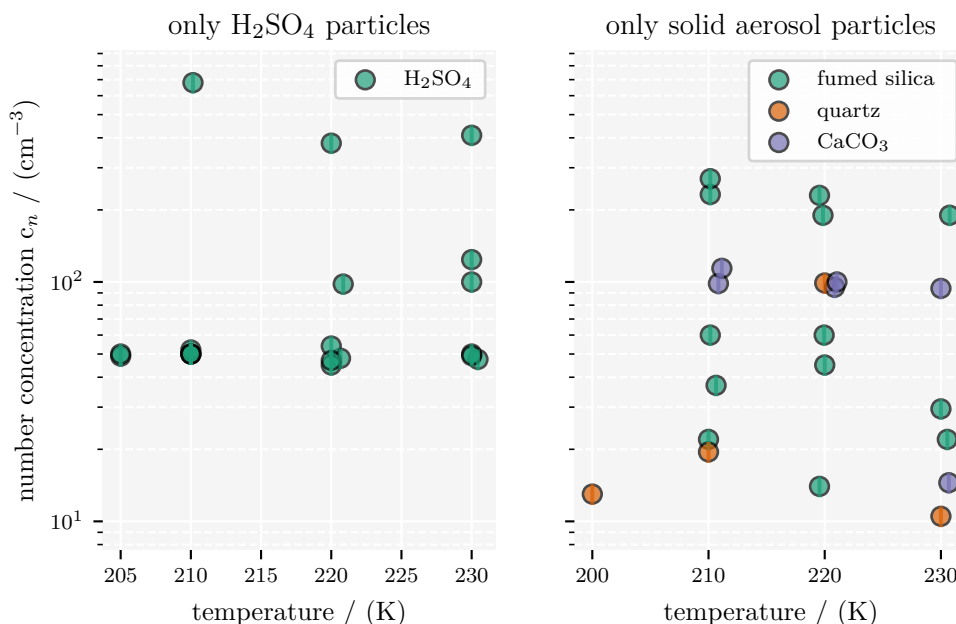


Figure 3.3.1 Number concentrations c_n of AIDA experiments with individual aerosol populations as a function of start temperature. The graph on the left shows the number concentration for experiments with only H_2SO_4 particles. The right graph shows the number concentration for the three heterogeneous INP aerosol types *fumed silica*, *quartz* and *calcium carbonate*.

We conducted 47 experiments with a starting temperature ~ 230 K, 48 at ~ 220 K and 62 at ~ 210 K. In the last campaign we extended the parameter space to even lower temperatures with 5 experiments at ~ 205 K and two experiments at ~ 200 K. The varying number concentrations for experiments investigating the ‘pure’ heterogeneous or homogeneous freezing are shown as a function of temperature in [Figure 3.3.1](#). The combinations of varying number concentrations for ‘mixed’ experiments, conducted with ASPs and INPs, are shown in [Figure 3.3.2](#).

To observe the competition between homogeneous and heterogeneous freezing we had to realize INP number concentrations $< 10 \text{ cm}^{-3}$. At such low number concentrations we are close to the detection limit for number concentrations with the optical particle counters.

3.4 AIDA data analysis

This section describes important aspects of the experimental data analysis. Specific software projects, which were developed in context of this work, are presented. Subsequently procedures of the data analysis are presented with a focus on PSDs and OPC data.

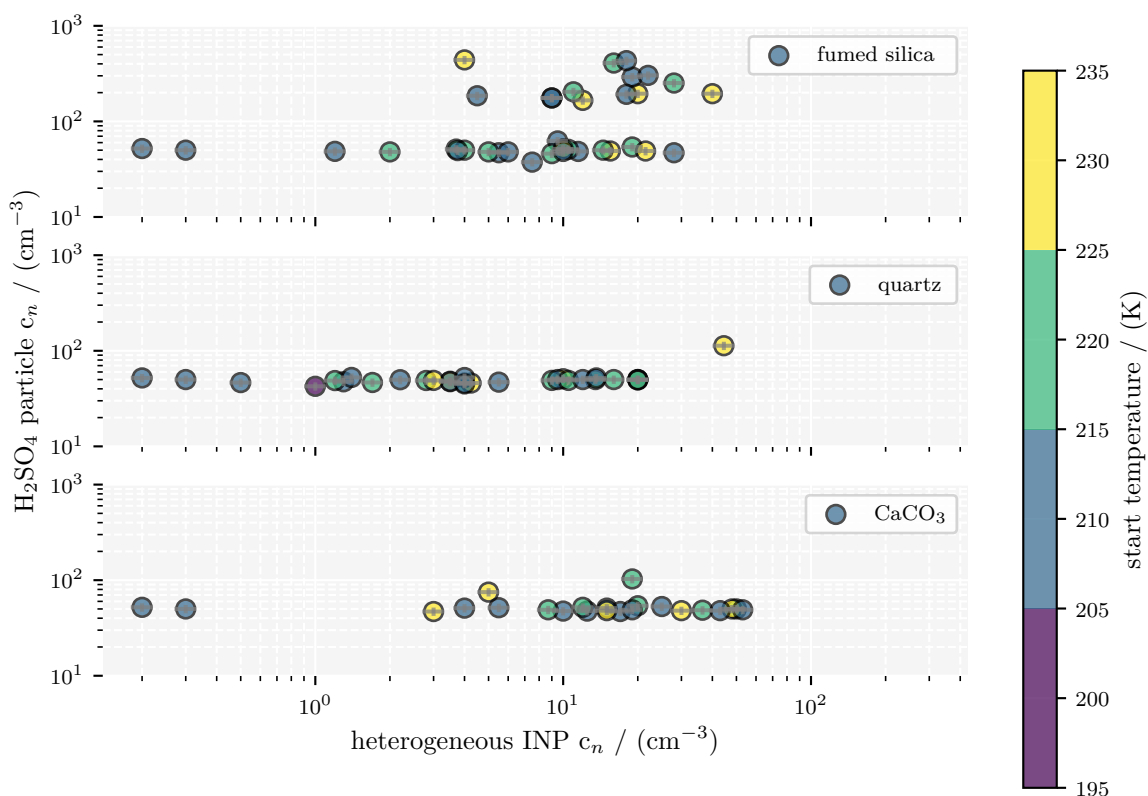


Figure 3.3.2 Number concentration (c_n) combinations of AIDA experiments with mixtures of heterogeneous INPs and sulfuric acid ASPs. The three panels refer to the three heterogeneous INP aerosol types *fumed silica*, *quartz* and *calcium carbonate*.

3.4.1 Developed analysis software

Here a brief description about two data analysis software projects, which were developed within this work, is given. They allow an easy analysis of the data acquired at the AIDA cloud chamber facility. Both projects query raw data from the data infrastructure at KIT/IMK-AAF, as depicted in Figure 3.4.1.

AIDA experiment analysis software

The python-based framework named *aida_experiment_analysis* was developed for the analysis of AIDA experiments. The previously preferred analysis framework was written in IDL. The new framework has a major part of the old functionality re-implemented and received new functionalities.

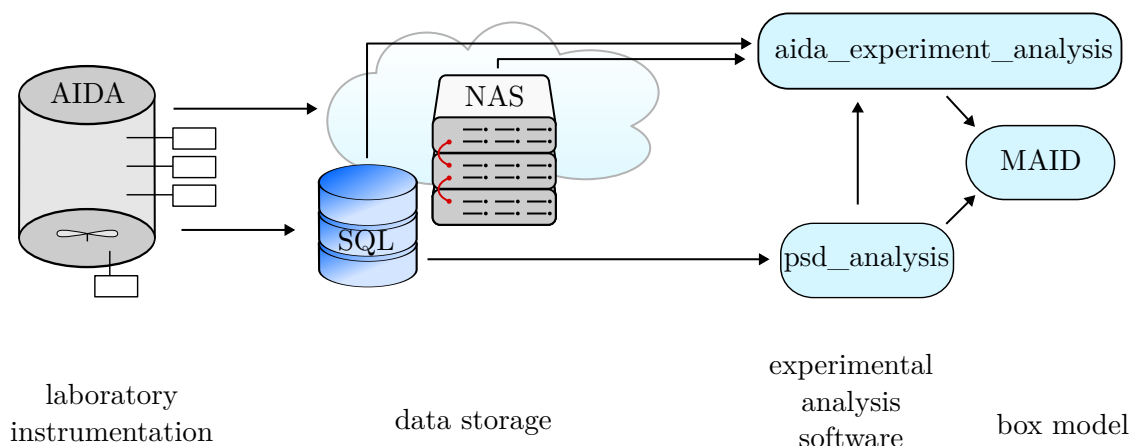


Figure 3.4.1 Schematic of the data flow within the developed software frameworks.

New functionalities include calculation of **INAS** densities for deposition freezing experiments and an analysis of the wall flux. Through an entry-function users can utilize all implemented functionalities by specifying well documented keyword arguments. Raw data, processed data and metadata of **AIDA** experiments can be easily collected and exported. Detailed overview plots can be generated on the fly or customized through a generalized function.

The code is publicly available in a remote [git](#) repository under an open license [69].

Size distribution analysis software

For the analysis of **PSDs** a python-based framework name *psd_analysis* was developed. It provides functionalities to analyze **PSD** data with a focus on **APS** and **SMPS** data. The main user-function relies on access to the **IMK-AAF structured query language (SQL)** database, where the raw data is stored. Otherwise, custom **PSDs** can also be processed, once they are converted to the right format.

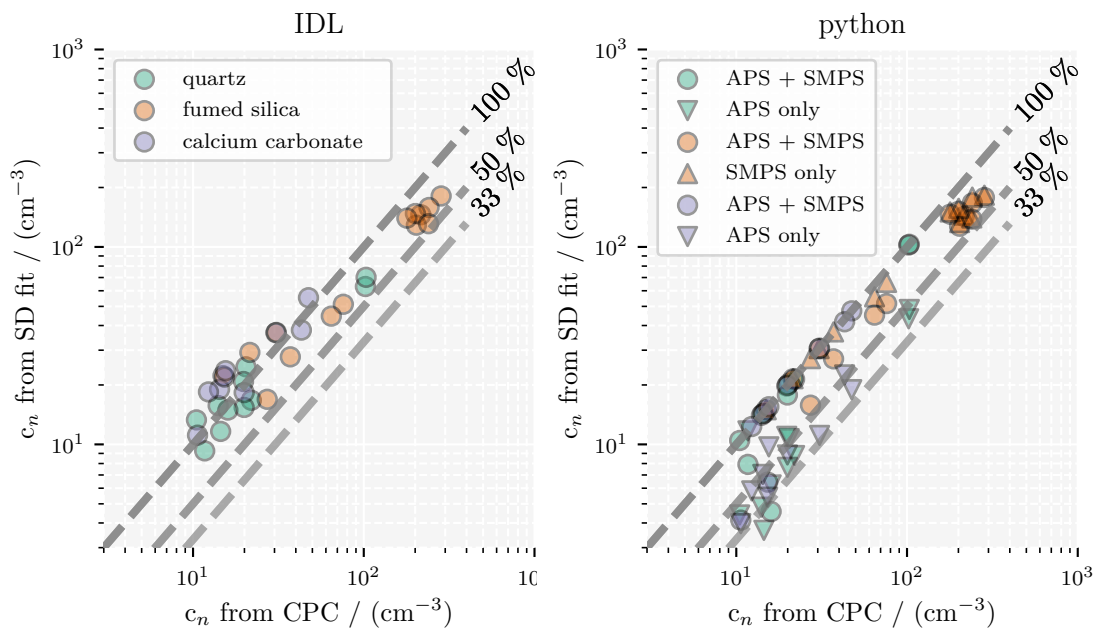
The functionality of the project covers

- ◇ import of raw **PSDs** from the **AAF** database
- ◇ converting **APS** and **SMPS PSDs** to be based on an equivalent sphere diameter
- ◇ gap interpolation between datasets or merging of overlapping data
- ◇ Fitting of size distributions (lognormal, bi-lognormal).

The code is publicly available in a remote [git](#) repository under an open license [70].

3.4.2 Aerosol size distribution fitting

The so far established [PSD](#) analysis scripts were implemented with [IDL](#) and are provided by the facility. With the `psd_analysis` project a new python-based implementation is available, providing more options for the [PSD](#) analysis. This section provides a brief comparison between the two analysis frameworks and shows differences when using only either the [APS](#) or [SMPS](#) data.



a) Comparison of IDL fits with CPC.

b) Comparison of `psd_analysis` fits with CPC.

Figure 3.4.2 Fit parameters of lognormal functions fitted to particle size distributions. The established IDL routines were used in the left panel, the new python-based framework `psd_analysis` was used on the right. The colors in b) match the legend in a). b) shows beside the combined fits (APS+SMPS) also the fit of only SMPS for fumed silica and the fit of only APS for quartz and calcium carbonate.

Figure 3.4.2 shows the number concentration derived from a lognormal fit for the three INP types in comparison to the CPC number concentration in AIDA during the PSD measurement. Figure 3.4.2a shows the comparison using the IDL framework, whereas in Figure 3.4.2b the new `psd_analysis` framework is used.

In Figure 3.4.2a the fitted total number concentration scatters around the CPC value without a clear bias. When looking into the individual fit curves it can be seen that the

fitted curves often do not capture the shape of the measured size distribution. Those lognormal curves have a strong variability in the geometric standard deviation (not explicitly shown here). This variability is depicted in an aggregated form in the left subplot of Figure 5.1.2 of the results section 5.1.2.

Figure 3.4.2b shows the same analysis with the python-based framework and differentiates between fits of the whole dataset (APS & SMPS) and fits using only one of the devices. This selection was made because the APS and SMPS measurements didn't work equally well for all aerosol types. The size distribution of fumed silica turned out too small for size range of the APS, thus we can neglect the APS for this aerosol type. However, as discussed in section 3.2.8, the SMPS did not work reliably for lower number concentrations. For CaCO₃ and quartz we typically see a well pronounced right tail of the PSD in the APS. Therefore, for these two aerosol types we can neglect the unclear SMPS data.

The fits in Figure 3.4.2b for quartz and calcium carbonate show a tendency to underestimate the total number concentration when fitted only to the APS data. The limitation on the SMPS data for fumed silica improves the alignment to the CPC concentration especially for lower number concentrations.

To account for the deviations from the CPC number concentration the size distributions are finally fitted by constraining the number concentration of the fit to the value from the CPC. The respective results are presented in section 5.1.2.

3.4.3 Separation between heterogeneously and homogeneously formed ice

Experimentally the total ice crystal number concentration $n_{\text{ice}}^{\text{tot}}$ is measured with the welas OPC system (see section 3.2.5). If we assume during an expansion experiment that heterogeneous ice forms exclusively before the homogeneous freezing onset, we can separate the two freezing mechanisms from another.

Therefore each experiment gets individually checked for the timestamp of the homogeneous freezing onset t_f^{hom} . The determination of t_f^{hom} is achieved by manual inspection of the OPC single particle data and the light scattering data from SIMONE. In general SIMONE is more sensitive on changes in the ice crystal concentration, so a kink in the data can be typically interpreted as the homogeneous freezing onset. However, for experiments with strong competition of heterogeneous and homogeneous ice formation the amount of homogeneously formed ice can be low and the freezing onset can be diffusive.

Ice which formed before t_f^{hom} is considered heterogeneously formed ice and contributes to $n_{\text{ice}}^{\text{het}}$. The ice which formed after t_f^{hom} is considered homogeneously formed ice and is

derived by

$$n_{\text{ice}}^{\text{hom}}(t) = n_{\text{ice}}^{\text{tot}}(t) - n_{\text{ice}}^{\text{het}}(t_f^{\text{hom}}). \quad (3.1)$$

Due to the short timescale of expansion experiments (3 min to 10 min) we don't take particle losses into account.

3.4.4 Fit of INAS density parameterizations

Parameterizations of **INAS** densities can be derived from the **OPC** ice crystal number concentrations n_{ice} . In the following the procedure is described, which was used to derive **INAS** density parameterizations for the heterogeneous **INP** used in this work. The corresponding code is located in 'calc_inas.py' and 'fit_inas_awiclit.py' of the **AIDA** analysis repository [69].

The **INAS** density $n_s(T, S_{\text{ice}})$ gets derived based on [equation \(2.12\)](#), which requires information about the initial **INP PSD** and the ice number concentration $n_{\text{ice}}(T, S_{\text{ice}})$.

The **PSD** is described by a lognormal fit of the measured aerosol size distribution (see [section 3.2.8](#)). The surface S of an aerosol particle is derived from its radius under the assumption of a spherical shape.

The time-resolved ice crystal number concentration $n_{\text{ice}}(t)$ of an **AIDA** experiment is derived from the **OPC** data, by applying a size threshold to distinguish between ice and other aerosol particles. If the experiment includes also homogeneous freezing the trajectory has to be cut off before homogeneous ice forms, since the **INAS** density describes only the formation of heterogeneous ice. Further n_{ice} is smoothed with a Savitzky-Golay filter to reduce the impact of noise. The heterogeneously formed ice crystal number concentration $n_{\text{ice}}^{\text{het}}(T, S_{\text{ice}})$ is derived as a trajectory in the parameter space of temperature T and saturation ratio S_{ice} .

During an **AIDA** experiment the measured number concentration drops, due to the expansion of the air. Therefore the ice crystal number concentration has to be corrected by multiplication with the factor $\frac{p(t_0)}{p(t)}$. Further only the data points of monotonous increasing $n_{\text{ice}}^{\text{het}}$ are used. If the data hasn't been smoothed earlier the noise would lead to a significant loss of data points in this step.

Finally $n_s(T, S_{\text{ice}})$ is fitted according to [equation \(2.12\)](#) with respect to $n_{\text{ice}}^{\text{het}}(T, S_{\text{ice}})$, the **INP PSD** and the respective aerosol surface S . Since the equation can't be explicitly solved for n_s it is solved numerically using the Nelder-Mead method with a start parameter of $n_s = 1 \times 10^9 \text{ m}^{-2}$.

After n_s is derived from the total heterogeneous ice crystal number concentration $n_{\text{ice}}^{\text{het}}(T, S_{\text{ice}})$, the proportional contribution of individual size bins can be calculated through the same formula (equation (2.12)).

3.4.5 Cirrus thinning effect in cloud chamber experiments

The competition between heterogeneous and homogeneous freezing is investigated by comparing experiments that are conducted with similar ASP number concentrations and different INP populations. The INPs are varied with respect to their number concentration and type. The types are fumed silica, quartz and calcium carbonate.

The total ice crystal number concentration $n_{\text{ice}}^{\text{tot}}$, which includes heterogeneously and homogeneously formed ice, is compared to the fraction of heterogeneously formed ice. The analysis is applied only on a selected subset of the conducted expansion experiments. From all AIDA expansion experiments we selected only experiments which fulfilled the following criteria:

- ◇ INP number concentration $>0 \text{ cm}^{-3}$
- ◇ ASP number concentration within $50(10) \text{ cm}^{-3}$
- ◇ no experiments from the campaigns AWICIT02 or AWICIT03 due to a different method of ASP generation

The total ice crystal number concentration $n_{\text{ice}}^{\text{tot}}$ was measured with the two OPC sensors *welas1* and *welas2*, of which we used the average when both devices were operated. A separation of $n_{\text{ice}}^{\text{tot}}$ into fractions of heterogeneously and homogeneously formed ice was conducted as described in section 3.4.3.

The results are shown and discussed in the results chapter in section 5.2.3.

3.5 Cloud chamber wall effects

When comparing a cloud chamber experiment with processes in the real atmosphere the interaction with the chamber walls have to be taken into account. When starting an AIDA expansion experiment the air pressure and air temperature drop. However, the AIDA passively cooled chamber walls change their temperature only comparably slow, which leads to a temperature gradient between the chamber walls and the inner gas. This thermal gradient drives a heat flux, which causes the actual gas temperature profile to deviate from an adiabatic profile.

The wall interaction can also affect the water vapor pressure in the chamber if the chamber walls are covered with ice. If we start an expansion experiment at ice-saturated conditions, the water vapor saturation pressure over the iced walls is higher than the water vapor pressure in the chamber as soon as the gas temperature drops and the water vapor gets depleted from ice formation. This leads to sublimation of ice on the chamber walls, which is proportional to the iced surface area and the difference between the water vapor pressure in the gas phase $p_w(T_g)$ and the water vapor saturation pressure $p_w,0(T_w)$ over the ice-covered wall.

Three different approaches are used to quantify the wall fluxes for each expansion experiment.

The first wall flux approach, is based on a fluid dynamic description of heat and mass transport under forced and natural convection. In this approach the heat and water wall flux are parameterized by two fit factors, which are multiplied with the gradients between the chamber walls and the inner gas. Both parameters are fitted based on reference reference activations (or reference expansions). Since reference expansions include the typical expansion dynamics, but no significant ice formation acting as an additional water sink, they are optimally suited to fit derive the wall flux fit parameters for [AIDA](#) experiments.

The second wall flux approach was derived by Cotton et al. [13]. The approach is simpler than the fluid dynamic approximation, but relies similarly on two fit parameters based on the gradients between chamber gas and wall [13, eq. (4) and (5)]. As explained for the fluid dynamic approach, reference expansions are utilized to derive the fit parameters.

The derivation of the wall flux parameterizations happens in a two-step process. First, the two fit parameters of each reference expansion are fitted with respect to the actual temperature profile or water vapor profile, respectively. We exclude the reference expansions from the first campaign AWICIT01B, due to issues on the mixing fan. To account for a temperature dependence of the fit parameters, they are further parameterized using an ordinary least square fit as a function of the starting temperature of the expansion experiments. The resulting parameterizations are presented in [section 5.3.1](#).

A third wall flux approach is based on the [MBW](#) measurements. This approach describes only the water wall flux, not the heat flux. Without any sinks or sources of water the water vapor mixing ratio should remain constant during an expansion. However, if a flux of water occurs from the wall will increase the measured total water mixing ratio $r_{\text{H}_2\text{O}}$. The change $\Delta r_{\text{H}_2\text{O}}^{\text{flux}}$ is given by

$$\Delta r_{\text{H}_2\text{O}}^{\text{flux}}(t) = r_{\text{H}_2\text{O}}(t) - r_{\text{H}_2\text{O}}(t_0) \quad (3.2)$$

with t_0 referring to the start of the expansion. Note that this approach is considered the least reliable, since the quality of the [MBW](#) data decreases strongly for low gas water contents at low cirrus temperatures. Still, through this approach we can derive an

3.5 *Cloud chamber wall effects*

estimate of the water wall flux directly from the measured data, without the need of any fit parameters.

Chapter 4

MAID – Model for Aerosol and Ice Dynamics

In this work the model [MAID](#) is used to simulate cirrus cloud formation with a competition between homogeneous and heterogeneous freezing. It is applied on large simulation ensembles representing [CCT](#) scenarios.

The model [MAID](#) ([Model for Aerosol and Ice Dynamics](#)) is a numerical Lagrangian parcel model to simulate cloud formation under [UTLS](#) conditions. The model was first introduced by Bunz et al. [[11](#)] and specifically improved within this work

The code is written in Fortran and is highly efficient. A typical updraft scenario can be computed within far less than a minute using an average consumer CPU model. Sets of multiple scenarios can be parallelized, scaling the efficiency linearly with the number of available threads.

The model was open-sourced in December 2023 . The code is publicly available under an open license and provided with a web documentation [[71](#)].

Each model run is based on an initialization file, which holds all basic information about the starting conditions, trajectory dynamics and selected parameterizations. A detailed summary of all model parameters can be found in the web documentation.

4.1 Model features

4.1.1 Selectable trajectory types

The trajectories of air temperature and pressure can be specified in two distinct categories: internal and external trajectories. The possible options to define a trajectory are depicted in [Figure 4.1.1](#).

For the internal trajectories one has to specify the starting conditions (T_0, p_0) and an

updraft velocity w . The trajectory then follows an adiabatic profile. The end of the trajectory can either be defined by a final pressure value (i1) or by a fixed simulated runtime (i2). With the use of trajectories driven by external data, the ambient conditions follow the values from an external trajectory file. This option allows to run also non-adiabatic trajectories along pre-defined pathways (e1). With additional columns in the trajectory file it is possible to provide time-resolved sinks/sources for the condensable gas components, such as water vapor (e2).

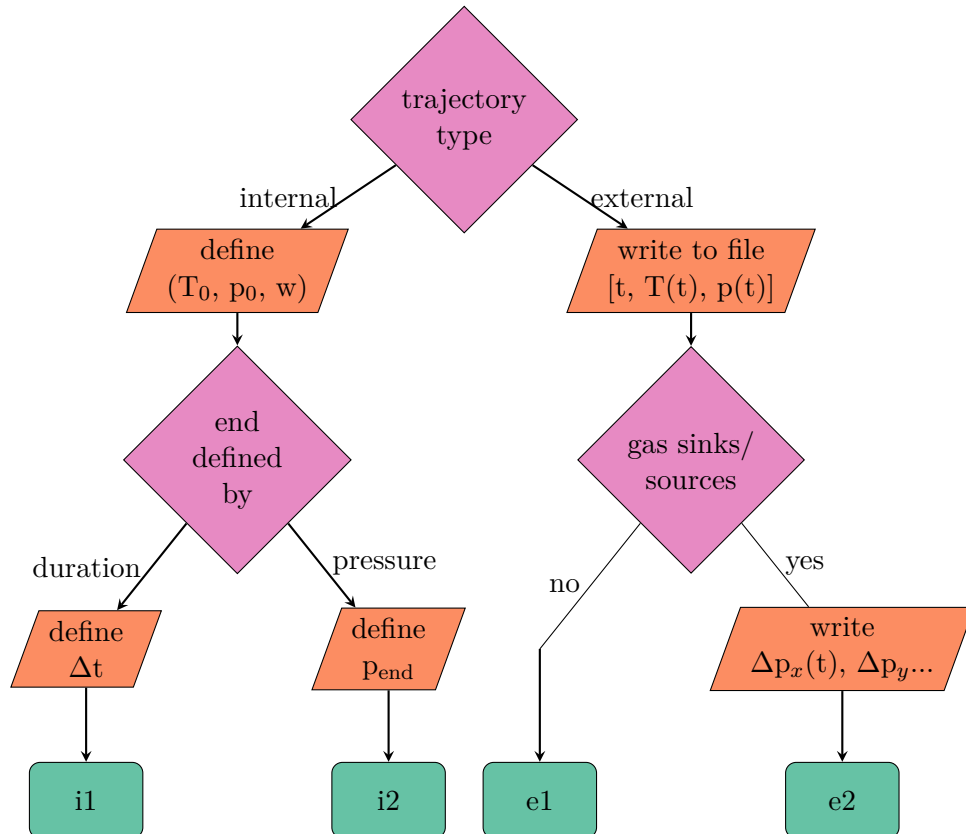


Figure 4.1.1 Decision graph for MAID trajectories. Depending on the users choices trajectories can be specified in four different ways. Options i1 and i2 use internally calculated adiabatic trajectories and differ only in the criteria for the trajectory to end. With i1 the model finishes after a fixed simulated runtime Δt , whereas with i2 the model finished once a certain final pressure p_{end} is reached. External trajectories are covered by option e1 and e2. The latter is similar to e1, but extended with additional columns specifying time a resolved sink/source for specified gases.

4.1.2 Aerosol particle types

The model has three aerosol types implemented: sulfuric acid [aqueous solution particles \(ASPs\)](#), solid [ice-nucleating particles \(INPs\)](#) and ice crystals. Each can be initialized as a [lognormal particle size distribution \(PSD\)](#).

ASP can be a mixture of water and sulfuric acid (H_2SO_4), nitric acid (HNO_3), hydrogen bromide (HBr) and hydrogen chloride (HCl). With the exception of H_2SO_4 , all constituents can also be present in their gas phase. Their composition is balanced during model runtime according to the partial pressure of the respective components, being closer described in [section 4.1.4](#). INP PSDs are defined by their size distribution and a respective density. The ice crystal PSD typically forms dynamically during the model run from frozen soluble or solid particles. Alternatively an ice crystal size distribution can be initialized at the start.

4.1.3 Freezing mechanisms

The ASP PSDs can freeze **homogeneously** as described in [section 2.2.1](#).

While the calculation of the nucleation rate coefficient J always follows Koop et al. [36], the calculation of a_w can be selected in the initialization file. The current default implementation combines results from Carslaw, Luo, and Peter [12] and Tabazadeh et al. [81]. Other options are available and described in the documentation.

Heterogeneous freezing separates in two major implementations:

The first heterogeneous freezing implementation describes immersion freezing according to a paper by Kärcher and Lohmann [35]. The framework is based on the concept of *shifted water activity* describing heterogeneous freezing events similar to homogeneous freezing, leading to sharp heterogeneous ice onsets. Therefore only the ASP particle type is accounted for freezing.

Parameterizations from early AIDA studies are implemented representing e.g. soot, coated soot, ammonium sulfate, mineral dust, volcanic ash [47]. It's also possible to pass a numeric value as critical relative humidity w.r.t. ice RH_{ice}^{crit} , which describes a temperature-independent freezing threshold. This freezing implementation was used in several publications [11, 18, 38].

However, a steep freezing onset doesn't match observations and the current knowledge about heterogeneous ice nucleation. Therefore a more realistic heterogeneous freezing mechanism was implemented.

The second heterogeneous freezing implementation describes deposition nucleation by solid INPs and is based on the concept of INAS density n_s parameterizations (see [section 2.2.2](#)).

For each model time step the ice crystal number concentration is calculated as

$$n_{\text{ice}}(T, S_{\text{ice}}) = \sum_{j=1}^k n_{\text{ae}}^j [1 - \exp(-A_{\text{ae}}^j \cdot n_s(T, S_{\text{ice}}))] \quad (4.1)$$

temperature T , saturation ratio with respect to ice S_{ice} , surface area of a single aerosol particle A_{ae}^j in the size bin j and INAS density n_s . With T and S_{ice} being functions of time n_s and therefore also n_{ice} are time dependent, too. The aerosol surface area A_{ae}^j is calculated under the assumption of spherical aerosol particles from their radius r^j and a defined density ρ .

Using equation (4.1) the model checks at each time step t if the calculated total amount of heterogeneous ice crystals n_{ice} exceeds the number of previously nucleated INPs. If this is the case for a time step t_i , the difference

$$\Delta n_{\text{ice}}^{\text{het}}(t_i) = n_{\text{ice}}(t_i) - n_{\text{ice}}^{\text{max}} \stackrel{!}{>} 0 \quad (4.2)$$

is the amount of freshly formed ice crystals. The nucleated INPs get removed from their respective size bin and added to a size bin in the ice crystal PSD. So in case of $\Delta n_{\text{ice}}^{\text{het}}(t_i) > 0$, $n_{\text{ice}}(t_i)$ becomes the new value for $n_{\text{ice}}^{\text{max}}$ to be used subsequently. With this method the INP PSD gets depopulated continuously, which leads to a much more realistic ice-nucleation behavior compared to the method following Kärcher and Lohmann [35].

The old (first) heterogeneous freezing implementation has a tight mass bin coupling between the ASP and ice crystal PSD. Since a freezing droplet already provides a certain amount of mass to a freshly formed ice crystal the ASP size bins could be simply mapped to ice crystal size bins. However, with the new implementation a nucleated solid INP forms an ice crystal which starts with a negligible amount of ice mass, so it doesn't match the predefined ice crystal PSD bin array. This is a code legacy problem, since such a bin mapping made sense with the old implementation, but is very limited to this approach. As a workaround the ice crystals formed from deposition freezing start to populate an additional empty bin with the geometric mean diameter of the initial INP size distribution. Once this size bin grows bigger than a certain threshold the next empty bin is used to take up the freshly nucleated heterogeneous ice crystals. The implemented INAS density parameterizations are listed in the documentation as possible initialization variables. They include the parameterizations by Steinke et al. [78], Ullrich et al. [85] and the parameterization derived within this work.

4.1.4 Trace gas balancing

The model has support for a number of condensable trace gases being present in the UTLS. The implemented gases are nitric acid (HNO_3), hydrogen bromide (HBr), hydrogen chloride (HCl) and most importantly water vapor (H_2O). Those trace gases interact

with solution droplets through condensation and evaporation. The model implementation follows Dahneke [14] and is compared to other approaches in the textbook of Seinfeld and Pandis [73, section 12.1]. Water vapor is also balanced with respect to ice (deposition/sublimation) using the same procedure, but with the respective ice-related selection of input arguments.

The driver of mass flux for a component x between its gas phase and a solid or liquid phase is the gradient between the partial pressure p_x in the gas and the respective saturation vapor pressure $p_{x,0}$ over the surface of the particle.

The parameterization for the saturation vapor pressure of water with respect to ice $p_{w,0}^{\text{ice}}$ can be defined in the initialization file through a specified keyword argument. Also for the water vapor saturation pressure over liquid multiple parameterizations are available.

For the calculation of $p_{w,0}$ over liquid surfaces the Kelvin effect is also taken into account [82]. The calculation involves density and surface tension of the particle, which is, for ASPs with H_2SO_4 and HNO_3 , based on measurements from Martin, George, and Mirabel (2000) [50].

HNO_3 from the gas phase can not only be solved in the liquid phase, but can also be trapped in ice crystals while they grow ("HNO₃ trapping") [27]. This process is implemented according to Kärcher and Voigt (2006) [30] and was already described in earlier publications regarding MAID [11, 18].

4.1.5 Diabatic effects

Latent heat effects are tracked for each model time step and added to the gas temperature. This works for internal and external trajectories similarly, with minor deviations in the implementation logic. If needed, it is also possible to force an external temperature trajectory, which can be desired if the temperature profile derives from an experiment where such diabatic contributions are already tracked.

The latent heat contributions derive from condensation on and evaporation of ASPs, growth and sublimation of ice crystals, freezing of ASPs and INPs as well as HNO₃ trapping.

4.1.6 Sedimentation

Sedimentation is described based on publications by Spichtinger and Gierens (2009) [76] and Spichtinger and Cziezo (2010) [77, section 2.2]. Ice mass and number-weighted terminal velocities after Heymsfield and Iaquinta [21] are used to simulate the sedimentation

of ice crystals [38]. The sedimentation is only applied to ice crystals and neglected for ASPs and INPs due to their small masses.

Considering a vertical extent of the simulated cloud a flux of sedimenting ice crystals through the box model can be assumed. If the model represents a volume at cloud top there is no flux of particles from above, whereas the vertical flux into the volume is maximized at the cloud bottom. Therefore one can define a sedimentation factor representing the ratio between an incoming ice crystal flux from above and an outgoing flux at the bottom of the simulated volume. So the factor is 0 at the cloud top and 1 at the cloud bottom. The sedimentation factor is used as a weight to calculate the net sedimentation loss of ice crystals.

4.1.7 Gravity wave driven fluctuations

Gravity waves induce fluctuations on the vertical velocity of an air parcel and force also temperature fluctuations, as discussed in section 2.1.1. An implementation based on Kärcher and Podglajen [29] can be activated. An important measure in the calculations is the Brunt-Väisälä frequency N (equation (2.3)). N is used to derive an autocorrelation time, which serves as a characteristic timescale τ_c after which new contributions from the fluctuation probability density function are added to the model dynamics. However, adiabatic updrafts represent the edge case in which N becomes zero and τ_c can not be derived. To work around this caveat one can specify a custom autocorrelation time in the initialization file. Therefore it is also possible to add gravity wave fluctuations for internally calculated trajectories, which follow an adiabatic updraft. For external trajectories following a stable temperature profile N and τ_c are calculated internally.

During a model run the fluctuations are randomly selected from a pool of values sampled from the respective probability density functions. For reproducible results a custom seed can be specified to fix the state of the model-intrinsic (pseudo-)random number generator. Otherwise the seed is randomly chosen on runtime.

4.2 Model history

This section gives a brief overview about the origin of MAID and gives a brief overview about publications using the model.

The MAID model has its roots in a model by Bunz and Dlugi [10] from 1991. This model focused on chamber experiments and the code was further developed by Helmut Bunz at Forschungszentrum Karlsruhe (predecessor of the later KIT). The step towards a UTLS

model was made with a publication by Bunz et al. [11] in 2008. It was developed along the PhD work of Iulia Gensch at Forschungszentrum Jülich (FZJ) and was used in an accompanying publication [18]. The model received routines regarding condensation and freezing of UT aerosol particles, microphysics and partitioning of water and nitric acid in ice clouds, adaption to Lagrangian atmospheric cirrus cloud calculations, heterogeneous freezing of liquid aerosol particles and nitric acid uptake of growing ice crystals ('trapping'). In the same year the model was used in a publication by Wagner et al. [88] to simulate the growth of H₂SO₄ solution particles. In 2012 Rolf et al. [63] published a paper using MAID with a new implementation of sedimentation for ice crystals. In 2016 Krämer et al. [38] published an extensive comparison of MAID runs, which was the last work with the model.

4.2.1 Model development within this work

This work started with the model in a state as it was after the publication by Krämer et al. However, some features, which supposedly existed, are lost and couldn't be recovered due to a lack of documentation. Those lost features include chamber wall fluxes, separated atmospheric mode and chamber mode, aerosol coagulation and a graphical user interface.

The source code has been modernized from FORTRAN77 to the free form modern Fortran standard. Features up to the Fortran2018 standard are in use now. Starting from a single file, the code is now structured in separate module files, grouping the procedures according to their physical meaning. Various code blocks were moved into procedures.

A documentation of the source code was added directly into the source files. This includes docstrings for modules and procedures as well as descriptions for the variables at declaration. Literature references were added where ever possible.

Broken functionalities were fixed, such as pre-existing ice or a mode, which allows to force the liquid aerosol particles to be in equilibrium with their environment.

The fundamental code to read water wall flux contributions from an external file was implemented by Christian Rolf from FZJ before the model was handed over. Within the present work the calculation of the wall flux was derived to actually use this feature (see section 3.5).

A new way to simulate heterogeneous freezing was implemented. Therefore solid aerosol particles were implemented as a whole new particle type. While the previous heterogeneous freezing mechanism did only represent immersion freezing, the new freezing mechanism is based on INAS density parameterizations and describes deposition freezing (see section 2.2.2).

The model used to derive its trajectory from an external file. Now it is also possible to run internally calculated adiabatic updraft scenarios based on defined start conditions and an updraft velocities. The end of the internally calculated trajectory must be either defined by final conditions or based on a given model runtime.

In case of internal trajectories the possibility for gravity wave based updraft fluctuations was implemented according to Kärcher and Podglajen [29] (see [section 2.1.1](#)).

Besides the direct source code of [MAID](#) a small ecosystem of additional tools was developed. The model should be run using a bash script, which handles the compilation of the source code and manages the generation of temporary directories to realize multiple parallelized runs. The script provides a command line interface with several useful options. Other tools were developed using python. Their functionalities cover the generation of initialization files aiming on scalability for batch runs. In case of external trajectories, the trajectory files can be generated from a single function call. To simulate experiments from the [AIDA](#) cloud chamber functions are available to generate both, initialization and trajectory files, directly from [AIDA](#) files (if generated from `aida_experiment_analysis`, see [section 3.4.1](#)).

The whole development was tracked with git and put into a public repository [71]. With consultation and permission of the previous authors the model could be published under the open software license [AGPL v3](#).

4.3 Model limitations

As a parcel model [MAID](#) does not represent some features, which would be desirable for [CCT](#) scenarios. The model does not have a vertical resolution. Therefore it is not possible to make predictions about cloud thickness, fall streaks or vertically stacked layers. The lack of vertical resolution includes that we can't resolve the water cycle and can't predict feeding mechanisms for warmer clouds at lower altitude. Internal fluctuations in the parcel due to latent heat aren't represented as well. The resolution is not only limited in the vertical direction, but also horizontally. Thus spacial movements driven by shear winds are also not represented.

A major drawback when modeling [CCT](#) is the missing information about radiative forcing. Since the radiative forcing depends in the vertical extent of the cloud, this issue is related to the missing vertical resolution.

Chapter 5

Results and Discussion

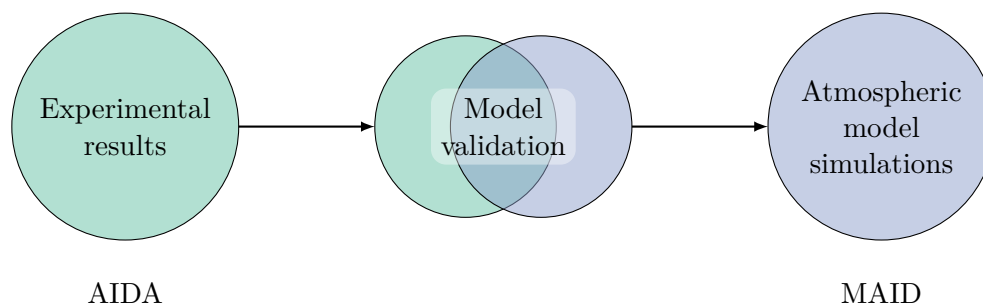


Figure 5.0.1 Schematic of the logical structure in the results chapter.

This chapter starts with the experimental results, which are used to validate the MAID simulations and finishes with atmospheric model results, as depicted in Figure 5.0.1.

Section 5.1 starts with the characterization of bulk aerosol samples, that are used as heterogeneous INPs in the cloud chamber experiments. Section 5.2 continues with the ice-nucleating properties of the aerosols under cirrus conditions and the competition between homogeneous and heterogeneous freezing. Section 5.3 discusses the model validation results. The experimental scenarios are reproduced with the model and the results are compared. The section also includes the derivation of parameterizations to represent the chamber wall flux in the model. Moreover the implementation of gravity wave driven updraft fluctuations in MAID is compared against literature results. Finally, section 5.4 presents model results of atmospheric cirrus seeding scenarios.

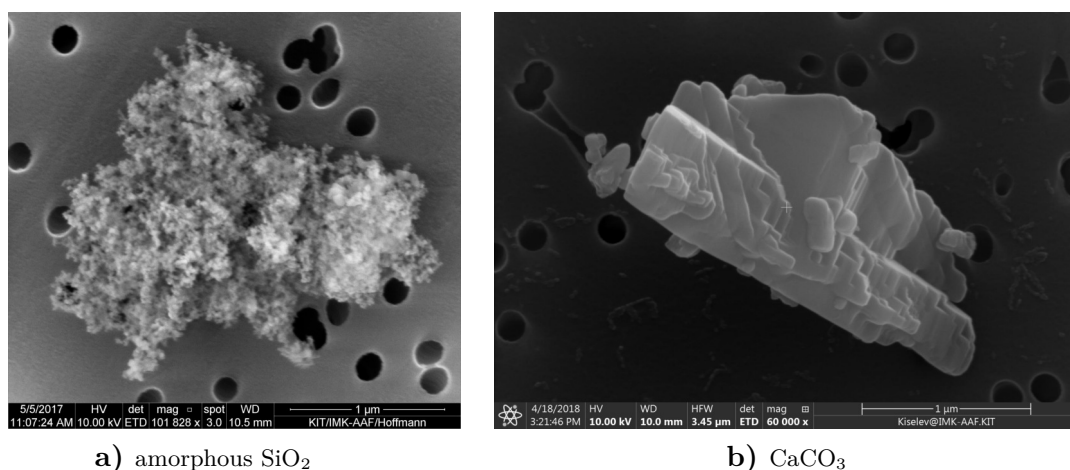


Figure 5.1.1 Environmental scanning electron microscopy pictures of aerosol particles sampled from AIDA on Whatman Nuclepore filters with 0.2 μm pore size.

5.1 Aerosol characterization

5.1.1 Filter sampling and ESEM images

Fumed silica and calcium carbonate aerosols were sampled from AIDA on Whatman Nuclepore filters with 0.2 μm pore size. Subsequently they were analyzed with an ESEM. Figure 5.1.1 shows ESEM images for fumed silica and calcium carbonate, respectively. The images provide an impression of the aerosol particle morphology.

Two CaCO₃ aerosol samples were collected on filters and compared with respect to a heat treatment of the respective bulk aerosol sample (filters not presented here). One filter was sampled from the normal CaCO₃ sample and the other filter was sampled from a dried sample, which was in an oven for one week at 60 °C. However, the ESEM images did not show any systematic difference with respect to the aerosol morphology.

5.1.2 Size distribution analysis

Lognormal fits were applied to the measurements from APS and SMPS to parameterize the size distributions of the dispersed aerosols in AIDA. The analysis is limited to only those PSD measurements with enough aerosol ($>10 \text{ cm}^{-3}$) and without any issues encountered during aerosol dispersion.

The three subplots in Figure 5.1.2 show different approaches to fit the PSDs of fumed silica, quartz and calcium carbonate with lognormal functions.

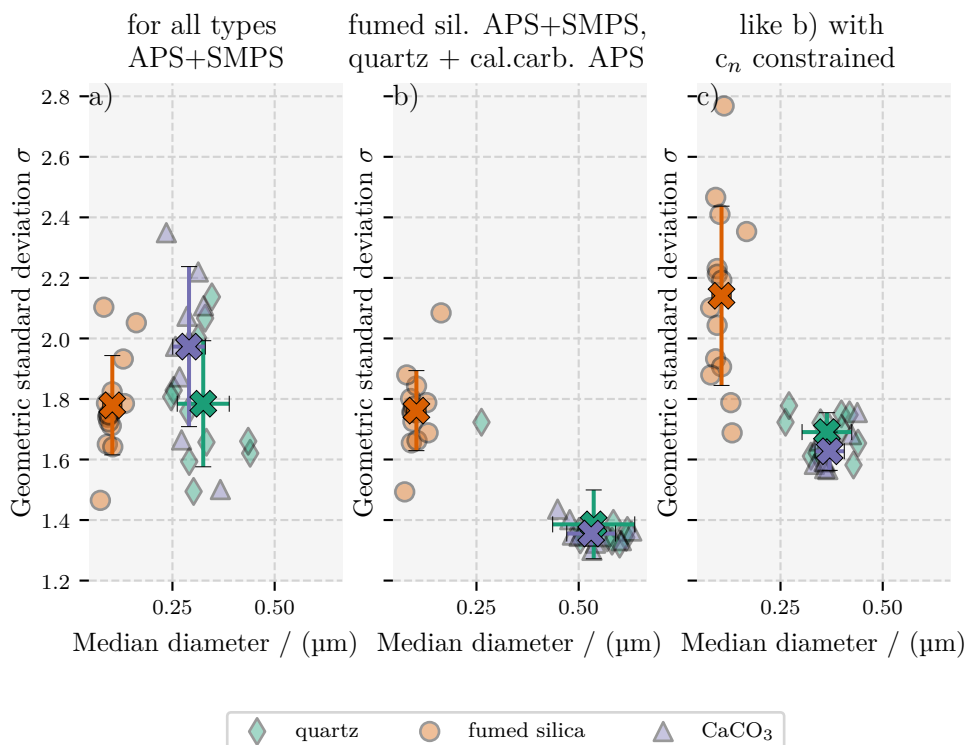


Figure 5.1.2 Aggregated lognormal fit parameters median diameter and geometric standard deviation for different fit methods. Subplot **a)** shows the fit parameters derived from fitting the **APS** and **SMPS** PSD measurements with the **IDL**-based framework. Subplot **b)** shows fit parameters derived with the python-based framework while using only **SMPS** for fumed silica and only **APS** for quartz and CaCO_3 . These data points complement the fitted number concentrations shown in [Figure 3.4.2b](#). Subplot **c)** is similar to **b)**, but here the fit was constrained to the number concentration from the **CPC**.

Subplot **a)** shows the lognormal fit parameters derived from the **IDL** routines. As discussed in [section 3.4.2](#), the fits derived with the **IDL** framework have a tendency to not capture the shape of the size distribution well. This is might be caused by artifacts in the **SMPS** data at relatively low number concentrations (see [section 3.2.8](#)). Hence, a significant variability for σ is observed.

The fits in subplot **b)** were conducted using the `psd_analysis` framework. In subplot **b)** for quartz and calcium carbonate the fits were only applied on the **APS** dataset to map the shape of the slope towards bigger particles better. This results in a significant reduction of the variability of σ and shifts the fitted median diameter towards larger values. However, as shown in [section 3.4.2](#), using only one instrument can lead to an underestimation of the fitted total number concentration, especially for the **APS** data. Fumed silica was further fitted to both instruments, since the **SMPS** is more dominant for this aerosol type.

The fit parameters in subplot c) are derived similar as in subplot b), but with a constrain to the CPC number concentration. As expected, for quartz and calcium carbonate the fitted median diameter decreases and the geometric standard deviation increases. These lognormal fits match the slope of the APS measurements well. For fumed silica the constrain towards the CPC number concentration leads to a strong increase for the variability of σ . An explanation could be an insufficient representation of the number concentration by the SMPS, which makes a constrain to the CPC concentration inconsistent with the measured size distribution.

For further analyses the averaged lognormal fit parameters for quartz and calcium carbonate are used from Figure 5.1.2 subplot c). For following analyses with fumed silica the averaged parameters from Figure 5.1.2 subplot b) are used, by assuming that the SMPS measures the shape of the distribution correctly.

Depending on the methods and assumptions a significant variability for the derived lognormal fit parameters could be demonstrated. This highlights, that the instrumentation (and presumably especially the SMPS), has systematic uncertainties, which are currently not characterized or quantified and require further investigation.

5.2 Ice nucleation in AIDA expansion experiments

This section is separated in three subsections. First section 5.2.1 covers homogeneous freezing of sulfuric acid ASPs. Afterwards section 5.2.2 focuses on heterogeneous freezing of the seeding aerosol particles. The derived INAS density parameterizations are presented there. Finally, section 5.2.3 covers the competition between both freezing mechanisms.

5.2.1 Homogeneous ice nucleation

This section covers homogeneous freezing of ASPs in the AIDA experiments at cirrus temperatures.

Figure 5.2.1 shows the observed homogeneous freezing onsets $S_{\text{ice}}^{\text{crit}}$ in our experiments. Two campaigns AWICIT02 and AWICIT03 are excluded due to a different method of ASP generation. The freezing onsets generally agree well with a review of ASP experiments in AIDA by Schneider et al. [68].

The freezing line according to Koop et al. [36] is represented in Figure 5.2.1 through a parameterization given by Kärcher and Lohmann [35], which includes assumptions regarding the size and H_2SO_4 mass fraction of the particles. However, the freezing threshold varies only insignificantly for typical variations of those parameters.

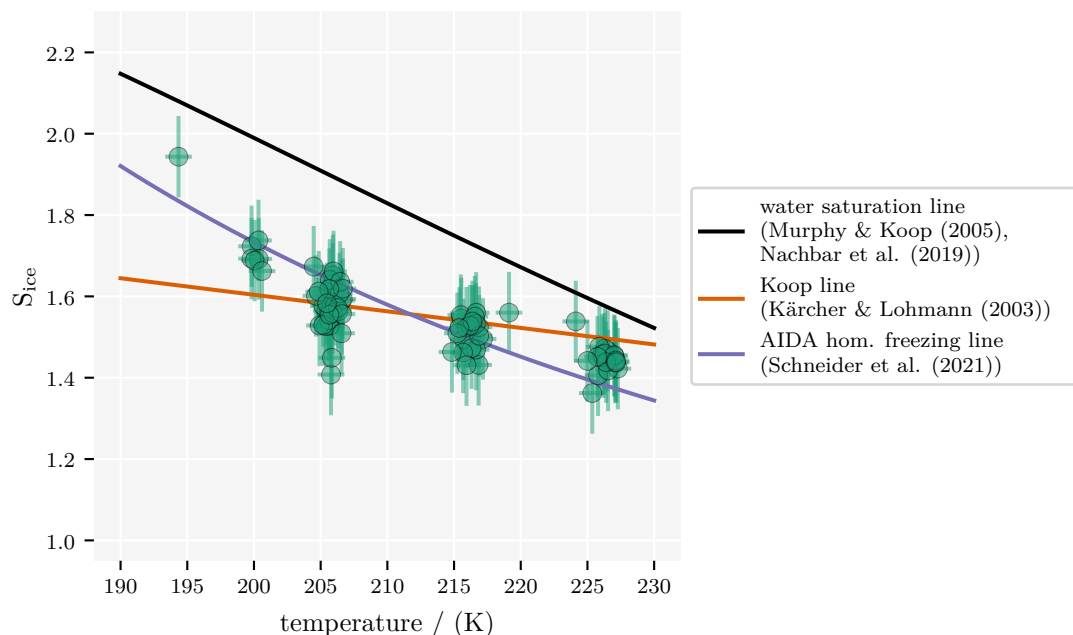


Figure 5.2.1 Homogeneous freezing onsets of ASPs as observed in the AIDA experiments. Each data point refers to an expansion experiment. The 'Koop line' describes homogeneous freezing according to Koop et al. [36] through a parameterization given by Kärcher and Lohmann [35]. The 'AIDA hom. freezing line' is derived from a fit through an extensive dataset of homogeneous freezing experiments conducted at AIDA [68].

Observed onsets deviate from the freezing parameterization by Koop et al. [36] towards lower temperatures, particularly for temperatures below 210 K. Schneider et al. [68] confirm this trend with additional data points towards temperatures <200 K. Their corresponding fit line is shown in Figure 5.2.1. The current hypothesis is that the water vapor saturation pressure of supercooled liquid water increases more steeply with decreasing temperature, than represented in current parameterizations.

Towards warmer temperatures between 220 K and 230 K lower freezing thresholds $S_{\text{ice}}^{\text{crit}}$ are observed, which can be explained from temperature inhomogeneities inside the chamber. This could lead to local fluctuations of S_{ice} which trigger homogeneous ice formation before it is expected regarding the mean gas temperature. These fluctuations lead to an asymmetric shift, since only fluctuations towards colder temperatures affect the ice formation onsets, whereas fluctuations towards warmer temperatures don't cause any observable effect. The magnitude and frequency of such fluctuations are unknown.

5.2.2 Heterogeneous ice nucleation

Heterogeneous freezing observed in [AIDA](#) experiments is described by fitted [INAS](#) densities. The calculation requires information about the ice crystal number concentration n_{ice} at given ambient conditions and the surface area distribution of the initial aerosol population (see [section 2.2.2](#)).

The aerosol surface area is derived from the size distribution fits of [APS](#) and [SMPS](#) measurements. The aerosol particles are assumed to have a spherical shape. Here, the n_{ice} is only derived from the *welas2* [OPC](#) sensor. In comparison, the [OPC](#) sensor *welas1* could detect more ice crystals in the smaller size range, however the data is less reliable. Therefore the derived [INAS](#) densities might be underestimated for experiments at low temperatures, where the ice crystals stay at comparably small sizes.

For the uncertainty of the [INAS](#) density n_s the error approximation of Ullrich et al. [85] is applied. They derived a combined relative error of 40 % for n_s .

[Figure 5.2.2](#) shows the [INAS](#) densities for all three seeding aerosol types. The fitted function including the fit parameters is shown as well. Since the [INAS](#) densities n_s of all three aerosols don't show a temperature dependence in the investigated temperature interval, a temperature independent fit function of the form

$$\log(n_s) = a + S_{\text{ice}} \cdot b \quad (5.1)$$

is used. For experiments where also homogeneous freezing occurred, the trajectories were cut off before the onset of homogeneous freezing to treat only the heterogeneously formed ice.

The temperature dependence of n_s isolines as proposed by Ullrich et al. [85, Fig. 5] could not be observed. The fitted [INAS](#) densities of quartz and calcium carbonate align both between $1 \times 10^{10} \text{ m}^{-2}$ and $1 \times 10^{12} \text{ m}^{-2}$ for S_{ice} at about 1.4, which compares well to the deposition freezing parameterization for dust by Ullrich et al. [85].

5.2.3 Cirrus thinning effect in cloud chamber experiments

To probe the [CCT](#) seeding effectiveness, the competition between heterogeneous and homogeneous freezing was investigated through [AIDA](#) expansion experiments. The [INP](#) seeding concentrations n_{INP} are varied, while [ASP](#) background concentrations are held constant at around 50 cm^{-3} .

The main goal of the presented cloud chamber experiments is to quantify the suppression of homogeneous ice formation due to heterogeneously formed ice. The maximum total

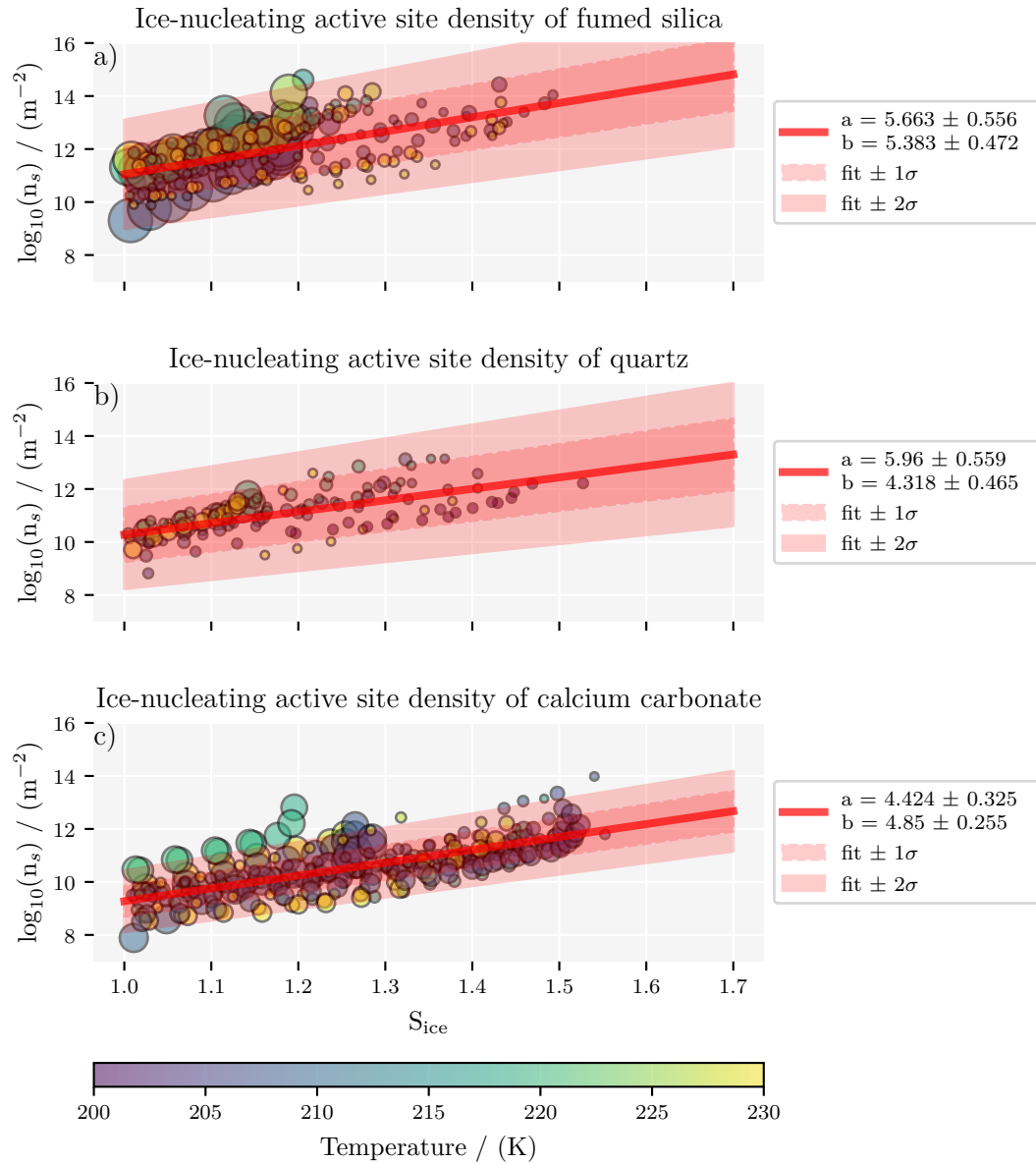


Figure 5.2.2 Ice-nucleating active site densities n_s derived from AIDA experiments for a) fumed silica, b) quartz and c) calcium carbonate. The data points are fitted by a linear fit function $\log_{10}(n_s) = a + b \cdot S_{ice}$ with parameters specified in the legend. The size of the data points indicates the total aerosol number concentration n_{ae} of the respective experiment.

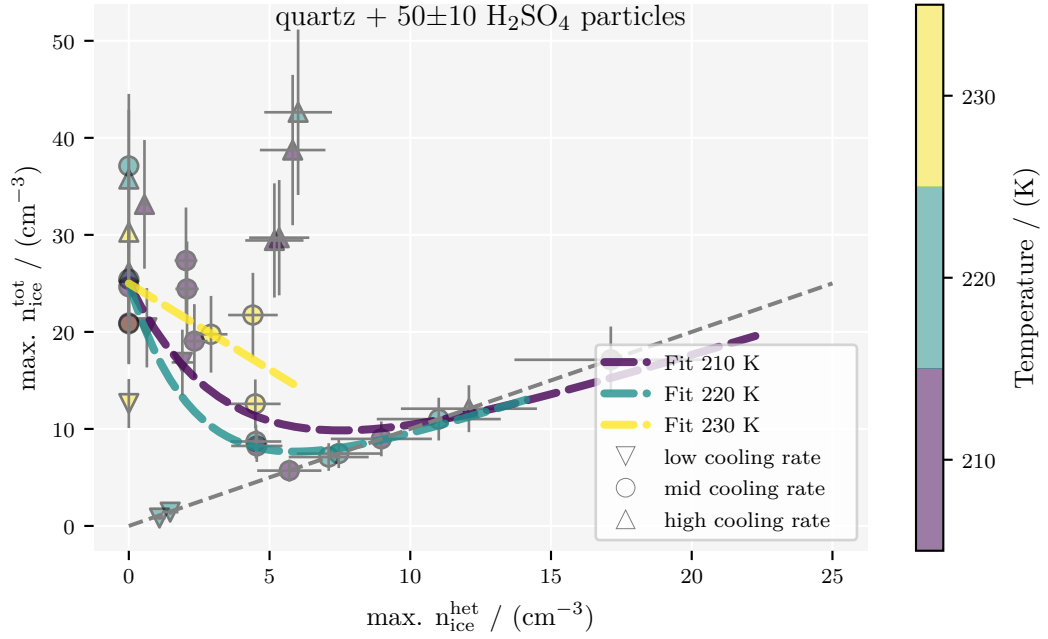


Figure 5.2.3 Cirrus cloud thinning in *AIDA* using quartz as seeding aerosol. The three cooling rate regimes correspond to different power levels of *AIDA* pump 2 (see text). The fit function is empirically derived and acts only as a guidance for the eye. The fits refers to the main data subset with 80 % pump power. Smaller data subsets with slower/faster cooling rates are indicated with triangles.

ice crystal number concentration $n_{\text{ice}}^{\text{max}}$ of each experiment is interpreted as a proxy for the density of the formed cloud. Hence, a minimum in $n_{\text{ice}}^{\text{max}}$ marks optimal CCT.

Figure 5.2.3 and Figure 5.2.4 show the total ice crystal number concentration $n_{\text{ice}}^{\text{tot}}$ as a function of the heterogeneous ice crystal number concentration $n_{\text{ice}}^{\text{het}}$ for each INP type. The figures include data points of different cooling rates, whereas the 'mid' cooling rate (\circ) corresponds to the standard pump power of 80 % of pump 2 (P2). Most expansion experiments were conducted at this pump rate. The slow cooling cooling rate (∇) corresponds to pump powers of 60 % to 70 % and the high cooling rate (\triangle) to a pump power of 100 %. These experiments are used to test the sensitivity of homogeneous freezing for slower/faster changes in S_{ice} . As to be expected, the homogeneous ice crystal number concentration increases with faster pump rates and decreases with slower pump rates. The color code refers to the starting temperature of the expansion experiments, which were conducted at three main temperatures, 210 K, 220 K and 230 K.

The dataset for quartz, shown in Figure 5.2.3, contains the most expansion experiments and will therefore be primarily discussed. An empirical fit is added in Figure 5.2.3 to guide the eye regarding the trend of the data points. The fit function represents the freezing competition through the assumption that the homogeneous ice crystal number concentration drops exponentially with a linearly increasing heterogeneous ice crystal

number concentration. The empirical expression

$$n_{\text{ice}}^{\text{tot}} = \left[n_{\text{ice},0}^{\text{hom}} \cdot \exp\left(-a \cdot n_{\text{ice}}^{\text{het}}\right) \right] + b \cdot n_{\text{ice}}^{\text{het}} \quad (5.2)$$

is used as a first order approximation with $n_{\text{ice},0}^{\text{hom}}$ being the ice crystal number concentration observed without any heterogeneously formed ice and two free fit parameters a and b . An individual fit is applied on three different experimental subsets with experiments being in the range ± 3 K around 210 K, 220 K and 230 K, respectively. However, the number of data points for each fit curve is too low to be considered robust, hence the fit should only be used as a visual guidance and should not be treated as a parameterization of the freezing competition.

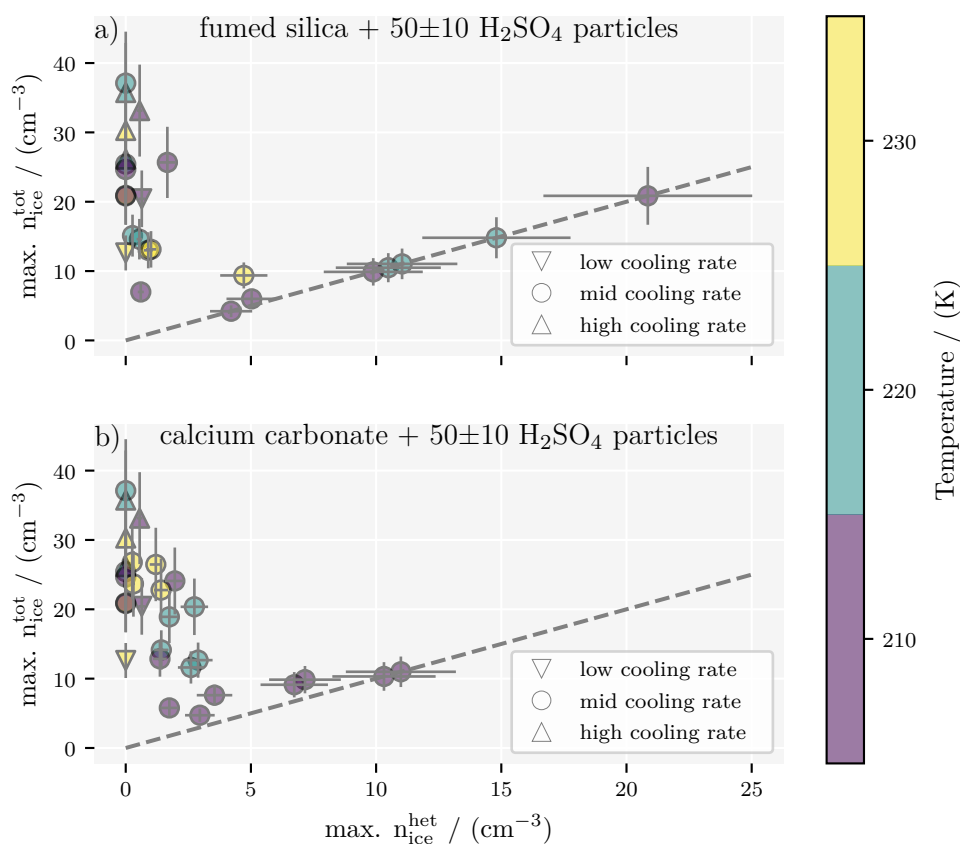


Figure 5.2.4 Cirrus cloud thinning in AIDA for fumed silica and calcium carbonate as seeding aerosol.

Figure 5.2.4 shows similar data as in Figure 5.2.3, but for fumed silica (subplot a)) and calcium carbonate (subplot b)). Since $n_{\text{ice}}^{\text{tot}}$ drops very fast for increasing $n_{\text{ice}}^{\text{het}}$ the optimum seeding concentration lies in a region which is experimentally difficult to investigate. Low INP number concentrations of $< 5 \text{ cm}^{-3}$ are difficult to achieve and the OPC reaches its detection limit. Nevertheless, a window of optimal seeding can be derived for each aerosol type at almost each starting temperatures.

An exception is observed for calcium carbonate seeding at a starting temperature of 230 K. At this temperature the ability to form ice heterogeneously dropped rapidly in the presence of H_2SO_4 . This effect was not observed for the starting temperatures ≤ 220 K. H_2SO_4 reacts with calcium carbonate and seems to change the surface properties and thus the freezing abilities of CaCO_3 aerosol at higher temperatures. The origin of the temperature dependence remains to be investigated. This inconsistent behavior leads to the conclusion that calcium carbonate is probably not suited as a proper seeding aerosol for CCT.

In a next step, the previously described results are used to validate microphysical model simulations with respect to the freezing competition during cirrus formation. Note that the ASP number concentration of 50 cm^{-3} was chosen to be lower than UTLS background aerosol concentrations. The choice for this number concentration was made in a very early stage of this work and was subsequently kept for comparability within the dataset.

5.3 MAID validation

Simulations with MAID are used to reproduce the thermodynamics and freezing competition as seen in the AIDA expansion experiments.

Section 5.3.1 provides wall flux parameterizations for the AIDA experiments, which are used within the model to represent cloud chamber boundary conditions. In section 5.3.2 key variables observed in the AIDA expansion experiments are compared against model runs. In section 5.3.3 the model representation for the experimentally observed freezing competition (see section 5.2.3) is shown. In section 5.3.4 implementation of gravity wave based updraft fluctuations is validated against results from literature.

5.3.1 Cloud chamber wall flux parameterization

In the following the wall flux parameterizations are presented for the fluid dynamic approach and the approach according to Cotton et al. [13]. An explanation about the meaning of the fit factors and the selection of the dataset is given in the methods section 3.5.

The scatter data in Figure 5.3.1 and Figure 5.3.2 show the fit parameters derived from the individual reference expansion experiments, as described in the methods section 3.5. Outliers are marked according to their z-score, which tells how many standard deviations a data point is allowed to deviate from the mean value. The outliers were excluded from the linear parameterization fit.

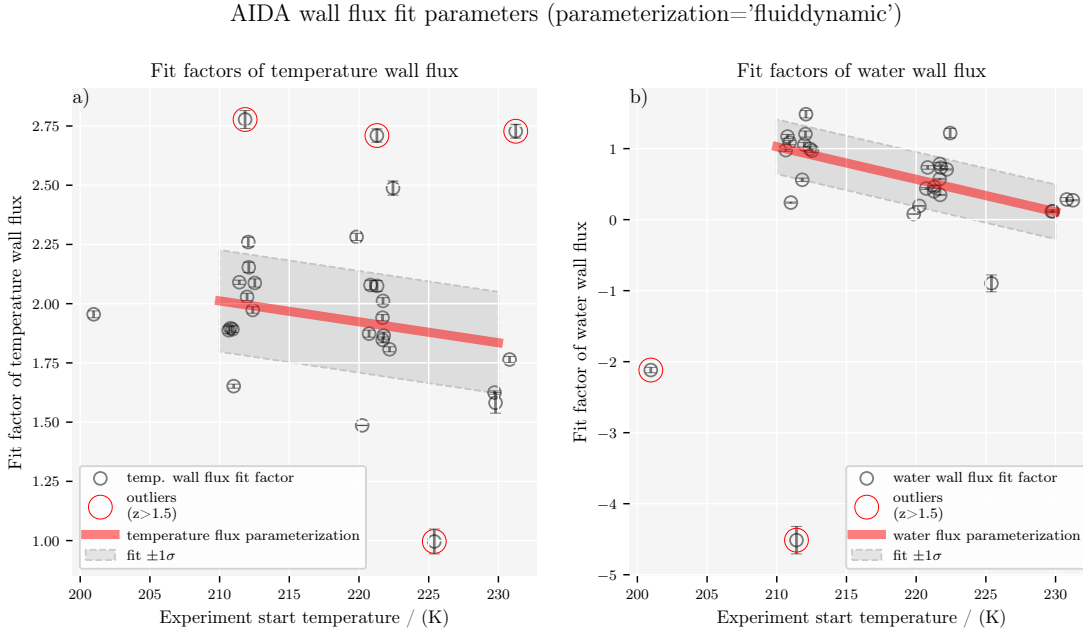


Figure 5.3.1 Fit of wall flux parameterizations according to the fluid dynamic approach (see appendix B). Each scatter point refers to a reference expansion experiment in AIDA. The campaign AWICIT01B is excluded since the mixing fan showed technical issues.

The fit was applied on the reduced dataset in the interval from 210 K to 230 K, where the majority of experiments were conducted. The derived parameterization should not be used for experiments outside this temperature range and not for experiments which were not prepared as described in section 3.2.10. A different preparation procedure could result in a different ice coverage in the inner chamber, thus requiring a different parameterization.

The parameterizations are fitted with a linear function following

$$x_{\text{fit}}(T) = A \cdot T + B. \quad (5.3)$$

The resulting parameters (A, B) are given in Table 5.3.1 for the two wall flux approaches, respectively.

Both parameterizations of the water wall flux are close to zero at 230 K, which indicates that the icing of the chamber walls doesn't play a role at higher temperatures. For the fluid dynamic approach this factor, which represents the actual fraction of iced walls, reaches 1 for about 210 K. Thus our experiments are conducted in the range where the icing of the wall changes from 0 % to 100 %.

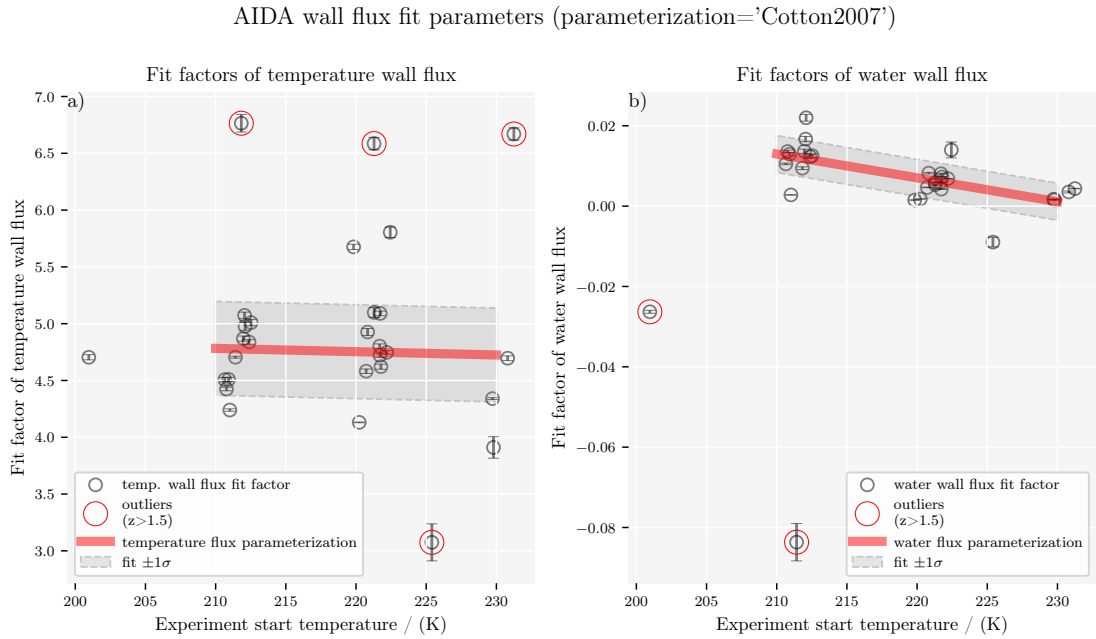


Figure 5.3.2 Fit of wall flux parameterizations according to Cotton et al. [13]. Each scatter point refers to a reference expansion experiment in AIDA. The campaign AWICIT01B is excluded since the mixing fan showed technical issues.

5.3.2 Model validation against AIDA experiments

In this section the model is used to conduct simulations of the AIDA experiments. The experiments and their corresponding model runs are compared using aggregated comparison metrics.

Our comparison focuses on the ice crystal number concentration n_{ice} and the temporal development of the saturation ratio S_{ice} . Quantitative metrics about the deviation between model and experiment are shown in Figure 5.3.3 for n_{ice} . The derived metrics are explained in appendix A.1.

The heterogeneous freezing is represented through the INAS density parameterizations presented in section 5.2.2. The size distributions are initialized from measurements as derived in section 5.1.2. The temperature and pressure profiles are directly used from the measured AIDA data and written into trajectory files used by the model. Hereby, the effect of the heat wall flux is already included in the experimental temperature profile. The water wall flux is calculated based on the parameterizations presented in section 5.3.1 and is also passed into the model as a time resolved column in the trajectory file.

The results in Figure 5.3.3 are based on model runs using the fluid dynamic wall flux implementation, but similar comparison plots for the other wall flux implementations are

Table 5.3.1 Fit parameters for to parameterize the AIDA water and heat wall flux. The parameters A and B refer to the temperature T dependent function given in equation (5.3).

wall flux method	quantity	slope A	offset B	σ
fluid dynamic	heat	-8.831×10^{-3}	3.866	0.215
	water	-4.611×10^{-2}	10.71	0.383
Cotton et al. (2007)	heat	-2.898×10^{-3}	5.391	0.413
	water	-5.933×10^{-4}	0.138	0.004

included in appendix C. At this point, can be stated that the fluid dynamic approach and the approach following Cotton et al. [13] lead to comparably good results.

From Figure 5.3.3 can be concluded that the model shows a systematic overestimation of n_{ice} in all metrics. This derives primarily from homogeneous freezing, which is less pronounced in the experiment regarding the number concentration and freezing onsets. However, the fractional bias also shows a smaller mode at largely negative values. This mode derives from experiments where the homogeneous freezing occurred in the experiment, but has not been triggered in the model. Such constellation occurs especially for temperatures ≤ 210 K, as being discussed below in more detail.

Regarding the deviations of the saturation ratio S_{ice} a more detailed analysis is necessary before drawing conclusions. A similar figure, such as Figure 5.3.3, for S_{ice} is given in appendix C. Such a comparison shows significant deviations between MAID results and the AIDA data. On the one hand, this is true if the whole experimental period is taken into account, which typically includes a relaxation period after the peak humidity was reached and the pumps are being stopped. However, an expansion experiment includes different periods, which can have very different characteristics and are not equally important. A quantitative analysis differentiating specific trajectory intervals has not been conducted within this work and can be a future follow-up task.

Instead, the observed characteristics will be discussed with help of a selection of expansion experiments. Figure 5.3.4 shows two AIDA experiments, which were simulated using the MAID model.

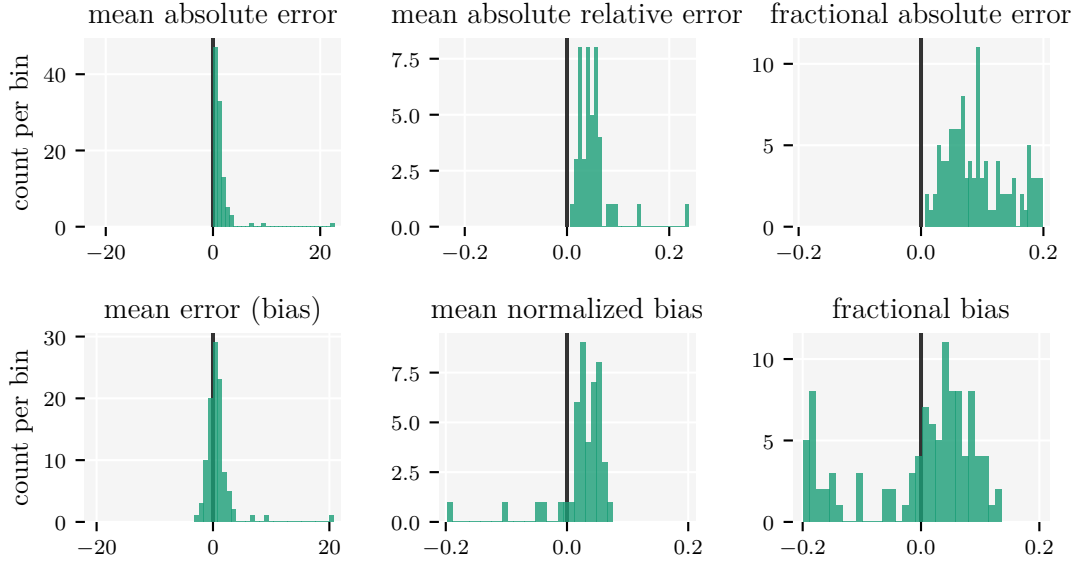
(MAID vs AIDA) metrics for n_{ice} , wall flux 'fluiddynamic'

Figure 5.3.3 Aggregated evaluation metrics about the deviation of the total ice crystal number concentration n_{ice} between **MAID** results and **AIDA** experiments. The abscissas in the first column have the unit cm^{-3} , whereas all other abscissas are dimensionless. For the bias metrics (bottom row) ($\text{MAID} - \text{AIDA}$) is calculated, so a positive bias indicates larger values in the model. The mean absolute relative error (MARE) and mean normalized bias (MNB) in the central column are normalized with respect to the **MAID** data. The experimental dataset excludes experiments from the campaigns **AWICIT02** and **AWICIT03** due to a different method of **ASP** generation.

The trajectory of an **AIDA** expansion can be subdivided into three main segments. The first segment goes from the start until peak humidity, the second segment from peak humidity until the pumps stop and the third section after the pumps have stopped. The first two sections are most relevant for the formation and the growth of ice, whereas in the third segment the gas simply equilibrates according to the temperature gradient to the wall.

In the first segment the model reproduces S_{ice} equally well for most experiments, independent of the wall flux implementation. However, in some cases (**Figure 5.3.4a**) the wall flux implementation is able to make a significant difference for the ice crystal number concentration of homogeneously formed ice, even though the peak humidity differs only on a small scale. In the second time segment the wall flux implementations 'fluiddynamic' and 'Cotton2007' lead to an increase of the water vapor, which is not observed in the experiment. Such behavior is representative for a majority of the model runs. For both implementations can be derived that the wall flux seems to be overestimated for high temperature gradients between gas and wall.

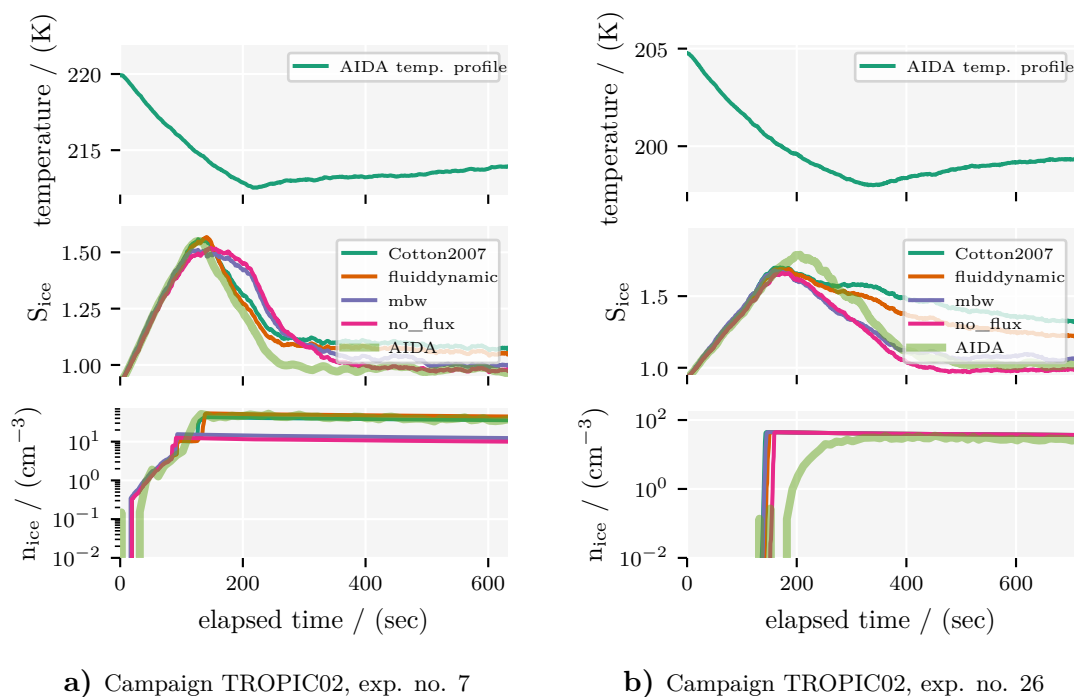


Figure 5.3.4 Comparison of selected **AIDA** expansion experiments against **MAID** simulations with different wall flux implementations. The legend in the center panel indicates the wall flux implementation used in the model (as described in section 3.5). The model run without any water wall flux implementation is labeled as 'no_flux'.

The agreement between **MAID** and **AIDA** with regard to the critical saturation ratio for the homogeneous freezing onset varies with temperature. For 230 K the model shows homogeneous freezing onsets even at slightly higher S_{ice} than observed in the experiment, whereas the agreement is very good around starting temperatures of 220 K. With starting temperatures at 210 K and below an increasing disagreement evolves (see Figure 5.3.4b). At very low temperatures the critical saturation ratio in the experiment exceeds the threshold in the model significantly. This effect has been described and discussed in a paper by Schneider et al. [68]. The current hypothesis is that water vapor saturation pressure of supercooled water might be higher in this temperature region, than predicted by the parameterization of Murphy and Koop [55].

The ice number concentration originated from homogeneous freezing modes is generally higher in the model. This could be explained through temperature inhomogeneities in the chamber, which cause only a fraction of the chamber volume reaching the homogeneous freezing threshold at once.

Even with the discussed caveats, the agreement between model and experiments is generally good with respect to the thermodynamics and the heterogeneous ice formation.

5.3.3 Ability of MAID to simulate CCT

Here MAID is utilized to reproduce the experimentally observed cirrus seeding effect, as described in section 5.2.3. The model is initialized to match the experimental conditions of the experimental dataset shown and in Figure 5.2.3. Heterogeneous freezing is described by the INAS density parameterization for quartz. An adiabatic updraft with an updraft velocity of 300 cm s^{-1} is selected to match the pump rate of 80% P2. The ASP number concentration is set to 50 cm^{-3} and sets of model runs are created for three different starting temperatures, 210 K, 220 K and 230 K. INP number concentrations were varied between 0 cm^{-3} to 40 cm^{-3} for each starting temperature.

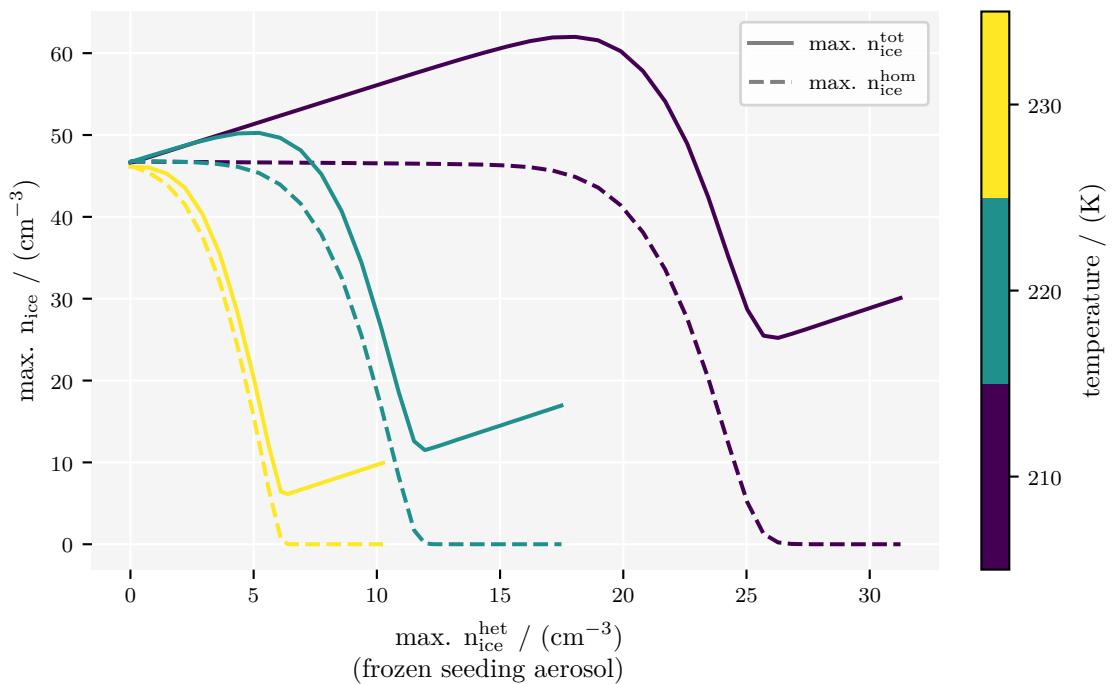


Figure 5.3.5 Simulation of the AIDA seeding effect using MAID. The plot shows quartz seeding for three different starting temperatures. The model was initialized to reproduce the features shown in Figure 5.2.3. Details about the model initialization are provided in the text.

The model output is shown in Figure 5.3.5. It shows the maximum total ice crystal number concentration $n_{\text{ice}}^{\text{tot}}$ and the maximum homogeneously formed ice crystal number concentration $n_{\text{ice}}^{\text{hom}}$ as a function of the heterogeneous ice crystal number concentration $n_{\text{ice}}^{\text{het}}$. The most striking feature is that $n_{\text{ice}}^{\text{tot}}$ doesn't drop in the presence of heterogeneously formed ice, as observed in the experiment. Instead, $n_{\text{ice}}^{\text{tot}}$ first increases with increasing $n_{\text{ice}}^{\text{het}}$ before the freezing competition has enough impact to alter the homogeneous ice formation. However, this could only be observed for the colder temperatures. It can be deduced that for low cirrus temperatures the depletion of water vapor by ice crystal

growth, happens slower in the model than observed in our experiments. For the curve with a starting temperature at 230 K the minimum in $n_{\text{ice}}^{\text{tot}}$ matches the observation comparably well.

A second important difference between the experimentally observed seeding effect shown in Figure 5.2.3 and the model simulation in Figure 5.3.5 is the different level of $n_{\text{ice}}^{\text{hom}}$. As also mentioned in section 5.3.2, the higher homogeneous ice crystal number concentration is a feature that is consistent through the comparison between model and AIDA observation.

5.3.4 Gravity wave forcing effect on homogeneous freezing

As a new feature, MAID includes the application of randomized updraft velocity fluctuations based on a stochastic representation of mesoscale gravity waves, based on the description of Kärcher and Podglajen [29]. In this section MAID model runs are compared to a result shown in Kärcher, Jensen, and Lohmann [28, Fig. 1].

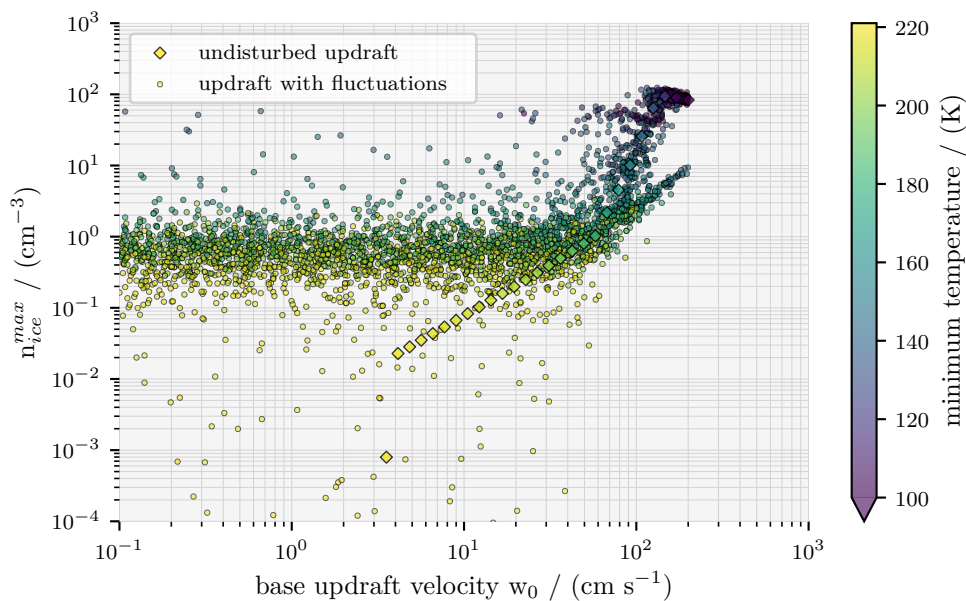


Figure 5.3.6 Effect of updraft velocity with fluctuations on homogeneous ice number concentration.

To reproduce the result from Kärcher, Jensen, and Lohmann [28] the model is initialized as described in their publication. The starting conditions are set to be 221 K and 300 hPa with a saturation ratio of $S_{\text{ice}} = 1.3$. Only sulfuric acid ASPs are initialized, so no heterogeneous ice formation is included. The ASP population has a number concentration

of 500 cm^{-3} a median radius¹ of 32 nm and a lognormal geometric standard deviation of $\sigma = 1.5$. The gravity wave forcing is initialized with $\sigma_w = \sqrt{2} \cdot 10 \text{ cm s}^{-1} \approx 14.14 \text{ cm s}^{-1}$ and a fixed autocorrelation time of $\tau_c = \frac{1}{N} = 2.8 \text{ min}$. For the calculation of the Coriolis frequency a latitude angle of 60°N is selected. 5000 individual model runs are lognormally distributed over base updraft velocities ranging from 0.1 cm s^{-1} to 200 cm s^{-1} , while their updraft fluctuation is randomly sampled from a Laplacian probability distribution. The duration of each model run is limited to 2 h. An additional termination condition is added by Kärcher, Jensen, and Lohmann [28] to stop the trajectory after a homogeneous freezing event, while they argue a second homogeneous freezing event would not happen within the given time scale of two hours. However, here this termination condition is intentionally not implemented, since a second homogeneous freezing mode could be observed in some cases.

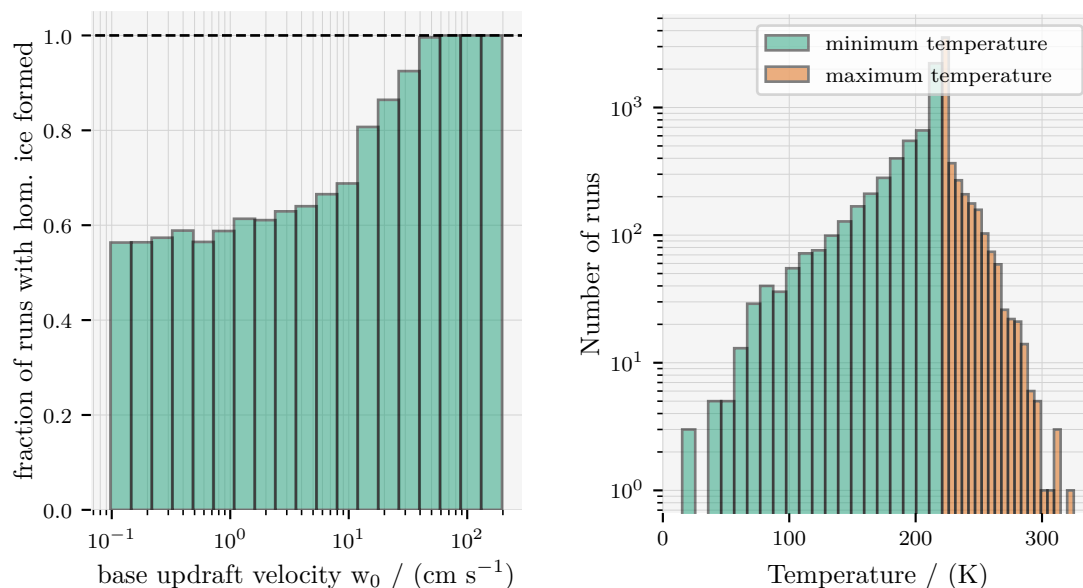
Figure 5.3.6 shows the maximum reached total ice crystal number concentration $n_{\text{ice}}^{\text{max}}$ from our model runs as a function of the base updraft velocity w . Our results reproduce the literature reference well. For updrafts $< 10 \text{ cm s}^{-1}$ a smaller spread of $n_{\text{ice}}^{\text{max}}$ is observed in our simulations, but the magnitude matches generally very well. For updrafts $> 50 \text{ cm s}^{-1}$ a kink emerges towards increasing $n_{\text{ice}}^{\text{max}}$, which indicates a second mode of homogeneous freezing. This feature is not represented in [28], since their additional breakup condition aborts before such an event. The highest $n_{\text{ice}}^{\text{max}}$ are reached for unrealistic low temperatures, which is circumvented in the literature reference by the breakup criteria after the first homogeneous mode. The impact of temperature extremes is shown in Figure 5.3.7b.

When comparing the runs with updraft fluctuations to the reference runs with unperturbed updrafts the most striking feature is the huge amount of homogeneously formed ice at low updrafts, where the set of reference experiments doesn't show any ice at all. It can be concluded for base updraft velocities $w < 10 \text{ cm s}^{-1}$ that the scenarios with unperturbed updrafts underestimate the amount of homogeneously formed ice significantly.

In Figure 5.3.7 statistics of the 5000 model runs from Figure 5.3.6 are shown. Figure 5.3.7a shows the fraction of model runs per base updraft bin, which reached the homogeneous freezing threshold. Even for the smallest updrafts homogeneous freezing is observed in $> 50\%$ of the ensemble. This is an important finding with a strong impact on the prediction of atmospheric ice crystal number concentrations at slow base updraft velocities. .

Figure 5.3.7b shows the temperature extremes in our model runs. It shows that the gravity wave fluctuations have a certain probability to change the observed air parcel temperature to extreme values. However, note that the scale is logarithmic and the vast

¹Kärcher, Jensen, and Lohmann [28] uses a median dry radius of 20 nm, however MAID must be initialized with the particles being in equilibrium with the ambient conditions.



a) Fraction of model runs including homogeneous ice formation.

b) Histogram of temperature extremes.

Figure 5.3.7 Statistics on the set of model runs with updraft perturbation shown in Figure 5.3.6. Plot a) shows the fraction of model runs in which homogeneous freezing occurs. Plot b) shows the distribution of temperature extremes (min, max) for all model runs.

majority of the model runs stays close enough to the expected temperature range. The distribution of temperature extremes has a bias towards decreasing temperatures, due to the adiabatic cooling of the base updraft velocities. The possibility of single model runs to escape into unrealistic temperature regimes seems to be an intrinsic problem of the updraft fluctuation implementation.

As a general conclusion about the comparison to the results of Kärcher, Jensen, and Lohmann [28], there is good agreement. However, the comparison leaves room for further investigations in the future. It is yet not clear why a smaller spread for $n_{\text{ice}}^{\text{max}}$ is observed in MAID for slow base updraft velocities. Furthermore the fact, that model runs can escape from reliable temperature regions puts a question mark to the underlying assumptions of this approach. Adding a damping term or a specified lifetime for single updraft fluctuation contributions could probably solve this issue.

5.4 MAID: atmospheric scenarios

After validating the model and learning about its constraints, the model application can be extended towards atmospheric simulations. Therefore scenarios including slower updraft velocities and lower seeding concentrations are simulated. These two parameters were the main limitation for atmospherically relevant scenarios in the AIDA experiments. For the atmospheric scenario sets the main parameter variation is chosen to be with respect to the updraft velocity w and the seeding number concentration n_{INP} .

Section 5.4.1 focuses on atmospheric scenario sets following adiabatic updrafts starting from saturated conditions at either 210, 220 or 230 K.

Section 5.4.1 presents the scenario set at 230 K with activated gravity wave fluctuations. For each individual scenario a batch of runs is simulated, which internally differs only by random stochastic updraft fluctuations.

5.4.1 Scenarios with constant updraft velocities

The effect of CCT was simulated using MAID with sets of scenarios along adiabatic updraft trajectories with static updraft velocities. The updraft velocity w and the heterogeneous INP number concentration n_{inp} were varied over a broad range. In addition the starting temperature was varied between 210 K, 220 K and 230 K and the starting pressure between 400 hPa and 500 hPa. The saturation ratio was set to $S_{\text{ice}}=1$ at trajectory start. The sulfuric acid ASP PSD was initialized with a median diameter of 64 nm, a geometric standard deviation of $\sigma = 1.5$ and a total number concentration of 1000 cm^{-3} . The H_2SO_4 mass fraction was set in a way that the ASPs are in equilibrium with the ambient conditions. The heterogeneous INP PSD was initialized with a median diameter of $0.6 \mu\text{m}$, a geometric standard deviation of $\sigma = 1.2$, while the number concentration was varied between zero and $1 \times 10^6 \text{ l}^{-1}$. The heterogeneous ice formation follows the parameterization for quartz, as derived in section 5.2.2.

Each scenario ended as soon as either a final pressure of 200 hPa or a final temperature of 190 K was reached. Those values are typical for the Arctic tropopause height and the lower range of cirrus cloud top temperatures, respectively.

Figure 5.4.1 shows the maximum total ice number concentration $n_{\text{ice}}^{\text{max}}$ of model runs with a starting pressure of 500 hPa. The plots a) to c) show the scenario sets for the different starting temperatures 210 K, 220 K and 230 K. In the center of each plot an area of reduced $n_{\text{ice}}^{\text{max}}$ is prominent which represents successful cirrus cloud thinning. These regions correspond to the seeding effect which could be observed experimentally in section 5.2.2. The values of $n_{\text{ice}}^{\text{max}}$ are higher for lower temperatures, but the general

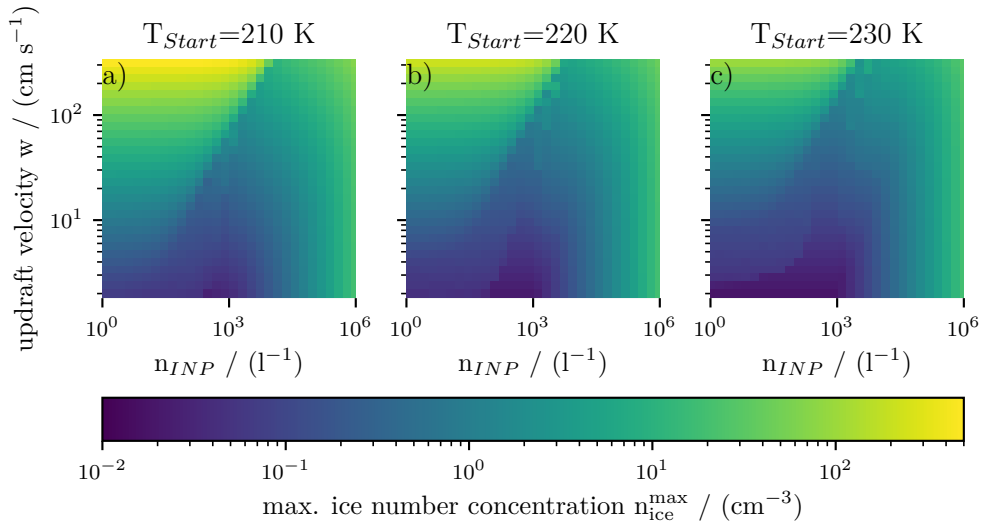


Figure 5.4.1 The maximum ice crystal number concentration $n_{\text{ice}}^{\text{max}}$ of MAID runs at three different starting temperatures for various constant updraft velocities w and seeding number concentrations n_{INP} . a) – c) represent datasets for the temperatures 210 K, 220 K and 230 K.

observed pattern with the optimum seeding region varies only slightly for different starting temperatures.

To quantify the seeding effect the scenarios with $n_{\text{INP}} > 0$ (seeding) must be compared to the corresponding scenario with $n_{\text{INP}} = 0$, which is the baseline scenario without seeding. In the scenarios with $n_{\text{INP}} = 0$ all ice forms homogeneously from the ASP population. Figure 5.4.2 shows the maximum ice crystal number concentration $n_{\text{ice}}^{\text{max}}$ and the maximum ice water content IWC_{max} for those baseline scenarios as a function of updraft velocity w . Note that $n_{\text{ice}}^{\text{max}}$ decreases with increasing temperature, whereas IWC_{max} shows an increase. The magnitude of $n_{\text{ice}}^{\text{max}}$ shows an accelerating increase with increasing updraft velocity w . In contrast, magnitude of IWC_{max} grows slower with increasing w . These different trends can be explained when looking into the dynamics for fast updrafts. For fast updrafts an increasing amount of ASP freezes, but the population of unfrozen ASP is still large, so the nucleation is not yet limited by a lack of particles. However all the ice crystals have only a limited amount of water vapor available to grow with. Therefore IWC_{max} is limited by the availability of water vapor.

For a closer comparison of the impact of different starting pressures Figure 5.4.3 shows a comparison of $n_{\text{ice}}^{\text{max}}$ for two scenario sets at $T_{\text{start}}=220$ K (dataset from plot b) in Figure 5.4.1). The comparison shows a slight shift of the observed pattern, which causes the biggest deviation at the transition of two regimes. The regimes are regions in the parameter space where the freezing characteristics are dominated through different mechanisms. Subplot c) shows that the absolute number concentration for scenarios $n_{\text{INP}}^{\text{max}} < 1 \times 10^3 \text{ l}^{-1}$ varies about a factor of 2, but the underlying pattern stays very

only homogeneously formed ice ($n_{\text{INP}}=0$)

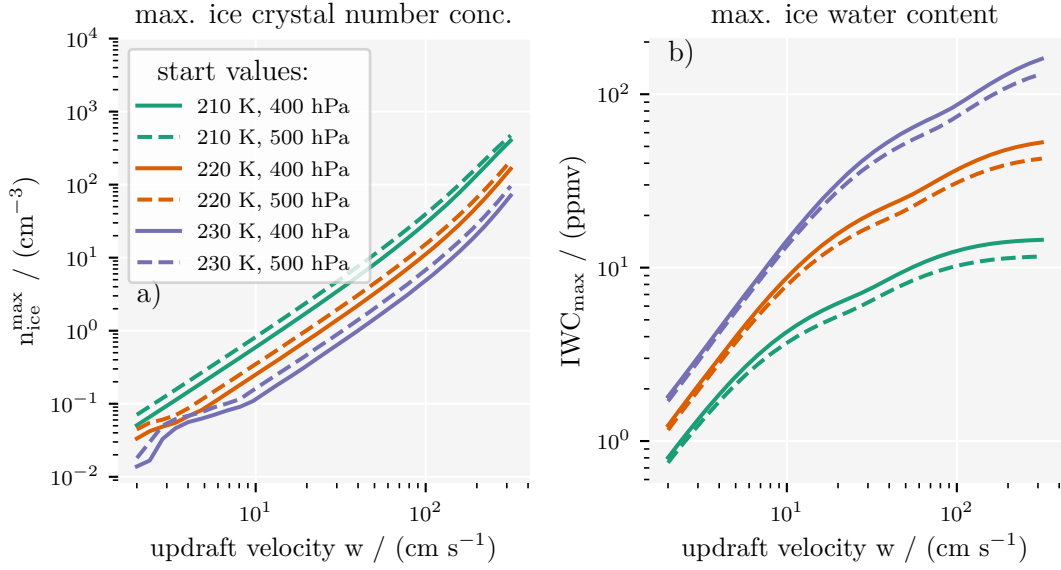


Figure 5.4.2 Maximum ice crystal number concentration and maximum ice water content for pure homogeneous scenarios as a function of static updraft velocity.

similar. Overall, it can be stated that different starting pressures have a rather small effect on $n_{\text{ice}}^{\text{max}}$. This applies also to IWC_{max} , which is not explicitly shown here.

The origin of those regimes is easier to interpret when looking on the maximum ice saturation ratio as depicted in Figure 5.4.4. The plots a) to c) show the maximum saturation ratio with respect to ice $S_{\text{ice}}^{\text{max}}$ as a function of updraft velocity w and INP number concentration n_{INP} . In plot b) the four regimes are labeled from I to IV, which is representative for a) and c), too. Regime I derives from scenarios with a single homogeneous freezing mode and only one major peak in S_{ice} . The boundary between regime I and II indicates that S_{ice} shows a subsequent increase along its trajectory and exceeds the first peak. In regime II such a recovery of S_{ice} with a subsequent higher peak can happen multiple times and can lead to multiple homogeneous freezing events. The boundary between the regimes II and III describe the region where heterogeneous freezing starts to suppress the homogeneous freezing. This boundary can be considered a marker for optimal cirrus thinning. The transition between the regimes III and IV is similar to the boundary between the regimes I and II. In regime III the heterogeneously formed ice is not enough to prevent a second peak in S_{ice} , which starts a second heterogeneous nucleation period. In contrast, the heterogeneous ice formation in regime IV is so dominant, that it prevents S_{ice} to reach another peak along the trajectory.

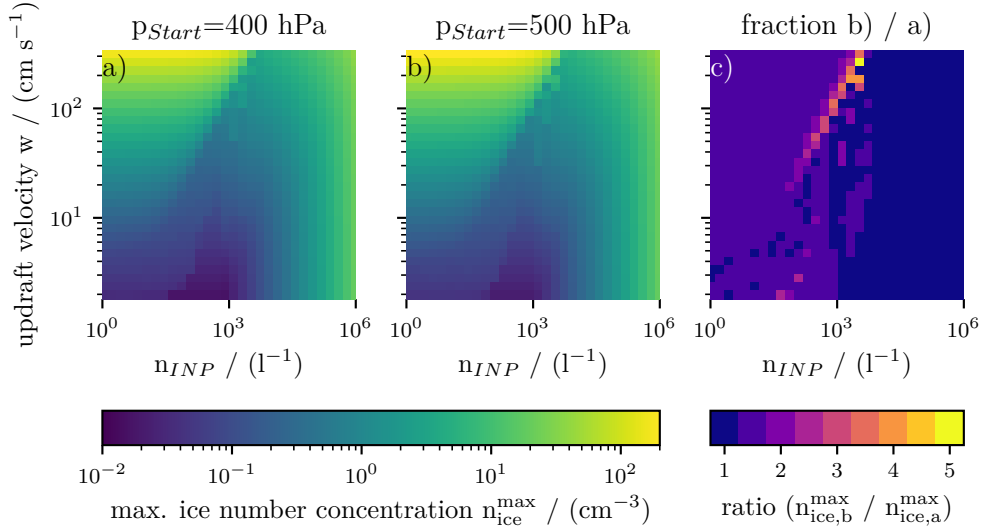


Figure 5.4.3 Comparison of maximum ice crystal number concentrations for scenario sets with different starting pressures. The maximum ice crystal number concentration $n_{\text{ice}}^{\text{max}}$ for atmospheric updraft scenarios with constant updraft velocity for starting pressures at a) 400 hPa and b) 500 hPa. Both scenario sets have a starting temperature of 220 K. Subplot c) shows the ratio of the data plotted in b) and a).

To quantify the seeding effect the seeding scenarios with $n_{\text{INP}} > 0$ must be compared to the corresponding baseline scenario with $n_{\text{INP}} = 0$. Therefore $n_{\text{ice}}^{\text{max}}$ and IWC_{max} is discussed for scenarios at $n_{\text{INP}} = 0$. Figure 5.4.5 shows the relative deviation of $n_{\text{ice}}^{\text{max}}$ as the ratio $n_{\text{ice}}^{\text{max}} / n_{\text{ice}}^{\text{max}}|_{n_{\text{INP}}=0}$. For a deviation of $\pm 5\%$ the color coding is set to white, to explicitly depict the scenarios with only minor changes. Three regimes are marked in plot b), being also representative for plot a) and c). Regime I represents scenarios where the INP number concentration has only a negligible effect on $n_{\text{ice}}^{\text{max}}$. In other words: in this regime homogeneous freezing is nearly unaffected by the seeding aerosol. This regime is more pronounced for fast updrafts, since the timescale for the heterogeneous ice to deplete water vapor before homogeneous freezing happens is rather short. For lower temperatures the ice growth kinetics are slower, so regime I is more pronounced than at warmer temperatures. Regime II shows that the *relative* seeding effect is stronger for faster updrafts. Since faster updrafts cause more homogeneously formed ice crystals a suppression of the homogeneous mode has a stronger relative impact. A line of scattered, white colored model runs represents the boundary between regime II and III. This boundary marks the very important transition from the regime with reduced $n_{\text{ice}}^{\text{max}}$ (II) to the regime with enhanced $n_{\text{ice}}^{\text{max}}$ (III). Regime III represents the undesired overseeding in a CCT scenario.

Previously it was shown that $n_{\text{ice}}^{\text{max}}$ and IWC_{max} don't follow the same trend with increasing updraft velocities. While $n_{\text{ice}}^{\text{max}}$ can continue to increase without a noticeable limitation, the IWC_{max} is limited by the depletion of water vapor pressure. So it is important to also discuss IWC_{max} as a measure for the cirrus cloud thickness.

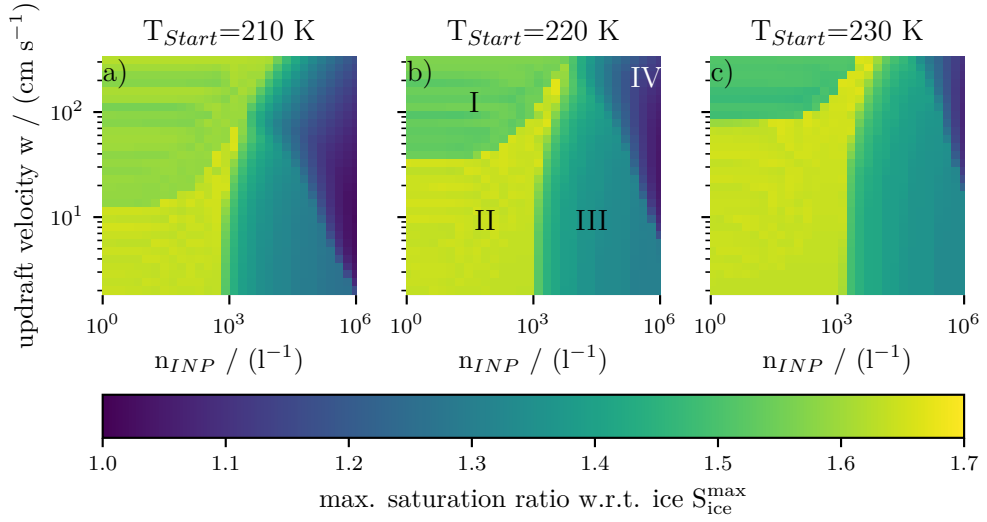


Figure 5.4.4 Maximum ice saturation ratio for MAID scenarios with static updrafts. Four regimes can be distinguished and are indicated in plot b). The regimes are explained in the text.

Therefore Figure 5.4.6 shows the evaluation of the maximum IWC as a function of seeding concentration n_{inp} and updraft velocity w . Figure 5.4.6a shows, in contrast to the similar plot for $n_{\text{ice}}^{\text{max}}$, higher values for warmer temperatures, which is caused by the higher water vapor content at warmer temperatures. Yet, for both variables the highest magnitudes are derived within the strongest updrafts and also the general pattern of regimes is the same identical.

Figure 5.4.6b shows the relative deviation of IWC_{max} to the baseline scenario, which has no seeding. In contrast to the same visualization regarding $n_{\text{ice}}^{\text{max}}$, the strongest relative reduction of IWC_{max} is observed for slower updrafts. Here the water vapor is mainly depleted by heterogeneously formed ice crystals. At slow updrafts they have enough time to sediment out, so they are not simultaneously present in the system to increase IWC_{max} . So the minimum region doesn't necessarily mean that the absolute water vapor depleted from ice crystals is especially low. It rather states that the cloud thickness was below a certain threshold IWC_{max} along the whole trajectory.

5.4.2 Scenarios with updraft velocity variations

In this section the effect of gravity wave driven updraft fluctuations on CCT effectiveness is presented. The analysis is limited on a subset of scenarios with a starting temperature of 230 K and a starting pressure of 500 hPa.

For the calculation of the updraft fluctuations the gravity wave autocorrelation time is set to a static value of $\tau_c = 200$ s. The value of τ_c is about 17% longer than used by

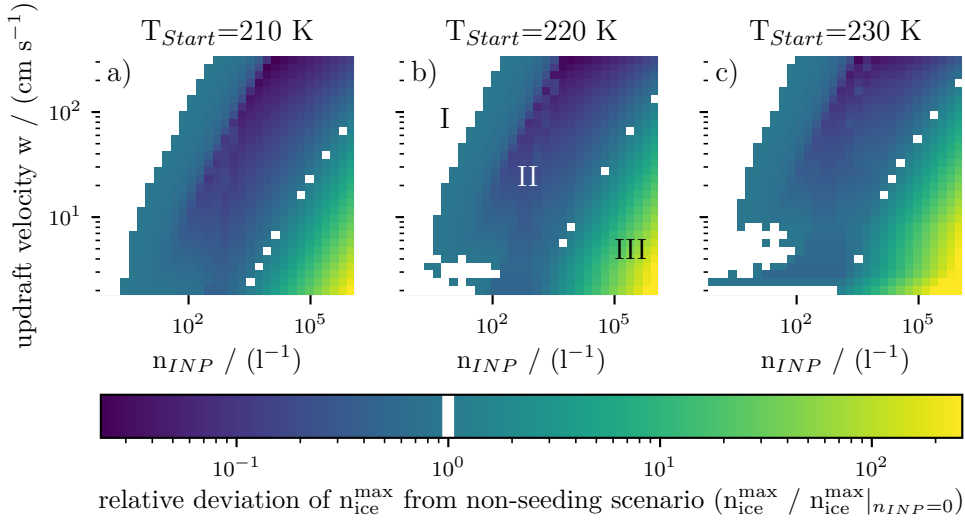


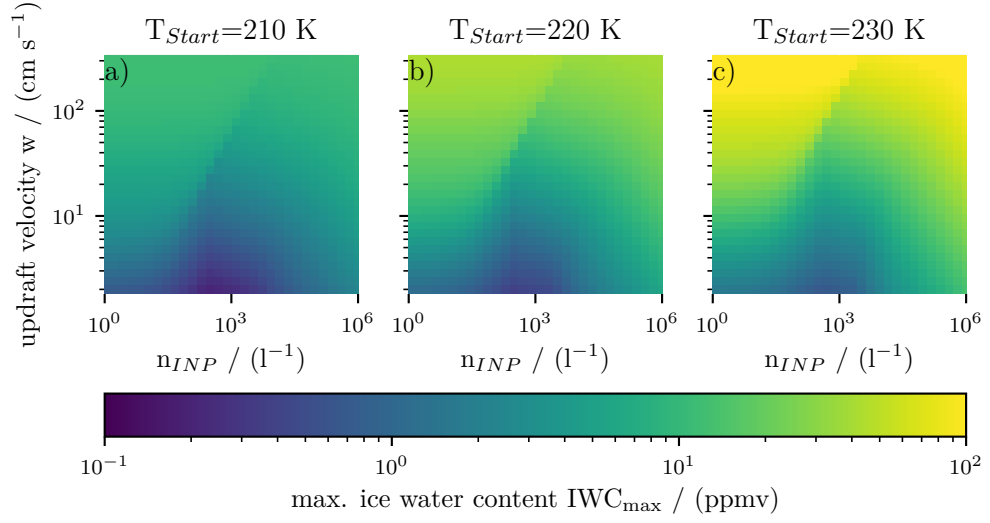
Figure 5.4.5 Relative deviation of maximum ice crystal number concentration $n_{\text{ice}}^{\text{max}}$ from the non-seeding scenario at $n_{\text{INP}} = 0$. The plots a)-c) show sets of model runs at different starting temperatures. The relative deviation around $\pm 5\%$ is colored white to highlight areas with low variation. Regimes are highlighted in plot b). I: negligible seeding effect; II: effective seeding; III: overseeding. With respect to $n_{\text{ice}}^{\text{max}}$ the white dots forming a line between the areas II and III mark the transition from successful seeding to overseeding.

Kärcher et al. [31]. The width parameter of the fluctuations is set to $\sigma_w = 15 \text{ cm s}^{-1}$, as a generally typical value. The latitude angle is set to 75°N , representing a not closer specified location within the Arctic circle. All other parameters were selected as specified for the clean updraft scenarios in section 5.4.1. Since in this case the statically defined updraft velocity w is not constant, it is now called the base updraft velocity w_0 . For each individual scenario 50 runs were conducted with different seeds for the random number generator.

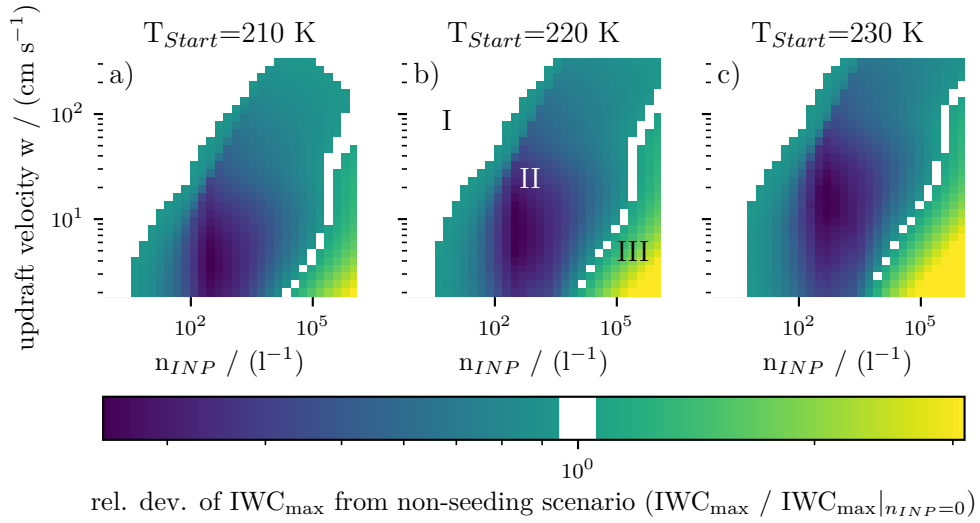
Figure 5.4.7 shows the output of those simulations with updraft perturbation. The subplots a) and b) show the median of the 50 runs per scenario for the maximum ice crystal number concentration $n_{\text{ice}}^{\text{max}}$ and the maximum ice water content IWC_{max} . The minima, which indicate optimal seeding, are less pronounced in subplots a) and b) and shifted towards higher n_{ice} .

The subplots c) and d) of Figure 5.4.7 show the deviation from the unperturbed scenario set shown in subplot c) of Figure 5.4.1.

Generally, an increase in $n_{\text{ice}}^{\text{max}}$ and IWC_{max} can be observed, which is associated with the presence of updraft fluctuations. This finding is consistent with updraft fluctuations causing homogeneous freezing already at base updraft velocities where homogeneous freezing wouldn't be observed otherwise. There is, however, a large degree of variability between runs that is not visible through the averaged metric.



a) Maximum ice water content IWC_{\max} for model ensemble runs at 210 K, 220 K and 230 K.



b) Relative deviation of the maximum ice water content IWC_{\max} from the non-seeding scenario with $n_{\text{INP}} = 0$ for model ensemble runs at 210 K, 220 K and 230 K. The relative deviation around $\pm 5\%$ is colored white to highlight areas with low variation.

Figure 5.4.6 Analysis of the maximum IWC for model run ensembles at starting temperatures 210 K, 220 K and 230 K. The maximum ice water content IWC_{\max} is shown in the upper subfigure a). The relative deviation of IWC_{\max} from the non-seeding scenario at $n_{\text{INP}} = 0$ is shown in the bottom subfigure b). Regimes are highlighted in the middle plot of subfigure b) and are representative for the other subplots. These regimes are described in the text with respect to n_{ice}^{\max} .

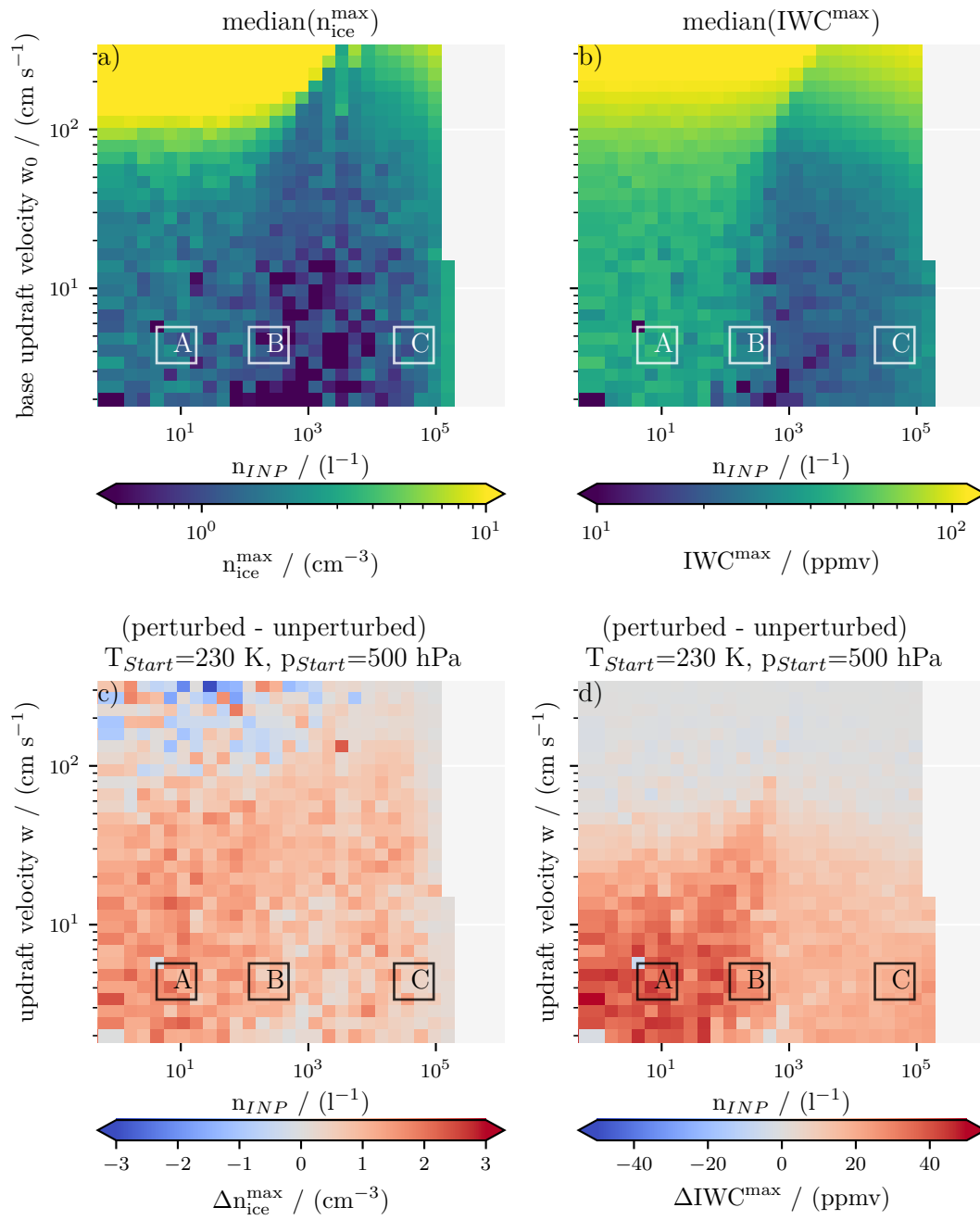


Figure 5.4.7 The median of quantitative ice metrics based on 50 model runs with updraft fluctuations. The parameters for the updraft fluctuations are $\sigma_w = 15 \text{ cm s}^{-1}$ and $\tau_c = \frac{1}{N} = 200 \text{ s}$. The scenarios had a starting temperature of 230 K and a starting pressure of 500 hPa.

Due to this variability the distribution of $n_{\text{ice}}^{\text{max}}$ and IWC_{max} for selected scenario subsets is further analyzed. The subsets A, B and C are indicated in Figure 5.4.7 and represent 800 individual model runs ($4 \times 4 \times 50$), respectively. Subset A represents low seeding, subset B includes model runs from the transition towards optimal seeding and subset C resides in the transition region towards overseeding. Figure 5.4.8 shows histograms of $n_{\text{ice}}^{\text{max}}$ and IWC_{max} for each subset. The median of the respective scenarios without updraft fluctuations is included as well. The histograms are extended by the quantiles of the underlying data.

In Figure 5.4.8 shows histograms of $n_{\text{ice}}^{\text{max}}$ and IWC_{max} for the runs, which are contained in each subset. In each subplot, the left most bar includes the runs which don't have any ice formed. This is the case for runs where the fluctuations quickly change the updraft to a downward movement. The quantiles line emphasizes that more than 10 % of all runs don't show any significant ice nucleation.

In subset A (upper row of Figure 5.4.8) the maximum ice crystal number concentrations forms a bimodal distribution. The left mode belongs to the heterogeneous nucleation mode and refers to successful seeding. For this subset the seeding leads to a successfully thinned cirrus cloud in about 20 % of the the model runs. However, more than half of the model runs reside in the mode of thicker cirrus. This thicker cirrus mode exceeds the median $n_{\text{ice}}^{\text{max}}$ from the respective subset with unperturbed updrafts (pink vertical line). To conclude: a wide spread in cirrus thicknesses is observed, which can not be controlled by low seeding concentrations, since the fluctuations are too dominant. However, even for low seeding concentrations more than 30 % of the model runs did not lead to a thick cirrus cloud.

Subset B (middle row of Figure 5.4.8) shows runs with moderate seeding. Those runs derive from a regime, which is assumed to be suitable for optimal seeding. Due to the increased amount of INPs the thin cirrus mode shifts towards higher $n_{\text{ice}}^{\text{max}}$ and IWC_{max} and causes both cirrus modes to overlap. Also for subset B it has to be stated that CCT provides little control over the resulting total ice number concentration. Yet, about 40 % of the model runs are represented by bins smaller than the dominant homogeneous freezing mode. Subtracting the 10 % of runs which didn't show any ice at all, about 30 % of the runs show thinner clouds due to CCT.

Subset C (bottom row in Figure 5.4.8) is characterized by overseeding. Hence, the thin cirrus mode has shifted towards the thick cirrus mode which results in a single dominant mode of thick cirrus. The resulting mode in $n_{\text{ice}}^{\text{max}}$ and IWC_{max} is similar to what is expected for pure homogeneous cirrus formation.

The discussion of the ice formation statistics within selected subsets shows a severe weak spot of the concept of cirrus cloud thinning. Without an exact knowledge of the boundary conditions and the present dynamics the resulting cirrus thickness can be

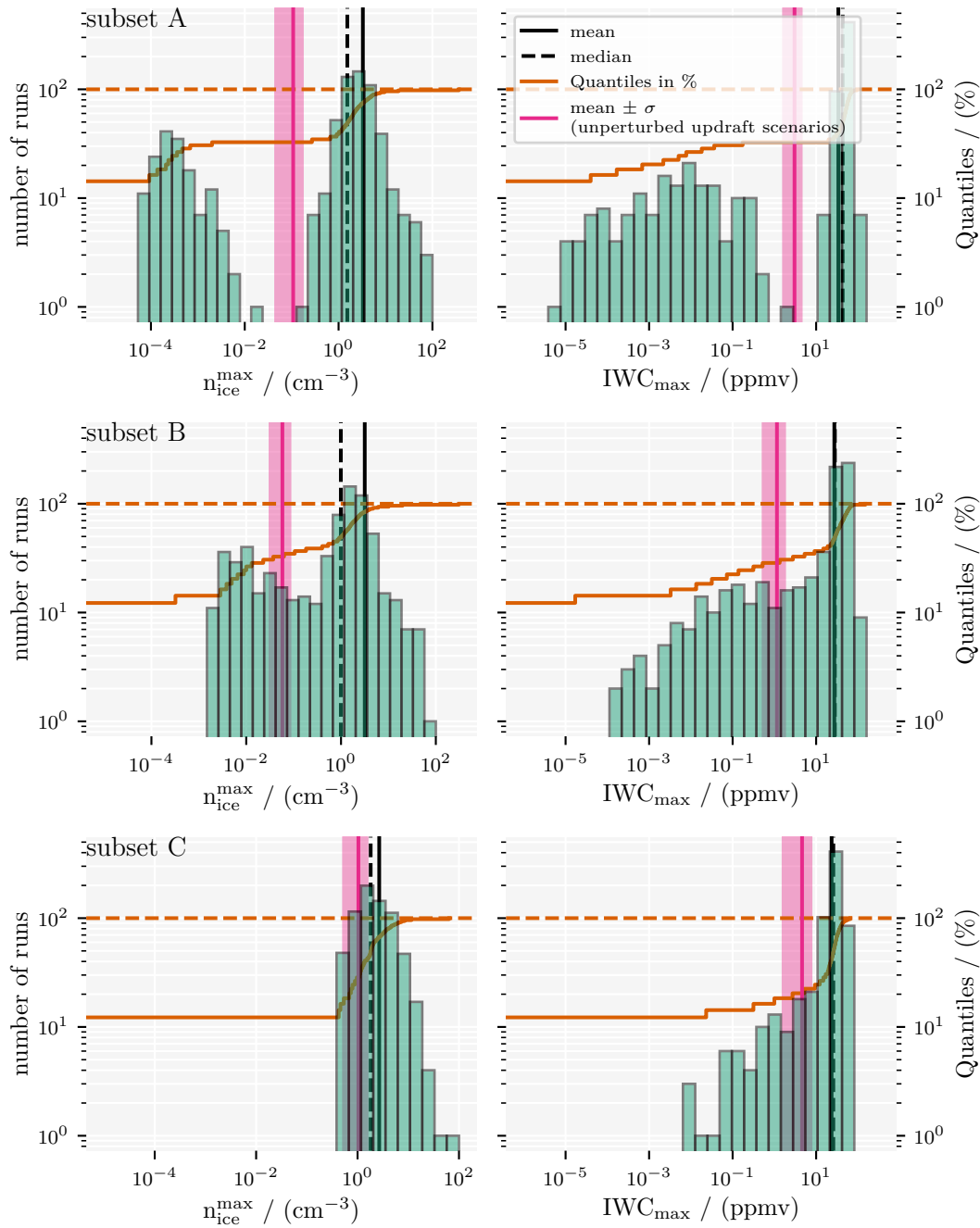


Figure 5.4.8 Histograms of $n_{\text{ice}}^{\text{max}}$ (left) and IWC_{max} (right) for run subsets A, B & C (rows). The subsets are indicated in Figure 5.4.8 and represent a set of 800 runs, respectively. The parameters for the underlying dataset is described in the text with respect to Figure 5.4.7. The quantiles curve describes the fraction of dataset represented by the bins from small to high abscissa values.

extremely variable. Therefore the outcome of a CCT can be hardly predicted. However, from a statistical perspective CCT causes thinner clouds in 20 % to 30 % of the low to moderate seeding scenarios.

Chapter 6

Summary and Outlook

The effectiveness of [CCT](#) is investigated through experiments at the [AIDA](#) cloud chamber facility and atmospheric simulations using the Lagrangian parcel model MAID. Both approaches revealed parameter regions with optimal seeding, where the ice crystal number concentration of cirrus clouds most effectively reduced. However, the model simulations span over a wider parameter space and show the sensitivity of cirrus cloud densities at more atmospherically relevant conditions.

The experimental part contains 168 expansion experiments under [UTLS](#) conditions. We combined different seeding aerosol types ([INPs](#)), namely fumed silica, quartz and calcium carbonate, with aqueous sulfuric acid solution particles to investigate the competition between freezing mechanisms. From the heterogeneous ice formation experiments [INAS](#) density based freezing parameterizations are derived for each [INP](#) type. Investigating the competition between heterogeneous and homogeneous freezing revealed a window of optimal [INP](#) seeding concentrations for all three [INP](#) types. The experimental dataset showing the freezing competition is unique and could be highly valuable for modelers to validate the representation of cirrus microphysics. Yet, the experiments were conducted at comparably fast cooling rates to circumvent the heat flux from the chamber walls. Future studies should use the new cloud chamber AIDA_d at KIT/IMK-AAF with actively cooled walls to complement the existing dataset with slower cooling rates.

In this work the [Model for Aerosol and Ice Dynamics \(MAID\)](#) was significantly improved and extended with additional functionalities. The main developments are a new heterogeneous freezing scheme and the implementation of gravity wave based fluctuations along updraft scenarios. The new heterogeneous freezing scheme can directly integrate the experimentally derived [INAS](#) density parameterizations.

For trajectories simulated along adiabatic updrafts we could show that the maximum ice crystal number concentrations and the maximum [IWCs](#) show parameter regimes of most efficient cirrus seeding. However, the patterns also show regimes with increased ice crystal number concentration (i.e. overseeding), due to the complex interplay of various parameters.

To investigate the impact of gravity wave based updraft fluctuations additional model runs were conducted. For ensembles with stochastically varying updraft fluctuations the median ice crystal number concentration and **IWC** are significantly higher for updraft velocities below 50 cm s^{-1} to 100 cm s^{-1} , compared to the unperturbed model runs. The same metrics show also parameter regions of optimal seeding, even though those are less pronounced.

As part of a more detailed analysis the statistical variability of ice crystal concentration distributions was compared between different ensemble runs. Across ensembles, there are two ice crystal modes. The first mode represents very efficient suppression of cirrus formation and the second mode represents thicker cirrus which includes homogeneous freezing. The first mode is formed by 20 % to 30 % of the model runs at low to moderate seeding. However this mode shifts towards the thick second mode with increasing seeding concentrations. Towards overseeding scenarios both modes merge into a single mode, making it comparable to pure homogeneous freezing.

A conclusion of this statistical analysis is that a controlled application of **CCT** towards a targeted outcome is challenging. Yet, it can be concluded, that a low to medium background of **INPs** can suppress the formation of cirrus clouds in about 20 % to 30 % of the cases almost completely.

We hope that these findings will contribute to further improvements in representations of cirrus cloud formation. Particularly in more complex models, which also consider vertical cloud extent and radiative properties. The radiative forcing effects of **CCT**, were not evaluated within this work, but are crucial for a quantitative evaluation of the **CCT** concept.

Finally, our results regarding ice crystal number concentrations and ice water contents could be parameterized and included into global climate models to improve the representation of cirrus cloud formation. In the long run this could lead to a better prediction of potential risks and side effects of cirrus cloud thinning.

Bibliography

- [1] AMAP. *AMAP Arctic Climate Change Update 2021: Key Trends and Impacts*. Tromsø, Norway: Arctic Monitoring and Assessment Programme (AMAP), 2021. ISBN: 978-82-7971-201-5.
- [2] D. Barahona and A. Nenes. “Parameterizing the competition between homogeneous and heterogeneous freezing in cirrus cloud formation – monodisperse ice nuclei”. In: *Atmospheric Chemistry and Physics* 9.2 (2009), pp. 369–381. DOI: 10.5194/acp-9-369-2009. URL: <https://acp.copernicus.org/articles/9/369/2009/>.
- [3] D. Barahona and A. Nenes. “Parameterizing the competition between homogeneous and heterogeneous freezing in ice cloud formation – polydisperse ice nuclei”. In: *Atmospheric Chemistry and Physics* 9.16 (Aug. 2009), pp. 5933–5948. DOI: 10.5194/acp-9-5933-2009.
- [4] Donifan Barahona, Andrea Molod, and Heike Kalesse. “Direct estimation of the global distribution of vertical velocity within cirrus clouds”. In: *Scientific Reports* 7.1 (July 2017). DOI: 10.1038/s41598-017-07038-6.
- [5] Stefan Benz et al. “T-dependent rate measurements of homogeneous ice nucleation in cloud droplets using a large atmospheric simulation chamber”. In: *Journal of Photochemistry and Photobiology A: Chemistry* 176.1-3 (Dec. 2005), pp. 208–217. DOI: 10.1016/j.jphotochem.2005.08.026.
- [6] Theodore L. Bergman et al. *Fundamentals of heat and mass transfer*. Ed. by Linda Ratts. Wiley, 2011. ISBN: 9780470501979.
- [7] Robert Byron Bird, Warren E. Stewart, and Edwin N. Lightfoot. *Transport Phenomena*. Ed. by Wayne Anderson. 2nd ed. Vol. 55. 1. John Wiley & Sons Inc, 2002. ISBN: 978-0-470-11539-8. DOI: 10.1115/1.1424298. URL: <https://doi.org/10.1115/1.1424298>.
- [8] Alexei Botchkarev. “A New Typology Design of Performance Metrics to Measure Errors in Machine Learning Regression Algorithms”. In: *Interdisciplinary Journal of Information, Knowledge, and Management* 14 (2019), pp. 045–076. DOI: 10.28945/4184.
- [9] Olivier Boucher. *Atmospheric Aerosols. Properties and Climate Impacts*. Springer eBook Collection. Dordrecht: Springer, 2015. 31111132 pp. ISBN: 9789401796491. DOI: 10.1007/978-94-017-9649-1.

-
- [10] Helmut Bunz and Ralph Dlugi. “Numerical studies on the behaviour of aerosols in smog chambers”. In: *Journal of Aerosol Science* 22.4 (Jan. 1991), pp. 441–465. DOI: 10.1016/0021-8502(91)90004-2.
- [11] Helmut Bunz et al. “MAID: a model to simulate UT/LS aerosols and ice clouds”. In: *Environmental Research Letters* 3.3 (July 2008), p. 035001. DOI: 10.1088/1748-9326/3/3/035001.
- [12] Kenneth S. Carslaw, Beiping Luo, and Thomas Peter. “An analytic expression for the composition of aqueous HNO₃-H₂SO₄ stratospheric aerosols including gas phase removal of HNO₃”. In: *Geophysical Research Letters* 22.14 (July 1995), pp. 1877–1880. DOI: 10.1029/95g101668.
- [13] R. J. Cotton et al. “Technical Note: A numerical test-bed for detailed ice nucleation studies in the AIDA cloud simulation chamber”. In: *Atmospheric Chemistry and Physics* 7.1 (Jan. 2007), pp. 243–256. DOI: 10.5194/acp-7-243-2007. URL: www.atmos-chem-phys.net/7/243/2007/.
- [14] B. Dahneke. “Simple Kinetic Theory of Brownian Diffusion in Vapors and Aerosols”. In: *Theory of Dispersed Multiphase Flow*. Elsevier, 1983, pp. 97–133. DOI: 10.1016/b978-0-12-493120-6.50011-8.
- [15] D. W. Fahey et al. “The AquaVIT-1 intercomparison of atmospheric water vapor measurement techniques”. In: *Atmospheric Measurement Techniques* 7.9 (Sept. 2014), pp. 3177–3213. DOI: 10.5194/amt-7-3177-2014.
- [16] Blaž Gasparini and Ulrike Lohmann. “Why cirrus cloud seeding cannot substantially cool the planet”. In: *Journal of Geophysical Research: Atmospheres* 121.9 (May 2016), pp. 4877–4893. DOI: 10.1002/2015jd024666. URL: <https://agupubs.onlinelibrary.wiley.com/doi/full/10.1002/2015JD024666>.
- [17] Blaž Gasparini et al. “To what extent can cirrus cloud seeding counteract global warming?” In: *Environmental Research Letters* 15.5 (Apr. 2020), p. 054002. DOI: 10.1088/1748-9326/ab71a3.
- [18] I. V. Gensch et al. “Supersaturations, microphysics and nitric acid partitioning in a cold cirrus cloud observed during CR-AVE 2006: an observation–modelling intercomparison study”. In: *Environmental Research Letters* 3.3 (July 2008), p. 035003. DOI: 10.1088/1748-9326/3/3/035003.
- [19] Simon Gruber et al. “A Process Study on Thinning of Arctic Winter Cirrus Clouds With High-Resolution ICON-ART Simulations”. In: *Journal of Geophysical Research: Atmospheres* 124.11 (June 2019), pp. 5860–5888. DOI: 10.1029/2018jd029815.
- [20] W. D. Hall and H. R. Pruppacher. “The Survival of Ice Particles Falling from Cirrus Clouds in Subsaturated Air”. In: *Journal of the Atmospheric Sciences* 33.10 (Oct. 1976), pp. 1995–2006. DOI: 10.1175/1520-0469(1976)033<1995:tsoipf>2.0.co;2. URL: [https://doi.org/10.1175/1520-0469\(1976\)033%3C1995:Tsoipf%3E2.0.CO;2](https://doi.org/10.1175/1520-0469(1976)033%3C1995:Tsoipf%3E2.0.CO;2).

- [21] Andrew J. Heymsfield and Jean Iaquinta. “Cirrus Crystal Terminal Velocities”. In: *Journal of the Atmospheric Sciences* 57.7 (Apr. 2000), pp. 916–938. DOI: 10.1175/1520-0469(2000)057<0916:cctv>2.0.co;2.
- [22] Andrew J. Heymsfield et al. “Cirrus Clouds”. In: *Meteorological Monographs* 58 (Jan. 2017), pp. 2.1–2.26. DOI: 10.1175/amsmonographs-d-16-0010.1.
- [23] James R. Holton et al. “Stratosphere-troposphere exchange”. In: *Reviews of Geophysics* 33.4 (Nov. 1995), pp. 403–439. DOI: 10.1029/95rg02097.
- [24] Corinna Hoose and Ottmar Möhler. “Heterogeneous ice nucleation on atmospheric aerosols: a review of results from laboratory experiments”. In: *Atmospheric Chemistry and Physics* 12.20 (Oct. 2012), pp. 9817–9854. DOI: 10.5194/acp-12-9817-2012.
- [25] IPCC. *Climate Change 2021: The Physical Science Basis. Contribution of Working Group I to the Sixth Assessment Report of the Intergovernmental Panel on Climate Change*. Vol. In Press. Cambridge, United Kingdom and New York, NY, USA: Cambridge University Press, 2021. DOI: 10.1017/9781009157896.
- [26] L. S. Jackson, J. A. Crook, and P. M. Forster. “An intensified hydrological cycle in the simulation of geoengineering by cirrus cloud thinning using ice crystal fall speed changes”. In: *Journal of Geophysical Research: Atmospheres* 121.12 (June 2016), pp. 6822–6840. DOI: 10.1002/2015jd024304.
- [27] B. Kärcher and M. M. Basko. “Trapping of trace gases in growing ice crystals”. In: *Journal of Geophysical Research: Atmospheres* 109.D22 (Nov. 2004). DOI: 10.1029/2004jd005254.
- [28] B. Kärcher, E. J. Jensen, and U. Lohmann. “The Impact of Mesoscale Gravity Waves on Homogeneous Ice Nucleation in Cirrus Clouds”. In: *Geophysical Research Letters* 46.10 (May 2019), pp. 5556–5565. DOI: 10.1029/2019gl082437.
- [29] B. Kärcher and A. Podglajen. “A Stochastic Representation of Temperature Fluctuations Induced by Mesoscale Gravity Waves”. In: *Journal of Geophysical Research: Atmospheres* 124.21 (Nov. 2019), pp. 11506–11529. DOI: 10.1029/2019jd030680.
- [30] B. Kärcher and C. Voigt. “Formation of nitric acid/water ice particles in cirrus clouds”. In: *Geophysical Research Letters* 33.8 (2006). DOI: 10.1029/2006gl025927.
- [31] B. Kärcher et al. “Studies on the Competition Between Homogeneous and Heterogeneous Ice Nucleation in Cirrus Formation”. In: *Journal of Geophysical Research: Atmospheres* 127.3 (Feb. 2022). DOI: 10.1029/2021jd035805.
- [32] Bernd Kärcher. “Cirrus Clouds and Their Response to Anthropogenic Activities”. In: *Current Climate Change Reports* 3.1 (Feb. 2017), pp. 45–57. DOI: 10.1007/s40641-017-0060-3.
- [33] Bernd Kärcher, J. Hendricks, and Ulrike Lohmann. “Physically based parameterization of cirrus cloud formation for use in global atmospheric models”. In: *Journal of Geophysical Research* 111.D1 (2006). DOI: 10.1029/2005JD006219.

-
- [34] Bernd Kärcher and Ulrike Lohmann. “A parameterization of cirrus cloud formation: Homogeneous freezing of supercooled aerosols”. In: *Journal of Geophysical Research* 107.D2 (2002). DOI: 10.1029/2001jd000470.
- [35] Bernd Kärcher and Ulrike Lohmann. “A parameterization of cirrus cloud formation: Heterogeneous freezing”. In: *Journal of Geophysical Research* 108.D14 (2003). DOI: 10.1029/2002jd003220.
- [36] Thomas Koop et al. “Water activity as the determinant for homogeneous ice nucleation in aqueous solutions”. In: *Nature* 406.6796 (Aug. 2000), pp. 611–614. DOI: 10.1038/35020537.
- [37] Greg Kopp and Judith L. Lean. “A new, lower value of total solar irradiance: Evidence and climate significance”. In: *Geophysical Research Letters* 38.1 (Jan. 2011), n/a–n/a. DOI: 10.1029/2010gl045777.
- [38] Martina Krämer et al. “A microphysics guide to cirrus clouds – Part 1: Cirrus types”. In: *Atmospheric Chemistry and Physics* 16.5 (Mar. 2016), pp. 3463–3483. DOI: 10.5194/acp-16-3463-2016.
- [39] Martina Krämer et al. “A microphysics guide to cirrus – Part 2: Climatologies of clouds and humidity from observations”. In: *Atmospheric Chemistry and Physics* 20.21 (Nov. 2020), pp. 12569–12608. DOI: 10.5194/acp-20-12569-2020.
- [40] Stefanie Kremser et al. “Stratospheric aerosol-Observations, processes, and impact on climate: Stratospheric Aerosol”. In: *Reviews of Geophysics* 54.2 (May 2016), pp. 278–335. ISSN: 8755-1209. DOI: 10.1002/2015rg000511.
- [41] Jón Egill Kristjánsson, Helene Muri, and Hauke Schmidt. “The hydrological cycle response to cirrus cloud thinning”. In: *Geophysical Research Letters* 42.24 (Dec. 2015), pp. 10, 807–10, 815. DOI: 10.1002/2015gl066795.
- [42] M. Kuebbeler et al. “Dust ice nuclei effects on cirrus clouds”. In: *Atmospheric Chemistry and Physics* 14.6 (Mar. 2014), pp. 3027–3046. DOI: 10.5194/acp-14-3027-2014.
- [43] Jiaojiao Liu and Xiangjun Shi. “Estimating the potential cooling effect of cirrus thinning achieved via the seeding approach”. In: *Atmospheric Chemistry and Physics* 21.13 (July 2021), pp. 10609–10624. ISSN: 1680-7324. DOI: 10.5194/acp-21-10609-2021.
- [44] Xiaohong Liu and Joyce E. Penner. “Ice nucleation parameterization for global models”. In: *Meteorologische Zeitschrift* 14.4 (Sept. 2005), pp. 499–514. DOI: 10.1127/0941-2948/2005/0059.
- [45] Ulrike Lohmann, Felix Lüönd, and Fabian Mahrt. *Introduction to Clouds – From the Microscale to Climate. From the Microscale to Climate*. Cambridge University Press, 2016, p. 399. ISBN: 9781107018228.

- [46] Anna E. Luebke et al. “The origin of midlatitude ice clouds and the resulting influence on their microphysical properties”. In: *Atmospheric Chemistry and Physics* 16.9 (May 2016), pp. 5793–5809. ISSN: 1680-7324. DOI: 10.5194/acp-16-5793-2016.
- [47] Alexander Mangold et al. “Experimental investigation of ice nucleation by different types of aerosols in the aerosol chamber AIDA: implications to microphysics of cirrus clouds”. In: *Meteorologische Zeitschrift* 14.4 (Sept. 2005), pp. 485–497. DOI: 10.1127/0941-2948/2005/0053.
- [48] C. Marcolli. “Deposition nucleation viewed as homogeneous or immersion freezing in pores and cavities”. In: *Atmospheric Chemistry and Physics* 14.4 (Feb. 2014), pp. 2071–2104. DOI: 10.5194/acp-14-2071-2014.
- [49] Claudia Marcolli. “Pre-activation of aerosol particles by ice preserved in pores”. In: *Atmospheric Chemistry and Physics* 17.3 (Feb. 2017), pp. 1595–1622. DOI: 10.5194/acp-17-1595-2017.
- [50] Emmanuel Martin, Christian George, and Philippe Mirabel. “Densities and surface tensions of H₂SO₄/HNO₃/H₂O solutions”. In: *Geophysical Research Letters* 27.2 (Jan. 2000), pp. 197–200. DOI: 10.1029/1999gl1010892.
- [51] David L. Mitchell and William Finnegan. “Modification of cirrus clouds to reduce global warming”. In: *Environmental Research Letters* 4.4 (Oct. 2009), p. 045102. DOI: 10.1088/1748-9326/4/4/045102.
- [52] O. Möhler et al. “Experimental investigation of homogeneous freezing of sulphuric acid particles in the aerosol chamber AIDA”. In: *Atmospheric Chemistry and Physics* 3.1 (Feb. 2003), pp. 211–223. DOI: 10.5194/acp-3-211-2003.
- [53] O. Möhler et al. “Efficiency of the deposition mode ice nucleation on mineral dust particles”. In: *Atmospheric Chemistry and Physics* 6.10 (July 2006), pp. 3007–3021. ISSN: 1680-7324. DOI: 10.5194/acp-6-3007-2006.
- [54] H. Muri et al. “The climatic effects of modifying cirrus clouds in a climate engineering framework”. In: *Journal of Geophysical Research: Atmospheres* 119.7 (Apr. 2014), pp. 4174–4191. DOI: 10.1002/2013jd021063.
- [55] D. M. Murphy and T. Koop. “Review of the vapour pressures of ice and super-cooled water for atmospheric applications”. In: *Quarterly Journal of the Royal Meteorological Society* 131.608 (Apr. 2005), pp. 1539–1565. DOI: 10.1256/qj.04.94.
- [56] Mario Nachbar, Denis Duft, and Thomas Leisner. “The vapor pressure of liquid and solid water phases at conditions relevant to the atmosphere”. In: *The Journal of Chemical Physics* 151.6 (Aug. 2019), p. 064504. DOI: 10.1063/1.5100364.
- [57] Joyce E. Penner, Cheng Zhou, and Xiaohong Liu. “Can cirrus cloud seeding be used for geoengineering?” In: *Geophysical Research Letters* 42.20 (Oct. 2015), pp. 8775–8782. DOI: 10.1002/2015gl1065992.

-
- [58] Aurélien Podglajen et al. “Lagrangian temperature and vertical velocity fluctuations due to gravity waves in the lower stratosphere”. In: *Geophysical Research Letters* 43.7 (Apr. 2016), pp. 3543–3553. DOI: 10.1002/2016gl068148.
- [59] Process insights. *High Performance for Humidity Measurements*. URL: <https://www.process-insights.com/products-3/products-industrial/chilled-mirror-hygrometers/373-model/>.
- [60] Hans R. Pruppacher and James D. Klett. *Microphysics of Clouds and Precipitation*. Ed. by Richard D. Rosen. 3rd ed. Vol. 18. Springer Netherlands, 2010. ISBN: 0-306-48100-6.
- [61] Mika Rantanen et al. “The Arctic has warmed nearly four times faster than the globe since 1979”. In: *Communications Earth & Environment* 3.1 (Aug. 2022). ISSN: 2662-4435. DOI: 10.1038/s43247-022-00498-3.
- [62] James Riordon, Elizabeth Zubritsky, and Alan Newman. *Top 10 Articles*. 2000.
- [63] C. Rolf et al. “Lidar observation and model simulation of a volcanic-ash-induced cirrus cloud during the Eyjafjallajökull eruption”. In: *Atmospheric Chemistry and Physics* 12.21 (Nov. 2012), pp. 10281–10294. DOI: 10.5194/acp-12-10281-2012.
- [64] Kenneth Sassen, Zhien Wang, and Dong Liu. “Global distribution of cirrus clouds from CloudSat/Cloud-Aerosol Lidar and Infrared Pathfinder Satellite Observations (CALIPSO) measurements”. In: *Journal of Geophysical Research: Atmospheres* 113.D8 (Apr. 2008). ISSN: 0148-0227. DOI: 10.1029/2008jd009972.
- [65] Abraham Savitzky and Marcel JE Golay. “Smoothing and differentiation of data by simplified least squares procedures.” In: *Analytical chemistry* 36.8 (1964), pp. 1627–1639.
- [66] Ronald Schafer. “What Is a Savitzky-Golay Filter? [Lecture Notes]”. In: *IEEE Signal Processing Magazine* 28.4 (July 2011), pp. 111–117. DOI: 10.1109/msp.2011.941097.
- [67] Martin Schnaiter et al. “Influence of particle size and shape on the backscattering linear depolarisation ratio of small ice crystals – cloud chamber measurements in the context of contrail and cirrus microphysics”. In: *Atmospheric Chemistry and Physics* 12.21 (Nov. 2012), pp. 10465–10484. DOI: 10.5194/acp-12-10465-2012.
- [68] Julia Schneider et al. “High homogeneous freezing onsets of sulfuric acid aerosol at cirrus temperatures”. In: *Atmospheric Chemistry and Physics* 21.18 (Sept. 2021), pp. 14403–14425. DOI: 10.5194/acp-21-14403-2021.
- [69] Tobias Schorr. *AIDA analysis software 'aida_experiment_analysis'*. 2023. URL: https://codebase.helmholtz.cloud/groups/aida/aida_experiment_analysis.
- [70] Tobias Schorr. *Size distribution analysis software 'psd_analysis'*. 2023. URL: https://codebase.helmholtz.cloud/groups/aida/psd_analysis.
- [71] Tobias Schorr et al. *MAID - Model for Aerosol and Ice Dynamics*. 2023. URL: <https://codebase.helmholtz.cloud/maid/maid>.

- [72] James A. Screen and Ian Simmonds. “The central role of diminishing sea ice in recent Arctic temperature amplification”. In: *Nature* 464.7293 (Apr. 2010), pp. 1334–1337. DOI: 10.1038/nature09051.
- [73] John H. Seinfeld and Spyros N. Pandis. *Atmospheric Chemistry and Physics From Air Pollution to Climate Change. From Air Pollution to Climate Change*. 3rd ed. Wiley and Sons, Incorporated, John, 2016, p. 1152. ISBN: 9781119221166. eprint: 9781119221166.
- [74] SIGMA-ALDRICH. *Calcium carbonate product page*. URL: <https://www.sigmaaldrich.com/DE/de/product/aldrich/310034>.
- [75] SIGMA-ALDRICH. *Fumed silica product page*. Data sheet of fumed silica. URL: <https://www.sigmaaldrich.com/DE/de/product/SIGMA/S5505>.
- [76] P. Spichtinger and K. M. Gierens. “Modelling of cirrus clouds – Part 1a: Model description and validation”. In: *Atmospheric Chemistry and Physics* 9.2 (Jan. 2009), pp. 685–706. DOI: 10.5194/acp-9-685-2009.
- [77] Peter Spichtinger and Dan J. Cziczo. “Impact of heterogeneous ice nuclei on homogeneous freezing events in cirrus clouds”. In: *Journal of Geophysical Research* 115.D14208 (2010). DOI: 10.1029/2009jd012168.
- [78] I. Steinke et al. “A new temperature- and humidity-dependent surface site density approach for deposition ice nucleation”. In: *Atmospheric Chemistry and Physics* 15.7 (Apr. 2015), pp. 3703–3717. DOI: 10.5194/acp-15-3703-2015.
- [79] T. Storelvmo, W. R. Boos, and N. Herger. “Cirrus cloud seeding: a climate engineering mechanism with reduced side effects?” In: *Phil. Trans. R. Soc. A* 372.2031 (Dec. 2014), p. 20140116. DOI: 10.1098/rsta.2014.0116.
- [80] T. Storelvmo et al. “Cirrus cloud seeding has potential to cool climate”. In: *Geophysical Research Letters* 40.1 (2013), pp. 178–182. DOI: 10.1029/2012GL054201. URL: <https://agupubs.onlinelibrary.wiley.com/doi/abs/10.1029/2012GL054201>.
- [81] Azadeh Tabazadeh et al. “A new parameterization of H₂SO₄/H₂O aerosol composition: Atmospheric implications”. In: *Geophysical Research Letters* 24.15 (Aug. 1997), pp. 1931–1934. DOI: 10.1029/97g101879.
- [82] William Thomson. “On the Equilibrium of Vapour at a Curved Surface of Liquid”. In: *Proceedings of the Royal Society of Edinburgh* 7 (1872), pp. 63–68. DOI: 10.1017/S0370164600041729. URL: <https://www.cambridge.org/core/journals/proceedings-of-the-royal-society-of-edinburgh/article/abs/4-on-the-equilibrium-of-vapour-at-a-curved-surface-of-liquid/FE2D8D526BD8347E46274E63329AA521>.
- [83] Colin Tully et al. “Cirrus cloud thinning using a more physically based ice microphysics scheme in the ECHAM-HAM general circulation model”. In: *Atmospheric Chemistry and Physics* 22.17 (Sept. 2022), pp. 11455–11484. DOI: 10.5194/acp-22-11455-2022.

-
- [84] Colin Tully et al. “Does prognostic seeding along flight tracks produce the desired effects of cirrus cloud thinning?” In: *Atmospheric Chemistry and Physics* 23.13 (July 2023), pp. 7673–7698. DOI: 10.5194/acp-23-7673-2023.
- [85] Romy Ullrich et al. “A New Ice Nucleation Active Site Parameterization for Desert Dust and Soot”. In: *Journal of the Atmospheric Sciences* 74.3 (Mar. 2017), pp. 699–717. DOI: 10.1175/jas-d-16-0074.1.
- [86] Gabor Vali. “Quantitative Evaluation of Experimental Results on the Heterogeneous Freezing Nucleation of Supercooled Liquids”. In: *Journal of the Atmospheric Sciences* 28.3 (Apr. 1971), pp. 402–409. DOI: 10.1175/1520-0469(1971)028<0402:qeoera>2.0.co;2.
- [87] Guido Visconti. *Fundamentals of Physics and Chemistry of the Atmosphere*. Springer International Publishing, 2016. DOI: 10.1007/978-3-319-29449-0.
- [88] Robert Wagner et al. “Infrared Optical Constants of Highly Diluted Sulfuric Acid Solution Droplets at Cirrus Temperatures”. In: *The Journal of Physical Chemistry A* 112.46 (Nov. 2008), pp. 11661–11676. DOI: 10.1021/jp8066102.
- [89] Robert Wagner et al. “Pre-activation of ice-nucleating particles by the pore condensation and freezing mechanism”. In: *Atmospheric Chemistry and Physics* 16.4 (Feb. 2016), pp. 2025–2042. DOI: 10.5194/acp-16-2025-2016.
- [90] Veronika Wolf, Thomas Kuhn, and Martina Krämer. “On the Dependence of Cirrus Parametrizations on the Cloud Origin”. In: *Geophysical Research Letters* 46.21 (Nov. 2019), pp. 12565–12571. ISSN: 1944-8007. DOI: 10.1029/2019g1083841.
- [91] Veronika Wolf et al. “Arctic ice clouds over northern Sweden: microphysical properties studied with the Balloon-borne Ice Cloud particle Imager B-ICI”. In: *Atmospheric Chemistry and Physics* 18.23 (Dec. 2018), pp. 17371–17386. DOI: 10.5194/acp-18-17371-2018.
- [92] World Meteorological Organization. *2023 shatters climate records, with major impacts*. accessed on 2023-12-07. URL: <https://wmo.int/news/media-centre/2023-shatters-climate-records-major-impacts>.
- [93] Ping Yang et al. “On the radiative properties of ice clouds: Light scattering, remote sensing, and radiation parameterization”. In: *Advances in Atmospheric Sciences* 32.1 (Nov. 2014), pp. 32–63. DOI: 10.1007/s00376-014-0011-z.

Appendix A

General evaluation methods

This appendix collects general descriptions about methods, which were used in the thesis. It covers evaluation metrics for data comparison and highlights the working principle and usefulness of a Savitzky-Golay filter for data smoothing.

A.1 Metrics for model evaluation and data comparison

Having two datasets describing the same quantity leads to the question how they can be compared on the basis of a quantitative metric. Depending on the context one can be interested in different metrics, like absolute errors, relative deviations or systematic biases.

Since the following metrics have a rather inconsistent nomenclature in literature ¹, we stick to the naming convention by Botchkarev [8, Appendix B]. Furthermore, those metrics are mostly mentioned in the context of model evaluation. However, they can also be used to compare other types of datasets, like time series data from various laboratory instruments. Potential use cases for comparing two datasets A & B can be

Dataset A		Dataset B
Model	vs.	Exp. observation
Model run i	vs.	Model run j
Model (1)	vs.	Model (2)
Instrument X data	vs.	Instrument Y data

¹Botchkarev [8] defines *Mean error* (ME) as what is called *Mean Bias* (MB) by Seinfeld and Pandis [73, chapter 25.7]. Vice versa, [73] defines *Mean error* (ME) as what is described as *Mean absolute error* (MAE) in [8], leading to contradicting definitions.

A.1.1 Absolute error metrics

The **mean absolute error (MAE)** is a common evaluation metric and defined as

$$MAE = \frac{1}{N} \sum_{i=1}^N |A_i - B_i| \quad (\text{A.1})$$

with N data points for the datasets A and B . Though from this metric one can't tell if the **MAE** is caused by a systematic shift between A & B or simply by noisy data.

A.1.2 Bias metrics

The **mean error (ME)**, or Mean Bias Error, is closely related to the [equation \(A.1\)](#) and defined as

$$ME = \frac{1}{N} \sum_{i=1}^N A_i - B_i \quad (\text{A.2})$$

However, here the sign of the difference between two data points (A_i, B_i) is preserved. Therefore the absolute value of the **ME** increases for systematic deviations, whereas **ME** is small for noise-like contributions.

Note

At this point one can see that the two metric types, bias and absolute error, complement each other well. Both values in combination can already lead to a meaningful conclusion about the relation between two datasets.

A.1.3 Normalized metrics (bias and absolute error)

The two previous metrics, **ME** and **MAE**, have a major drawback. Their absolute value is proportional to the magnitude of the evaluated data points. Therefore it has no meaning to compare the **ME** or **MAE** values if the underlying datasets had different magnitudes (e.g. low vs. high aerosol number concentrations).

Thus we will introduce two further metrics for the two metric types, respectively.

The **mean absolute relative error (MARE)** is the equivalent to **MAE**, but normalized with respect to one of the datasets:

$$MARE = \frac{1}{N} \sum_{i=1}^N \frac{|A_i - B_i|}{|A_i|} \quad (\text{A.3})$$

A.1 Metrics for model evaluation and data comparison

The **mean normalized bias (MNB)** is the equivalent to **ME**, but normalized with respect to one of the datasets:

$$MNB = \frac{1}{N} \sum_{i=1}^N \frac{A_i - B_i}{A_i} \quad (\text{A.4})$$

One can extend this concept by normalizing with respect to both datasets, which leads to the **fractional absolute error (FAE)**

$$FAE = \frac{2}{N} \sum_{i=1}^N \frac{|A_i - B_i|}{|A_i| + |B_i|} \quad (\text{A.5})$$

and the **fractional bias (FB)**

$$FB = \frac{2}{N} \sum_{i=1}^N \frac{A_i - B_i}{A_i + B_i}. \quad (\text{A.6})$$

The main advantage of normalizing with respect to both datasets sticks out when looking at the range of the introduced metrics:

Table A.1.1 Comparison metrics and their range.

metric name	abbrev.	metric type	range
mean error	ME	bias	$-\bar{B}$ to ∞
mean normalized bias	MNB	bias	-1 to ∞
fractional bias	FB	bias	-2 to $+2$
mean average error	MAE	abs. err.	$-\bar{B}$ to ∞
mean average relative error	MARE	abs. err.	0 to ∞
fractional average error	FAE	abs. err.	0 to 2

The range of both, **FAE** and **FB** (equations (A.5) and (A.6)), are limited to finite intervals, no matter if the values of both datasets A & B vary strongly. Thus, using the **FAE** and **FB** we can compare a variety of cases through two clear quantities.

Yet, absolute values of the the fractional bias are not intuitively easy translated to the underlying deviation between dataset A & B. Therefore [Figure A.1.1](#) shows the fractional bias as a function of a factor f being applied onto dataset A. Obviously, **FB** is most sensitive for small deviations between two datasets and loses this sensitivity with increasing deviation.

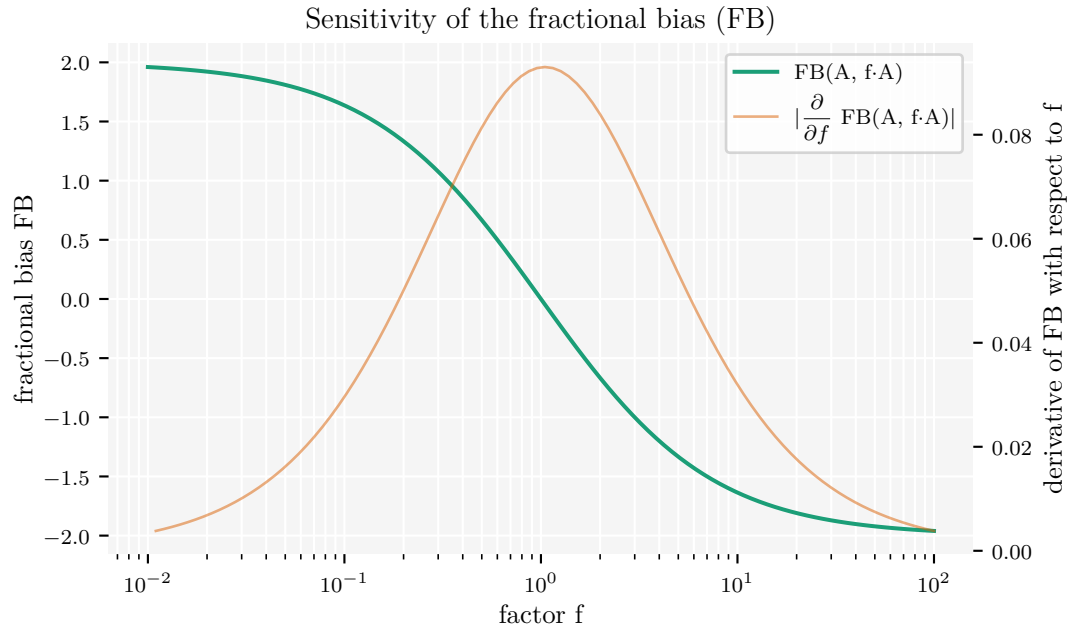


Figure A.1.1 Fractional bias (green) between a dataset A and another dataset fA , with the scaling factor f being applied on. Its derivative (orange) shows the highest sensitivity of the fractional bias around 1, decreasing to low sensitivities for factors f of 0.01 and 100, respectively.

Here, a main use case for these methods is the comparison of various cloud chamber experiments against [MAID](#) box model results. Furthermore, they were used to validate the new [AIDA](#) analysis framework (see [section 3.4.1](#)) against the old established analysis code.

A.2 Smoothing: Savitzky-Golay filter

The Savitzky-Golay filter can be used to smooth 1-dimensional data. It is based on least-squares polynomial approximations applied on a moving window of data points and acts as a low-pass filter.

For the application one has to select the polynomial degree k and a window width N of an uneven number of data points. Hence, the polynomial is described as

$$p(x) = \sum_{k=0}^N a_k x^k. \tag{A.7}$$

The window is moved along the dataset and for each subset the polynomial parameters a are determined using the least-squares method. The optimized polynomial evaluated at the central abscissa value $p_i^{opt}(x_i)$ serves as the smoothed ordinate $y_i^*(x_i)$.

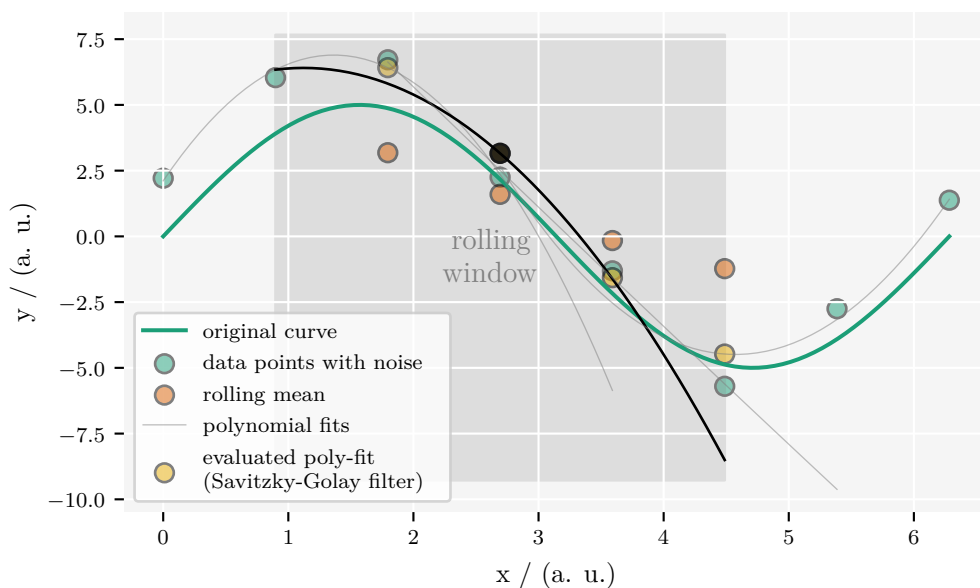


Figure A.2.1 Conceptual example of the Savitzky-Golay smoothing algorithm (yellow), which is applied on an artificially noisy dataset (green). A common *rolling mean* smoothing (orange) is also applied for comparison. The Savitzky-Golay filter represents the original curve better and is more sensitive to high frequency components.

The polynomial order should be chosen in such way, that it fits the nature of the selected data points. Starting with a polynomial order of $k = 2$ should typically be a good choice. For high noise levels the window width should be increased, even though it leads to a loss of *real* high frequency signal components. A meaningful combination of those two parameters have to be determined individually from case to case.

As a great advantage the Savitzky-Golay filter, compared to the widely used *moving average* (or *rolling mean*) method, it introduces less distortion into the smoothed dataset, regarding the shapes and positions of peaks. Moreover it is also less susceptible to outliers

The Savitzky-Golay filter introduces less distortion into the smoothed dataset, regarding the shapes and positions of peaks, when compared to other common smoothing techniques like the widely used *moving average* (or *rolling mean*) method. Moreover it is less susceptible towards outliers and better in preserving high frequency components of the signal. Deeper analyses and comparisons to other smoothing methods can be found in literature. [66, 65]

The method was introduced by Savitzky and Golay back in 1964 [65]. In 2000 the American Chemical Society (ACS) listed the original publication in the top 10 list of seminal papers being published in their journals [62].

In this work the Savitzky-Golay filter is used to reduce noise in TDL data, as well as to reduce noise and smooth outliers in SIMONE data.

Appendix B

AIDA wall flux model

This part describes an approach to calculate the heat flux and water exchange between the gas volume of the AIDA cloud chamber with its inner walls.

This fluid dynamic approach is based on several dimensionless characteristic numbers describing heat- and molecular mass transport in vertical and horizontal components. Subsequently these numbers are coupled to the specific geometry of the AIDA cloud chamber to calculate the fluxes.

The driver for the heat flux is the temperature difference between wall temperature and gas temperature. The driver for the water flux is the difference between the actual water vapor pressure inside the chamber and the water vapor saturation pressure over the wall surface.

B.1 Assumptions

B.1.1 Chamber geometry assumption

The AIDA geometry is approximated as a cylinder to easily separate the chamber wall in a vertical and a horizontal component. The height of this cylinder is calculated by using the real chamber volume¹ of 80.38 m³ and inner radius of 1.98 m. The cylinder height h_{cyl} yields to

$$h_{cyl} = \frac{V}{\pi \cdot r^2} = \frac{80.38 \text{ m}^3}{\pi \cdot (1.98 \text{ m})^2} = 6.53 \text{ m} \quad (\text{B.1})$$

¹The volume was calculated by treating AIDA as a tank with 5.445 m high parallel walls and torispherical top and bottom endings ($r_{max} = 4 \text{ m}$, $r_{min} = 0.4 \text{ m}$, "Klöpfer head").

and the surface A_{cyl} with horizontal and vertical components to

$$A_{cyl}^v = 2\pi \cdot r \cdot h_{cyl} = 81.2 \text{ m}^2 \quad (\text{B.2})$$

$$A_{cyl}^h = \pi \cdot r^2 = 12.32 \text{ m}^2 \quad (\text{B.3})$$

$$A_{cyl} = A_{cyl}^v + 2 \cdot A_{cyl}^h = 105.83 \text{ m}^2, \quad (\text{B.4})$$

with $r = r_{AIDA}$ and $V = V_{AIDA}$. You can see that each horizontal surface contributes only about 11.6 % to the total cylinder surface, whereas the vertical surface component contributes about 77 %.

B.1.2 Wall icing assumption

The wall of the AIDA cloud chamber doesn't get ice covered homogeneously. The cooled chamber wall shows a temperature gradient in vertical direction caused by an inhomogeneous temperature distribution in the thermal housing. Hence we assume that the three chamber surface fractions (see [appendix B.1.1](#)) are getting ice covered one after another according to their specific wall temperatures. The ice coverage of the vertical and horizontal wall component, respectively, is calculated from a total ice coverage fraction fA_{iced} and a case distinction following the rules, leading to:

$$fA_{iced} \Rightarrow \left\{ \begin{array}{ll} \text{I: } 0 \leq fA_{iced} \leq 11.6 \% : & \begin{array}{l} fA_{iced}^v = 0 \\ 0 \leq fA_{iced}^h \leq 50 \% \end{array} \\ \text{II: } 11.6 \% < fA_{iced} \leq 88.4 \% : & \begin{array}{l} 0 < fA_{iced}^v \leq 1 \\ fA_{iced}^h = 50 \% \end{array} \\ \text{III: } 88.4 \% < fA_{iced} \leq 1 : & \begin{array}{l} fA_{iced}^v = 1 \\ 50 \% < fA_{iced}^h \leq 1 \end{array} \end{array} \right. \quad (\text{B.5})$$

B.1.3 Fluid dynamic assumptions

A transport mechanism is often related to a *characteristic length*, representing a given geometry. Regarding the convective heat transport the chamber walls have to be treated separately as vertical and horizontal components with each independent characteristic lengths.

For the heat flux from the vertical wall component we assume a characteristic length L^v of half the radius $\frac{r}{2}$, representing a boundary layer². For the heat flux from the horizontal wall component the characteristic length L^h is the chamber height.

The calculations in systems of natural convection or forced convection rely on different sets of equations. To simplify the calculations we calculate the heat flux as if we had only natural convection in AIDA and then scale the result with an additional factor f to treat the fact that the mixing fan creates an additional forced convection.

B.2 Relevant characteristic fluid dynamic numbers

B.2.1 Prandtl number

The dimensionless Prandtl number is defined as the ratio of kinematic viscosity ν and the thermal diffusivity α .

$$Pr = \frac{\nu}{\alpha}$$

The Prandtl number

- ◇ provides a measure of the relative effectiveness of momentum and energy transport by diffusion in the velocity and thermal boundary layers, respectively [6].
- ◇ indicates the relative ease of momentum and energy transport in flow systems [7].

The kinematic viscosity ν is equal to the ratio of dynamic viscosity and the density $\frac{\eta}{\rho}$ and the thermal diffusivity can be expressed as $\alpha = \frac{\lambda}{c_p \cdot \rho}$ with the thermal conductivity λ . These relations lead to an equivalent expression of the Prandtl number

$$\begin{aligned} Pr &= \frac{\nu}{\alpha} = \frac{\eta}{\rho \cdot \alpha} = \frac{\eta}{\rho} \cdot \frac{c_p \cdot \rho}{\lambda} \\ &= \frac{c_p \cdot \eta}{\lambda} \end{aligned} \tag{B.6}$$

²Assumption adopted from earlier calculations done by Helmut Bunz.

The dynamic viscosity η in equation (B.6) can be derived through the Sutherland model as

$$\eta(T) = \mu_0 \cdot \frac{T_0 + C}{T + C} \cdot \left(\frac{T}{T_0} \right)^{\frac{3}{2}} \quad \text{in Pa s} \quad (\text{B.7})$$

with: $C = 120 \text{ K}$ Sutherland constant
 $T_0 = 291.15 \text{ K}$ reference temperature
 $\mu_0 = 18.27 \times 10^{-6} \text{ Pa s}$ reference viscosity at T_0 .

The thermal conductivity λ can be expressed as a function of temperature

$$\lambda(T_C) = (24.5286 + 7.6749 \times 10^{-2} \cdot T_C - 4.21645 \times 10^{-5} \cdot T_C^2) \times 10^{-3} \quad (\text{B.8})$$

in $\text{J m}^{-1} \text{s}^{-1} \text{K}^{-1}$ (or $\text{kg m s}^{-3} \text{K}^{-1}$) as a function of temperature T_C in $^{\circ}\text{C}$.

Heat capacity of dry air can be calculated as

$$c_p^{dry}(T_C) = 1005.07 - 5.18275 \times 10^{-3} \cdot T_C + 8.90574 \times 10^{-4} \cdot T_C^2$$

with temperature T_C in $^{\circ}\text{C}$. For humid air the expression can be extended with an additional term leading to the expression

$$c_p(T_C, p, p_w) = c_p^{dry}(T_C) \cdot \frac{p - p_w}{p} + 1884.06 \cdot \frac{p_w}{p} \quad (\text{B.9})$$

in $\text{J kg}^{-1} \text{K}^{-1}$ with water vapor pressure p_w in Pa and pressure p in Pa.

With equations (B.7) to (B.9) the Prandtl number Pr can be calculated according to equation (B.6) as a function of temperature T , total pressure p and water vapor pressure p_w , which are all continuously measured.

B.2.2 Schmidt number

The dimensionless Schmidt number Sc is defined as

$$Sc = \frac{\nu}{D} = \frac{\mu}{\rho \cdot D} \quad (\text{B.10})$$

with the kinetic viscosity ν , dynamic viscosity η , density ρ and the diffusion coefficient D .

The Schmidt number

◇ is the mass transfer analogue of the Prandtl number. [7].

The diffusion coefficient of water molecules in air was parameterized by Hall and Pruppacher [20] as a function of temperature T in K and pressure p in Pa [20, eq. 13]:

$$D(T, p) = D_0 \cdot \left(\frac{T}{T_0}\right)^{1.94} \cdot \frac{p_0}{p} \quad \text{in m}^2 \text{ s}^{-1} \quad (\text{B.11})$$

with: $D_0 = 2.11 \times 10^{-5} \text{ m}^2 \text{ s}^{-1}$
 $T_0 = 273.15 \text{ K}$
 $p_0 = 101\,325 \text{ Pa}$

In the original publication this parameterization is accounted to be valid in the temperature range from -80°C to 40°C . However in the newer text book from Pruppacher and Klett the valid temperature range is given from -40°C to 40°C [60, p. 503]. Due to a lack of newer parameterizations this expression is also used to calculate the diffusion coefficient of water for experiments at temperatures below -40°C .

The gas density of air can be expressed by

$$\varrho = \varrho_0 \cdot \frac{p}{p_0} \cdot \frac{T_0}{T} \quad (\text{B.12})$$

with: $\varrho_0 = 1.2754 \text{ kg m}^{-3}$
 $T_0 = 273.15^\circ\text{C}$
 $p_0 = 1 \times 10^5 \text{ Pa}$

where the given ϱ_0 is the IUPAC standard dry air density at T_0 and p_0 .

With the expressions from equations (B.7), (B.11) and (B.12) the Schmidt number Sc can be calculated by equation (B.10).

B.2.3 Grashof number

The Grashof number is defined as

$$Gr = \frac{g\beta(T_{surf} - T_{gas})L^3}{\nu^2} = \frac{\varrho^2 g\beta(T_{surf} - T_{gas})L^3}{\eta^2} \quad (\text{B.13})$$

with: $g = 9.806\,65 \text{ m s}^{-2}$

where T_{surf} is the surface temperature, T_{gas} the fluid temperature, β the volume expansion coefficient of the fluid and L is the characteristic length for a given geometry. The relation between ϱ , ν and η is described in equation (B.6).

The volume expansion coefficient β for gas can be derived from the ideal gas law to

$$\beta = \frac{1}{T_{gas}}. \quad (\text{B.14})$$

The Grashof number

- ◇ is a measure of the ratio of buoyancy forces to viscous forces. Its role in free convection is much the same as that of the Reynolds number in forced convection. [6]
- ◇ is the characteristic group occurring in analyses of free convection. [7]

B.2.4 Rayleigh number

The Rayleigh number results from the product of the Prandtl number and the Grashof number

$$\begin{aligned}
 Ra &= Pr \cdot Gr \\
 &\Downarrow \text{equations (B.6) and (B.13)} \\
 &= \frac{c_p}{\lambda} \cdot \frac{\rho^2 g \beta (T_{surf} - T_{fluid}) L^3}{\eta}
 \end{aligned}
 \tag{B.15}$$

and is relevant to describe systems with natural convection.

The Rayleigh number

- ◇ is a measure of the ratio of buoyancy forces to viscous forces. Its role in free convection is much the same as that of the Reynolds number in forced convection. [6]
- ◇ characterizes the fluid's flow regime: a value in a certain lower range denotes laminar flow; a value in a higher range, turbulent flow.^a

^aadapted from https://en.wikipedia.org/wiki/Rayleigh_number, 13.12.2020

B.2.5 Nusselt number

The Nusselt number is a measure for the ratio between the convective heat transfer and the conductive heat transfer

$$Nu_L = \frac{h}{\frac{\lambda}{L}} = \frac{h \cdot L}{\lambda}
 \tag{B.16}$$

with the convective heat transfer coefficient h , the thermal conductivity λ (see equation (B.8)) and a characteristic length L . The heat transfer coefficient h is defined as

$$h = \frac{q}{\Delta T} \quad (\text{B.17})$$

in $\text{W m}^{-2} \text{K}^{-1}$, describing the heat flux through the unit area of a surface with a temperature difference ΔT to a surrounding fluid.

In most cases the surface geometry is not just a plane plate, causing h to vary along the surface. Therefore an averaged convective heat transfer coefficient \bar{h} is used to calculate the averaged Nusselt number \overline{Nu}_L .

The Nusselt number

- ◇ is equal to the dimensionless temperature gradient at the surface, and it provides a measure of the convection heat transfer occurring at the surface.
The Nusselt number is to the thermal boundary layer what the friction coefficient is to the velocity boundary layer. [6]

The expression of \overline{Nu}_L for different geometries can be rather complicated and is often described by empirical functions. For forced convection \overline{Nu}_L depends on the Reynolds and Prandtl number, for natural convection \overline{Nu}_L depends on the Rayleigh and Prandtl number.

For the vertical wall component of AIDA we can assume that the geometry is close to a vertical heated plate, for which the following expression can be applied [6, p. 605, eq. 9.26]:

$$\overline{Nu}_L^v = \left(0.825 + \frac{0.387 Ra_L^{1/6}}{[1 + (0.492/Pr)^{9/16}]^{8/27}} \right)^2 \quad (\text{B.18})$$

For the horizontal wall components one can apply

$$\overline{Nu}_L^h = 0.14 * Ra_L^{\frac{1}{3}} + 0.27 * Ra_L^{\frac{1}{4}} \quad (\text{B.19})$$

If we paid respect to the case of mixed convection, meaning both forced and natural convection, \overline{Nu}_L would be a function of Re , Ra and Pr as independent variables [7, sec. 14.6].

B.3 Heat Flux Calculations

The heat flux between AIDA walls and gas is calculated as an incremental heat flux per timestep, which has a typical length of $\Delta t = 1$ s.

By inseting equation (B.17) into equation (B.16) and solving for q we receive a general expression for the heat flux

$$q = Nu_L \cdot \frac{\Delta T \cdot \lambda}{L} \quad (\text{B.20})$$

in $\text{J m}^{-2} \text{s}^{-1}$. Using the mean Nusselt numbers and most of the expressions from the previous sections the time resolved heat flux for the vertical and horizontal wall component result to

$$q^v = \left(0.825 + \frac{0.387 Ra_L^{1/6}}{[1 + (0.492/Pr)^{9/16}]^{8/27}} \right)^2 \cdot \frac{(T_w - T_g) \cdot \lambda}{L^v} \cdot A_{cyl}^v \cdot \Delta t \quad (\text{B.21})$$

$$q^h = \left(0.14 * Ra^{\frac{1}{3}} + 0.27 \cdot Ra_L^{\frac{1}{4}} \right) \cdot \frac{(T_w - T_g) \cdot \lambda}{L^h} \cdot A_{cyl}^h \cdot \Delta t. \quad (\text{B.22})$$

The sum of both terms is the total heat flux which we will scale with an additional empirical factor f to treat the fact, that the convective heat flux is not only driven by natural convection, but enhanced by an additional contribution of forced convection caused by the chambers mixing fan.

$$q^{tot} = f \cdot (q^v + q^h) \quad (\text{B.23})$$

Translating the transported heat to a temperature change in the chamber leads to

$$\delta T = \frac{q^{tot}}{c_p \cdot V \cdot \rho} \quad (\text{B.24})$$

For an AIDA expansion experiment we can argue that the deviation between the measured gas temperature profile and a pure adiabatic profile is driven by the heat flux from the walls. Hence we can say the sum of the adiabatic profile and the temperature change caused by the cumulative heat flux has to result in the chambers gas temperature. This assumption is used to fit the factor f , which typically results in values around 1.5 to 1.8.

B.4 Water Flux Calculation

The factor f , describing the enhancement of natural convection by forced convection, is also relevant to describe surface boundary layer conditions regarding the the water flux.

B.5 Sources of errors in this approach?

The characteristic lengths for the water flux from the horizontal and vertical walls are calculated as

$$L_w^v = \frac{L^v}{Nu_L^v \cdot f} \quad \text{and} \quad L_w^h = \frac{L^h}{Nu_L^h \cdot f} \quad (\text{B.25})$$

This approach is adopted from notes from Stefan Benz (2009) and code from Helmut Bunz (until 2008). A robust source needs to be looked up, yet.

The change in AIDA water vapor pressure caused by the water wall flux is then derived as

$$\delta p_w^v = \frac{D}{L_w^v} \cdot \left(\frac{Sc}{Pr} \right)^{\frac{1}{3}} \cdot (p_w^{gas} - p_w^{wall}) \cdot A_{iced}^v \cdot \Delta t \quad (\text{B.26})$$

$$\delta p_w^h = \frac{D}{L_w^h} \cdot \left(\frac{Sc}{Pr} \right)^{\frac{1}{3}} \cdot (p_w^{gas} - p_w^{wall}) \cdot A_{iced}^h \cdot \Delta t \quad (\text{B.27})$$

in Pa.

Since the fraction of AIDA walls being iced $f_{ice} = \frac{A_{iced}}{A}$ is an unknown parameter we can derive it by fitting the wall flux calculation to experimentally derived data with f_{iced} as fit parameter. Here we have to assume that the wall acts as the only sink or source of water. Every other effect (e.g. ice nucleating aerosol) affecting the water content in the chamber will falsify the fit of f_{iced} .

B.5 Sources of errors in this approach?

The presented approach makes a couple of assumptions which can be seen as sources of errors, The assumptions are listed as follows:

- ◇ Approximation of the AIDA geometry as cylinder
- ◇ The different surfaces are a coupled system. Can they really be treated independently?
- ◇ A mean value is currently used for the wall temperature. At least for the different surface party (vert./horiz.) one could use more accurate wall temperatures.
- ◇ According to Pruppacher and Klett [60] the parameterization for the diffusion coefficient is not valid below -40°C .
- ◇ The expression for the density in [equation \(B.12\)](#) is specified for dry air.

- ◇ How valid is the approach to calculate the water wall flux from sub-results of the heat flux calculations (factor f)

Appendix C

MAID validation for different wall flux implementations

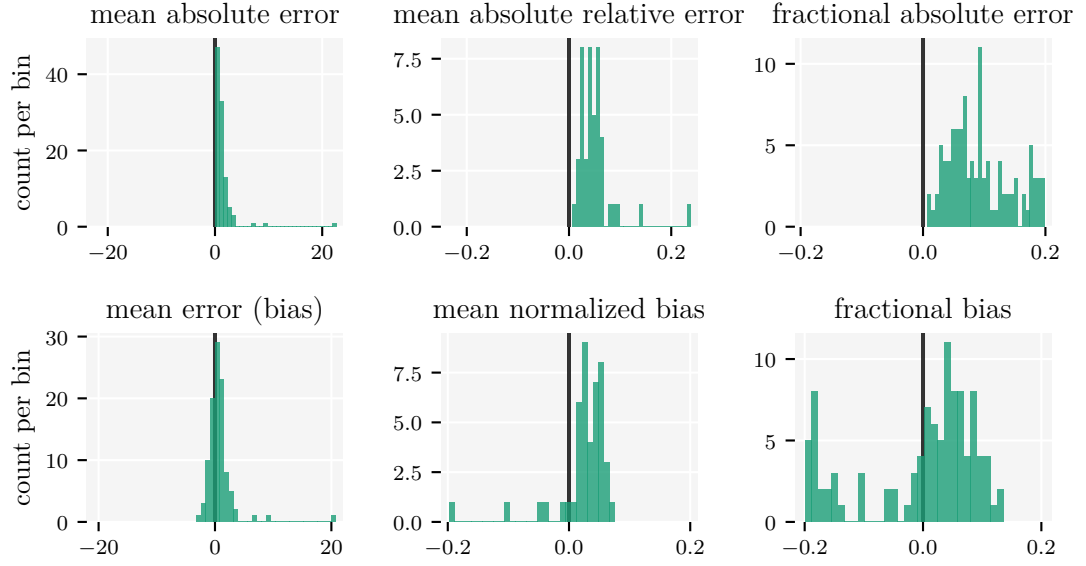
Here we provide additional figures for the comparison between [AIDA](#) expansion experiments and the [MAID](#) runs, which were conducted to reproduce the experiments. In [section 5.3](#) we showed a subset of these figures, which were derived using the fluid dynamic wall flux implementation in the model.

Here we show the evaluation statistics of the maximum ice number concentration n_{ice} and the maximum saturation ratio S_{ice} for model runs under all available wall flux representations. The wall flux representations include

- ◇ 'fluiddynamic': fluid dynamic approach, detailed description in [appendix B](#)
- ◇ 'Cotton2007': approach according to Cotton et al. [13]
- ◇ 'mbw': based on the change of the total water mixing ratio
- ◇ 'no_flux': without any water wall flux implementation

The different approaches are described in [section 3.5](#) and the metrics are described in [appendix A.1](#).

(MAID vs AIDA) metrics for n_{ice} , wall flux 'fluiddynamic'



(MAID vs AIDA) metrics for S_{ice} , wall flux 'fluiddynamic'

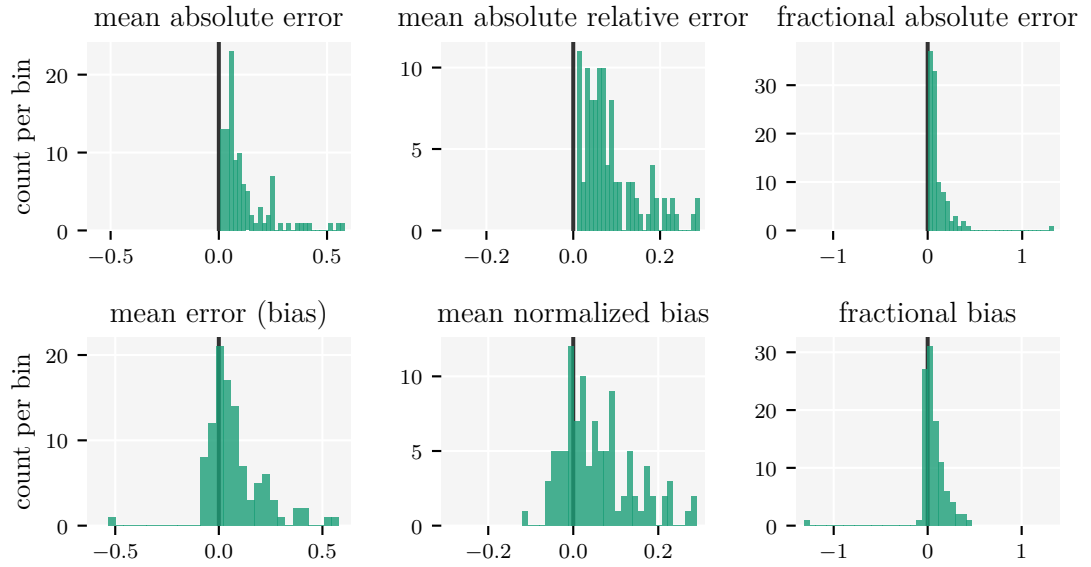
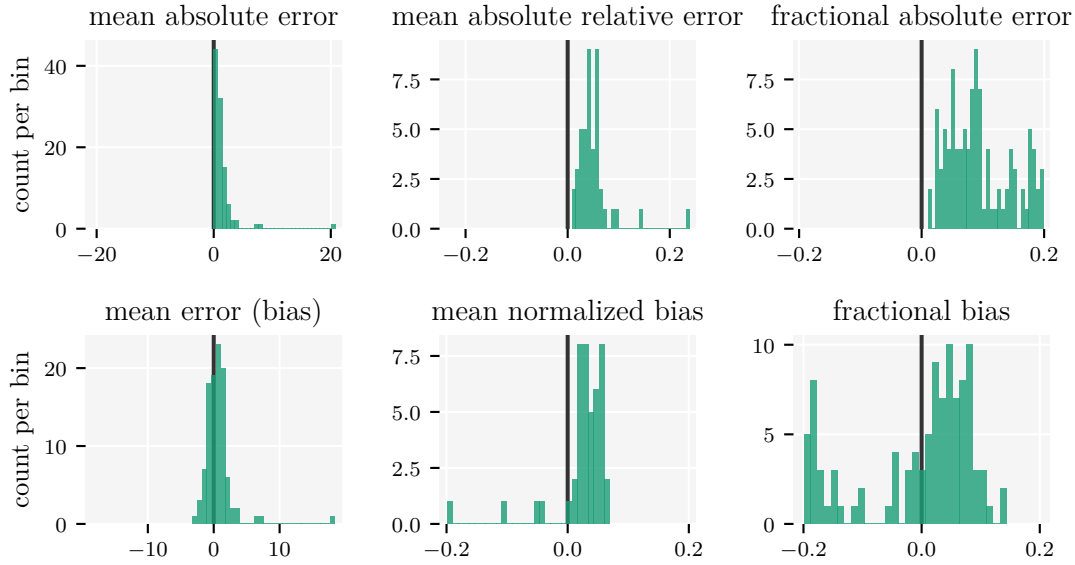


Figure C.0.1 Aggregated evaluation metrics about the deviation of the total ice crystal number concentration n_{ice} and S_{ice} between MAID results and AIDA experiments using the fluid dynamic wall flux implementation in the model. The abscissas in the first column of the upper subplot have the unit cm^{-3} , whereas all other abscissas are dimensionless. The upper half of the figure was already shown in section 5.3.2.

(MAID vs AIDA) metrics for n_{ice} , wall flux 'Cotton2007'



(MAID vs AIDA) metrics for S_{ice} , wall flux 'Cotton2007'

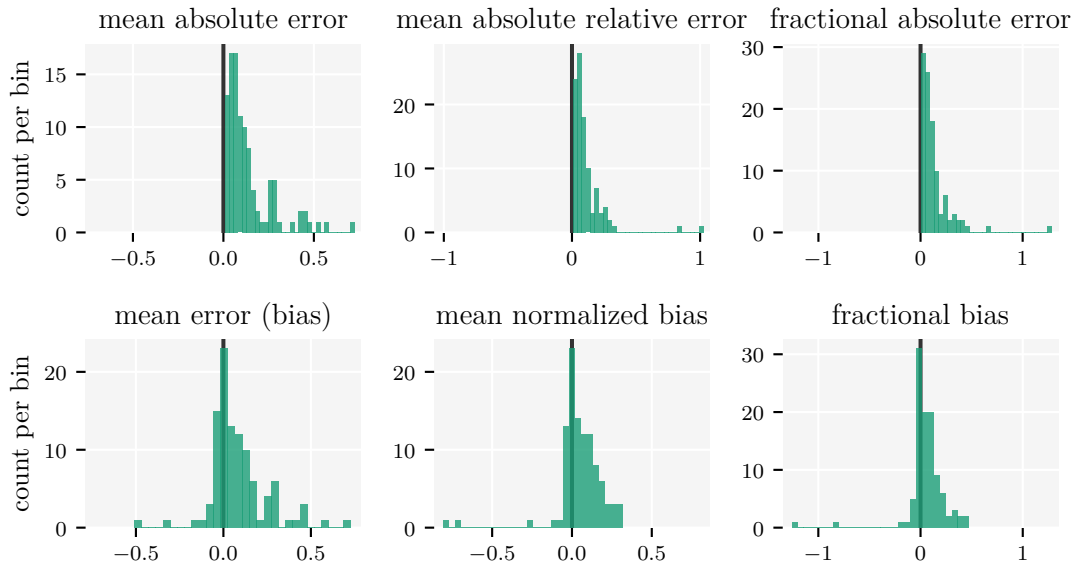
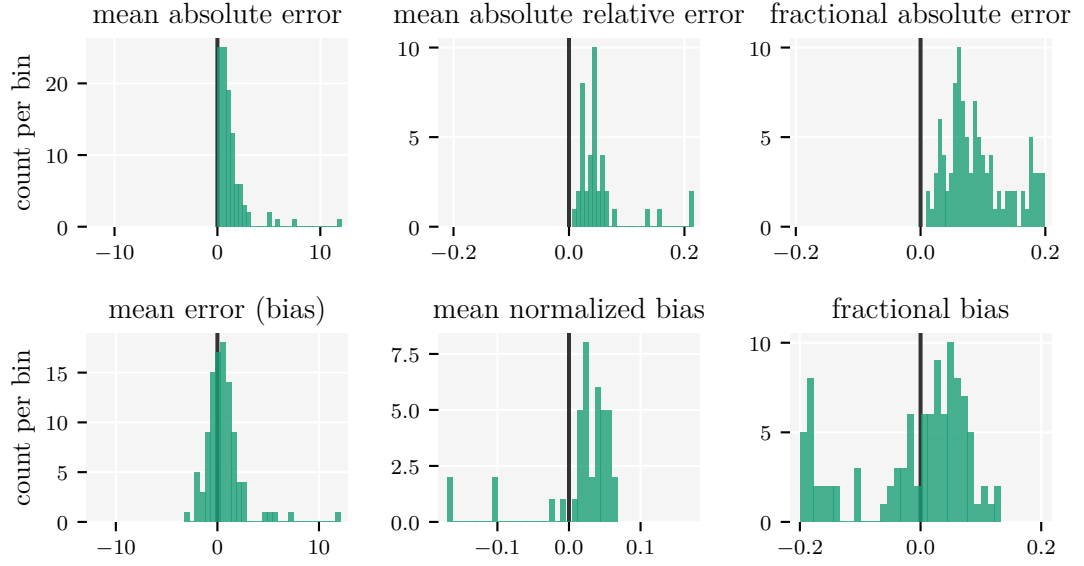


Figure C.0.2 Aggregated evaluation metrics about the deviation of the total ice crystal number concentration n_{ice} and S_{ice} between MAID results and AIDA experiments using the wall flux implementation according to Cotton et al. [13] in the model. The abscissas in the first column of the upper subplot have the unit cm^{-3} , whereas all other abscissas are dimensionless.

(MAID vs AIDA) metrics for n_{ice} , wall flux 'mbw'



(MAID vs AIDA) metrics for S_{ice} , wall flux 'mbw'

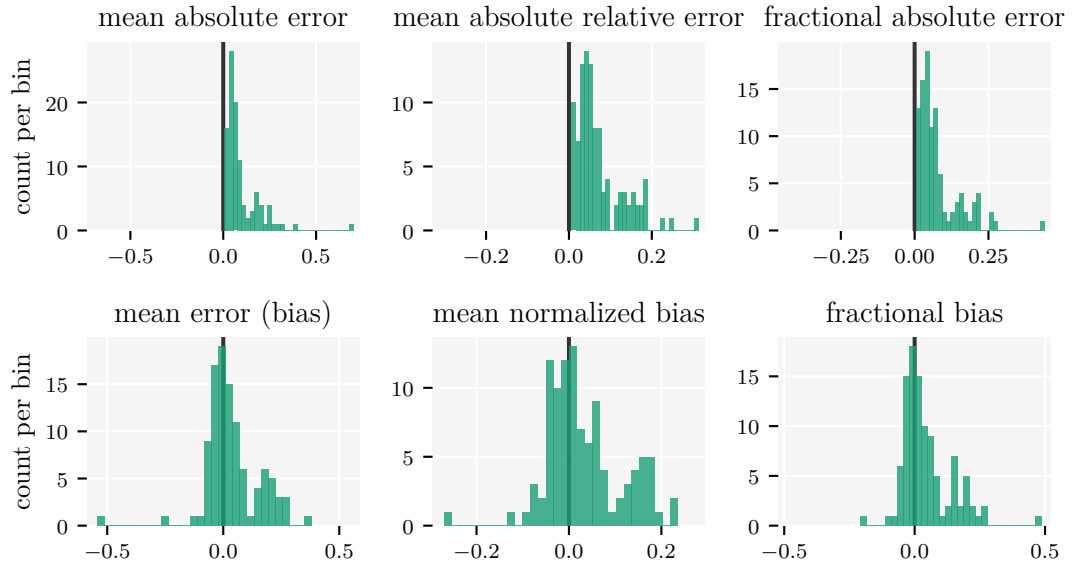
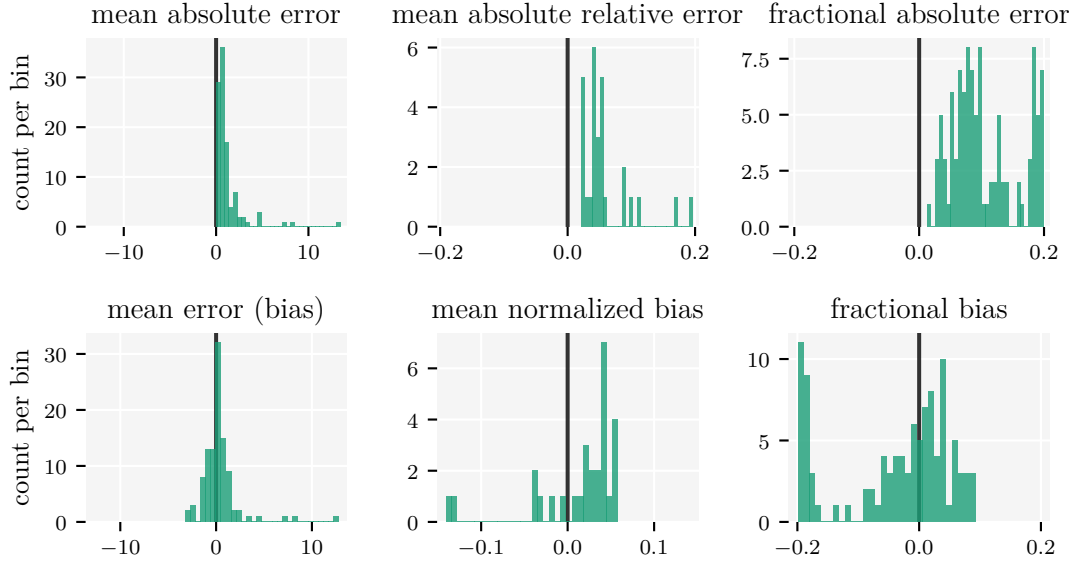


Figure C.0.3 Aggregated evaluation metrics about the deviation of the total ice crystal number concentration n_{ice} and S_{ice} between MAID results and AIDA experiments using the wall flux implementation based on the MBW variation in the model. The abscissas in the first column of the upper subplot have the unit cm^{-3} , whereas all other abscissas are dimensionless.

(MAID vs AIDA) metrics for n_{ice} , wall flux 'no_flux'



(MAID vs AIDA) metrics for S_{ice} , wall flux 'no_flux'

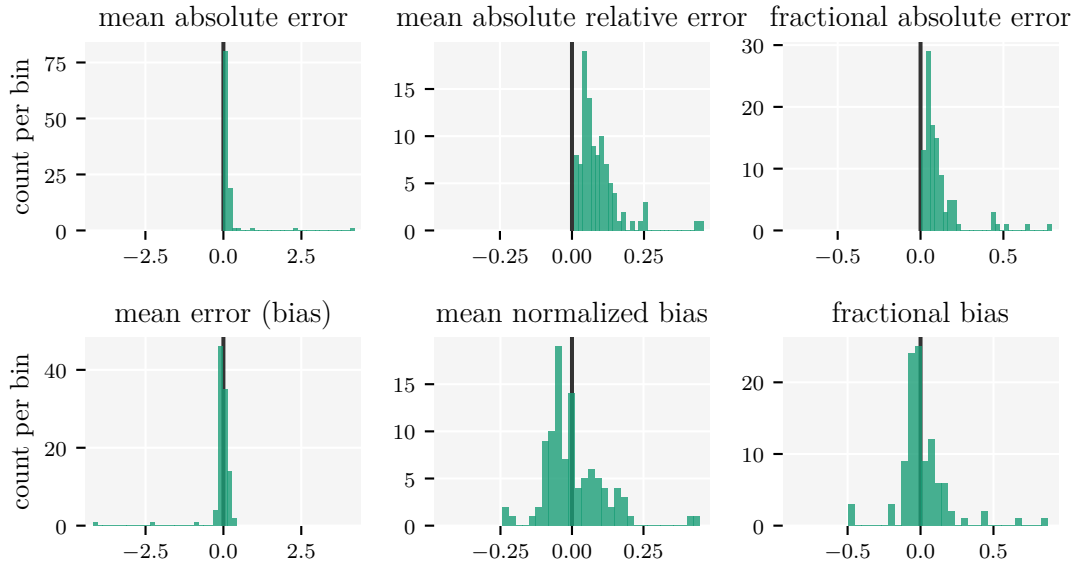


Figure C.0.4 Aggregated evaluation metrics about the deviation of the total ice crystal number concentration n_{ice} and S_{ice} between MAID results and AIDA experiments without any water wall flux consideration in the model. The abscissas in the first column of the upper subplot have the unit cm^{-3} , whereas all other abscissas are dimensionless.

Appendix D

Long tables

This chapter provides tables with additional information with importance for reproducibility, transparency and documentation.

Table D.0.1 Key information of expansion experiments conducted at the [AIDA](#) cloud chamber facility. The list excludes 'reference activations', which are quick expansions to clean ice-active contaminations from the chamber. A similar list for the reference activations can be found in [Table D.0.2](#). Note that this table provides unique information, which is not represented in the [AIDA](#) database. The database structure isn't designed to support multiple aerosol number concentrations and varying pump rates.

campaign	exp. num	exp. ID	temp. in K	aerosol type	n_{INP} in cm^{-3}	n_{ASP} in cm^{-3}	abs. timestamp in sec., rel. pump power
AWICIT01B	2	3591	210.2	IN_Sil	232	NaN	0, P2 80 %
AWICIT01B	3	3592	210.2	IN_Sil	264	NaN	0, P2 80 %
AWICIT01B	5	3594	210.2	IN_Sil	270	NaN	0, P2 50 %
AWICIT01B	6	3595	210.2	IN_Sil	60	NaN	0, P2 80 %
AWICIT01B	7	3596	210.7	IN_Sil	37	NaN	0, P2 50 %
AWICIT01B	9	3598	210.2	IN_H2SO4	NaN	680.0	0, P2 80 %
AWICIT01B	10	3599	210.7	IN_NXIllite	550	NaN	0, P2 80 %
AWICIT01B	11	3600	210.7	IN_NXIllite	125	NaN	0, P2 80 %
AWICIT01B	12	3601	219.8	IN_Sil	190	NaN	0, P2 80 %
AWICIT01B	13	3602	219.6	IN_Sil	230	NaN	0, P2 50 %
AWICIT01B	14	3603	219.9	IN_Sil	60	NaN	0, P2 80 %
AWICIT01B	15	3604	219.6	IN_Sil	14	NaN	0, P2 50 %
AWICIT01B	16	3605	220.6	IN_NXIllite	260	NaN	0, P2 80 %
AWICIT01B	17	3606	230.8	IN_Sil	190	NaN	0, P2 80 %
AWICIT01B	18	3607	230.6	IN_Sil	22	NaN	0, P2 80 %
AWICIT01B	20	3609	230.0	IN_H2SO4	NaN	410.0	0, P2 80 %
AWICIT01B	21	3610	230.1	IN_H2SO4_Sil	12	166.0	0, P2 80 %

Continued on next page

Table D.0.1 (Continued) Key information of expansion experiments conducted at the [AIDA](#) cloud chamber facility. The list excludes 'reference activations', which are quick expansions to clean ice-active contaminations from the chamber. A similar list for the reference activations can be found in [Table D.0.2](#). Note that this table provides unique information, which is not represented in the [AIDA](#) database. The database structure isn't designed to support multiple aerosol number concentrations and varying pump rates.

campaign	exp. num	exp. ID	temp. in K	aerosol type	n_{INP} in cm⁻³	n_{ASP} in cm⁻³	abs. timestamp in sec., rel. pump power
AWICIT01B	23	3612	229.8	IN_H2SO4_Sil	4	440.0	0, P2 80 %
AWICIT01B	25	3614	230.1	IN_H2SO4_Sil	20	195.0	0, P2 80 %
AWICIT01B	26	3615	229.3	IN_H2SO4_Sil	40	195.0	0, P2 80 %
AWICIT01B	27	3616	219.8	IN_H2SO4_Sil	28	252.0	0, P2 80 %
AWICIT01B	28	3617	219.8	IN_H2SO4_Sil	11	204.0	0, P2 80 %
AWICIT01B	30	3619	220.3	IN_H2SO4_Sil	16	408.0	0, P2 80 %
AWICIT01B	31	3620	209.8	IN_H2SO4_Sil	4.5	185.5	0, P2 80 %
AWICIT01B	32	3621	210.1	IN_H2SO4_Sil	9	176.0	0, P2 80 %
AWICIT01B	33	3622	210.4	IN_H2SO4_Sil	19	291.0	0, P2 80 %
AWICIT01B	34	3623	209.9	IN_H2SO4_Sil	7.5	37.5	0, P2 80 %
AWICIT01B	35	3624	209.8	IN_H2SO4_Sil	28	47.0	0, P2 80 %

Continued on next page

Table D.0.1 (Continued) Key information of expansion experiments conducted at the [AIDA](#) cloud chamber facility. The list excludes 'reference activations', which are quick expansions to clean ice-active contaminations from the chamber. A similar list for the reference activations can be found in [Table D.0.2](#). Note that this table provides unique information, which is not represented in the [AIDA](#) database. The database structure isn't designed to support multiple aerosol number concentrations and varying pump rates.

campaign	exp. num	exp. ID	temp. in K	aerosol type	n_{INP} in cm⁻³	n_{ASP} in cm⁻³	abs. timestamp in sec., rel. pump power
AWICIT01B	36	3625	210.5	IN_H2SO4_Sil	9	176.0	0, P2 100 % + MFC 25 qm/h 490, P2 100 % + MFC 50 qm/h 1030, P2 100 % + MFC 100 qm/h 1077, P2 100 % + MFC 95 qm/h 1110, P2 100 % + MFC 90 qm/h
AWICIT01B	37	3626	210.5	IN_H2SO4_Sil	9.5	62.5	0, P2 100 % + MFC 75 qm/h
AWICIT01B	39	3628	209.8	IN_H2SO4_Sil	18	432.0	0, P2 80 %
AWICIT01B	40	3629	210.4	IN_H2SO4_Sil	22	303.0	0, P2 80 %
AWICIT01B	41	3630	209.7	IN_H2SO4_Sil	18	192.0	0, P2 80 %
AWICIT01B	42	3631	220.0	IN_H2SO4	0	380.0	0, P2 80 %
AWICIT01B	43	3632	219.8	IN_H2SO4_Sil	19	54.0	0, P2 80 %
AWICIT01B	44	3633	220.2	IN_H2SO4_Sil	9	46.0	0, P2 80 %
AWICIT02	2	3693	230.0	IN_H2SO4_Sil	9	49.0	0, P2 50 %

Continued on next page

Table D.0.1 (Continued) Key information of expansion experiments conducted at the [AIDA](#) cloud chamber facility. The list excludes 'reference activations', which are quick expansions to clean ice-active contaminations from the chamber. A similar list for the reference activations can be found in [Table D.0.2](#). Note that this table provides unique information, which is not represented in the [AIDA](#) database. The database structure isn't designed to support multiple aerosol number concentrations and varying pump rates.

campaign	exp. num	exp. ID	temp. in K	aerosol type	n_{INP} in cm⁻³	n_{ASP} in cm⁻³	abs. timestamp in sec., rel. pump power
AWICIT02	3	3694	230.0	IN_H2SO4_Sil	5	28.0	0, P2 50 %
AWICIT02	4	3695	210.0	IN_H2SO4_Sil	5	25.0	0, P2 50 %
AWICIT02	5	3696	210.0	IN_H2SO4_Sil	9	49.0	0, P2 50 %
AWICIT02	6	3697	220.0	IN_H2SO4_Sil	11	46.0	0, P2 50 %
AWICIT02	7	3698	220.0	IN_H2SO4_Sil	27	51.0	0, P2 80 %
AWICIT02	8	3699	220.0	IN_H2SO4_Sil	4	26.0	0, P2 50 %
AWICIT02	9	3700	230.0	IN_H2SO4_Sil	5	47.0	0, P2 80 %
AWICIT02	10	3701	230.0	IN_H2SO4_Sil	9	50.0	0, P2 80 %
AWICIT02	11	3702	230.0	IN_H2SO4_Sil	20	46.0	0, P2 80 %
AWICIT03	1	3735	230.0	IN_H2SO4_Sil	20	NaN	0, P2 80 %
AWICIT03	2	3736	230.0	IN_H2SO4_Sil	10	50.0	0, P2 80 %
AWICIT03	3	3737	230.0	IN_H2SO4_Sil	6.5	25.0	0, P2 80 %
AWICIT03	4	3738	230.0	IN_H2SO4_Sil	10	25.0	0, P2 80 %
AWICIT03	6	3740	230.0	IN_H2SO4	NaN	47.0	0, P2 80 %
AWICIT03	8	3742	220.0	IN_H2SO4_Sil	4.5	26.5	0, P2 80 %
AWICIT03	9	3743	220.0	IN_H2SO4_Sil	12	44.0	0, P2 80 %

Continued on next page

Table D.0.1 (Continued) Key information of expansion experiments conducted at the [AIDA](#) cloud chamber facility. The list excludes 'reference activations', which are quick expansions to clean ice-active contaminations from the chamber. A similar list for the reference activations can be found in [Table D.0.2](#). Note that this table provides unique information, which is not represented in the [AIDA](#) database. The database structure isn't designed to support multiple aerosol number concentrations and varying pump rates.

campaign	exp. num	exp. ID	temp. in K	aerosol type	n_{INP} in cm⁻³	n_{ASP} in cm⁻³	abs. timestamp in sec., rel. pump power
AWICIT03	11	3745	220.0	IN_H2SO4	NaN	53.0	0, P2 80% + PB on 205, P2 80%
AWICIT03	12	3746	210.0	IN_H2SO4_Sil	14	49.0	0, P2 80%
AWICIT03	13	3747	210.0	IN_H2SO4_Sil	15	25.0	0, P2 80%
AWICIT03	15	3749	210.0	IN_H2SO4	NaN	40.0	0, P2 80%
AWICIT03	16	3750	210.0	IN_H2SO4_Sil	5	25.0	0, P2 80%
AWICIT03	18	3752	210.0	IN_H2SO4	NaN	185.0	0, P2 80% + NAUA explosion
AWICIT04	1	3862	293.0	IN_H2SO4_CaCO3	60	365.0	0, P2 80%
AWICIT04	2	3863	293.0	IN_H2SO4_CaCO3	27	5100.0	0, P2 80%
AWICIT04	4	3865	230.0	IN_CaCO3	94	NaN	0, P2 80%
AWICIT04	5	3866	230.0	IN_H2SO4_CaCO3	5	75.0	0, P2 80%
AWICIT04	6	3867	230.0	IN_H2SO4	NaN	124.0	0, P2 80% + PB on at start
AWICIT04	7	3868	230.0	IN_H2SO4	NaN	100.0	0, P2 80%
AWICIT04	8	3869	230.0	IN_H2SO4_CaCO3	9.5	45.5	0, P2 80%
AWICIT04	9	3870	230.0	IN_H2SO4_CaCO3	14.5	43.5	0, P2 80%
AWICIT04	10	3871	220.8	IN_CaCO3	95	NaN	0, P2 80%

Continued on next page

Table D.0.1 (Continued) Key information of expansion experiments conducted at the [AIDA](#) cloud chamber facility. The list excludes 'reference activations', which are quick expansions to clean ice-active contaminations from the chamber. A similar list for the reference activations can be found in [Table D.0.2](#). Note that this table provides unique information, which is not represented in the [AIDA](#) database. The database structure isn't designed to support multiple aerosol number concentrations and varying pump rates.

campaign	exp. num	exp. ID	temp. in K	aerosol type	n_{INP} in cm⁻³	n_{ASP} in cm⁻³	abs. timestamp in sec., rel. pump power
AWICIT04	11	3872	220.8	IN_H2SO4	NaN	98.0	0, P2 80 %
AWICIT04	12	3873	220.8	IN_H2SO4_CaCO3	20	54.0	0, P2 80 %
AWICIT04	13	3874	220.7	IN_H2SO4_CaCO3	50	50.0	0, P2 80 %
AWICIT04	15	3876	221.1	IN_H2SO4_CaCO3	36.5	48.5	0, P2 80 %
AWICIT04	16	3877	221.1	IN_CaCO3	100	NaN	0, P2 80 %
AWICIT04	17	3878	210.8	IN_H2SO4_CaCO3	12.5	47.5	0, P2 80 %
AWICIT04	18	3879	210.8	IN_CaCO3	98.5	NaN	0, P2 80 %
AWICIT04	19	3880	216.2	IN_H2SO4	NaN	110.0	0, P2 80 %
AWICIT04	20	3881	210.8	IN_H2SO4_CaCO3	25	53.0	0, P2 80 %
AWICIT04	21	3882	211.2	IN_H2SO4_CaCO3	17	47.0	0, P2 80 %
AWICIT04	22	3883	210.7	IN_H2SO4_Sil	5.5	47.0	0, P2 80 %
AWICIT04	23	3884	210.8	IN_H2SO4_Sil	11.5	48.5	0, P2 80 %
AWICIT04	24	3885	211.2	IN_CaCO3	114	NaN	0, P2 80 %
AWICIT04	26	3887	211.1	IN_H2SO4_CaCO3	19	49.0	0, P2 80 %
AWICIT04	27	3888	211.2	IN_H2SO4_CaCO3	10	47.5	0, P2 80 %
AWICIT04	28	3889	211.8	IN_H2SO4_CaCO3	5.5	51.5	0, P2 80 %
AWICIT04	29	3890	220.9	IN_H2SO4_CaCO3	19	103.0	0, P2 80 %

Continued on next page

Table D.0.1 (Continued) Key information of expansion experiments conducted at the [AIDA](#) cloud chamber facility. The list excludes 'reference activations', which are quick expansions to clean ice-active contaminations from the chamber. A similar list for the reference activations can be found in [Table D.0.2](#). Note that this table provides unique information, which is not represented in the [AIDA](#) database. The database structure isn't designed to support multiple aerosol number concentrations and varying pump rates.

campaign	exp. num	exp. ID	temp. in K	aerosol type	n_{INP} in cm⁻³	n_{ASP} in cm⁻³	abs. timestamp in sec., rel. pump power
AWICIT04	30	3891	221.7	IN_H2SO4_Sil	5	48.0	0, P2 80% + PB on 104, P2 80%
AWICIT04	31	3892	221.8	IN_H2SO4_Sil	10.5	51.0	0, P2 80%
AWICIT04	33	3894	230.8	IN_H2SO4_Sil	10	51.5	0, P2 80%
AWICIT04	34	3895	231.4	IN_H2SO4_Sil	15.5	49.0	0, P2 80%
AWICIT04	35	3896	232.2	IN_H2SO4_Sil	21.5	49.0	0, P2 80%
AWICIT04	36	3938	220.7	IN_H2SO4	NaN	48.0	0, P2 80%
AWICIT04	37	3939	230.4	IN_H2SO4	NaN	47.5	0, P2 80%
AWICIT05	1	3983	230.0	IN_BCR	100	0.0	0, P2 80%
AWICIT05	2	3984	230.0	IN_H2SO4	0	57.0	0, P2 80%
AWICIT05	3	3985	220.0	IN_BCR	99	0.0	0, P2 80%
AWICIT05	4	3986	220.0	IN_H2SO4	0	54.0	0, P2 80%
AWICIT05	6	3988	220.0	IN_Sil	45	0.0	0, P2 80%
AWICIT05	7	3989	210.0	IN_H2SO4	0	50.0	0, P2 80%
AWICIT05	8	3990	210.0	IN_H2SO4	0	52.0	0, P2 80%
AWICIT05	9	3991	210.0	IN_Sil	22	0.0	0, P2 80%
AWICIT05	10	3992	210.0	IN_H2SO4	0	50.0	0, P2 80%

Continued on next page

Table D.0.1 (Continued) Key information of expansion experiments conducted at the [AIDA](#) cloud chamber facility. The list excludes 'reference activations', which are quick expansions to clean ice-active contaminations from the chamber. A similar list for the reference activations can be found in [Table D.0.2](#). Note that this table provides unique information, which is not represented in the [AIDA](#) database. The database structure isn't designed to support multiple aerosol number concentrations and varying pump rates.

campaign	exp. num	exp. ID	temp. in K	aerosol type	n_{INP} in cm⁻³	n_{ASP} in cm⁻³	abs. timestamp in sec., rel. pump power
AWICIT05	11	3993	211.3	IN_H2SO4_Sil	6	48.0	0, P2 80 %
AWICIT05	13	3995	210.0	IN_H2SO4_Sil	2.5	48.5	0, P2 80 %
AWICIT05	14	3996	210.0	IN_H2SO4_Sil	2.5	2380.0	0, P2 80 %
AWICIT05	15	3997	220.0	IN_H2SO4	0	45.0	0, P2 80 %
AWICIT05	16	3998	231.1	IN_H2SO4	0	40.0	0, P2 80 %
AWICIT05	17	3999	230.0	IN_H2SO4_BCR	3.5	48.0	0, P2 80 %
AWICIT05	18	4000	230.0	IN_H2SO4_BCR	10	51.0	0, P2 80 %
AWICIT05	19	4001	230.0	IN_H2SO4_BCR	20	50.0	0, P2 80 %
AWICIT05	20	4002	230.0	IN_BCR	10.5	0.0	0, P2 80 %
AWICIT05	21	4003	220.0	IN_H2SO4_BCR	9	49.0	0, P2 80 %
AWICIT05	23	4005	220.0	IN_H2SO4_BCR	4	46.0	0, P2 80 %
AWICIT05	25	4007	220.0	IN_H2SO4_BCR	2.8	48.9	0, P2 80 %
AWICIT05	27	4009	220.0	IN_H2SO4_CaCO3	8.7	49.0	0, P2 80 %
AWICIT05	28	4010	220.0	IN_H2SO4_CaCO3	12	52.0	0, P2 80 %
AWICIT05	29	4011	210.0	IN_H2SO4_CaCO3	4	51.0	0, P2 80 %
AWICIT05	30	4012	210.0	IN_H2SO4_CaCO3	15	51.0	0, P2 80 %
AWICIT05	32	4014	210.0	IN_H2SO4	0	50.0	0, P2 80 %

Continued on next page

Table D.0.1 (Continued) Key information of expansion experiments conducted at the [AIDA](#) cloud chamber facility. The list excludes 'reference activations', which are quick expansions to clean ice-active contaminations from the chamber. A similar list for the reference activations can be found in [Table D.0.2](#). Note that this table provides unique information, which is not represented in the [AIDA](#) database. The database structure isn't designed to support multiple aerosol number concentrations and varying pump rates.

campaign	exp. num	exp. ID	temp. in K	aerosol type	n_{INP} in cm⁻³	n_{ASP} in cm⁻³	abs. timestamp in sec., rel. pump power
AWICIT05	34	4016	210.0	IN_H2SO4_BCR	20	50.0	0, P2 80 %
AWICIT05	35	4017	210.0	IN_H2SO4_BCR	5.5	47.0	0, P2 80 %
AWICIT05	36	4018	210.0	IN_H2SO4_BCR	3.5	47.5	0, P2 80 %
AWICIT05	40	4022	210.0	IN_BCR	19.5	0.0	0, P2 80 %
AWICIT05	43	4025	210.0	IN_H2SO4_BCR	1.3	47.4	0, P2 80 %
AWICIT05	44	4026	230.0	IN_H2SO4_BCR	4.2	46.0	0, P2 80 %
AWICIT05	45	4027	230.0	IN_Sil	29.5	0.0	0, P2 80 %
AWICIT05	47	4029	230.0	IN_H2SO4_Sil	3.5	51.0	0, P2 80 %
AWICIT05	49	4031	220.0	IN_H2SO4_Sil	3.7	51.3	0, P2 80 %
AWICIT05	50	4032	220.0	IN_H2SO4_Sil	4	50.0	0, P2 80 %
AWICIT05	52	4034	220.0	IN_H2SO4_Sil	2	48.0	0, P2 80 %
AWICIT06	1	4046	230.7	IN_CaCO3	14.5	0.0	0, P2 80 %
AWICIT06	2	4047	231.2	IN_H2SO4_CaCO3	3	47.0	0, P2 80 %
AWICIT06	3	4048	230.6	IN_H2SO4_CaCO3	15	48.0	0, P2 80 %
AWICIT06	4	4049	231.2	IN_H2SO4_CaCO3	30	48.0	0, P2 80 %
AWICIT06	5	4050	231.3	IN_H2SO4_CaCO3	48	50.0	0, P2 80 %
AWICIT06	7	4052	220.0	IN_H2SO4_BCR	20	49.5	0, P2 80 %

Continued on next page

Table D.0.1 (Continued) Key information of expansion experiments conducted at the [AIDA](#) cloud chamber facility. The list excludes 'reference activations', which are quick expansions to clean ice-active contaminations from the chamber. A similar list for the reference activations can be found in [Table D.0.2](#). Note that this table provides unique information, which is not represented in the [AIDA](#) database. The database structure isn't designed to support multiple aerosol number concentrations and varying pump rates.

campaign	exp. num	exp. ID	temp. in K	aerosol type	n_{INP} in cm⁻³	n_{ASP} in cm⁻³	abs. timestamp in sec., rel. pump power
AWICIT06	8	4053	220.0	IN_H2SO4_BCR	13.5	50.0	0, P2 80 %
AWICIT06	10	4055	220.0	IN_H2SO4_Sil	14.5	50.0	0, P2 80 %
AWICIT06	11	4056	210.0	IN_H2SO4_Sil	10	48.5	0, P2 80 %
AWICIT06	12	4057	210.0	IN_H2SO4_Sil	3.8	49.5	0, P2 80 %
AWICIT06	14	4059	210.0	IN_H2SO4_Sil	1.2	48.6	0, P2 80 %
AWICIT06	15	4060	210.0	IN_H2SO4_BCR	9.5	50.0	0, P2 80 %
AWICIT06	16	4061	210.0	IN_H2SO4_CaCO3	43	48.0	0, P2 80 %
AWICIT06	18	4063	210.0	IN_H2SO4_CaCO3	53	49.0	0, P2 80 %
TROPIC02	3	4333	230.0	IN_H2SO4_BCR	44.5	113.0	0, P2 80 % 330, P2 variation
TROPIC02	4	4334	230.0	IN_H2SO4	0	50.0	P2 100 % + variation 0, P2 50 %
TROPIC02	5	4335	230.0	IN_H2SO4	0	49.2	190, P2 60 % 300, P2 80 % 435, P2 variation
TROPIC02	7	4337	220.0	IN_H2SO4_BCR	10.5	49.0	0, P2 100 % 210, P2 50 % + variation 1230, FC 10qm/h refill

Continued on next page

Table D.0.1 (Continued) Key information of expansion experiments conducted at the [AIDA](#) cloud chamber facility. The list excludes 'reference activations', which are quick expansions to clean ice-active contaminations from the chamber. A similar list for the reference activations can be found in [Table D.0.2](#). Note that this table provides unique information, which is not represented in the [AIDA](#) database. The database structure isn't designed to support multiple aerosol number concentrations and varying pump rates.

campaign	exp. num	exp. ID	temp. in K	aerosol type	n_{INP} in cm⁻³	n_{ASP} in cm⁻³	abs. timestamp in sec., rel. pump power
TROPIC02	9	4339	220.0	IN_H2SO4_BCR	1.7	46.6	0, P2 60 % 270, P2 50 % + variation
TROPIC02	10	4340	220.0	IN_H2SO4_BCR	1.2	48.8	0, P2 60 %
TROPIC02	12	4342	210.0	IN_H2SO4_BCR	4	52.5	0, P2 100 % 330, P2 50 % + variation
TROPIC02	13	4343	210.0	IN_H2SO4_BCR	1.4	52.6	0, P2 60 % 360, P2 70 % 450, P2 80 % 480, P2 85 % 660, P2 50 % + variation
TROPIC02	14	4344	210.0	IN_H2SO4	0.3	50.0	0, P2 100 %
TROPIC02	16	4346	200.0	IN_H2SO4_BCR	1	42.5	0, P2 60 % 480, P2 70 % 540, P2 80 %
TROPIC02	18	4348	200.0	IN_BCR	13	0.0	0, P2 60 % + variation 330, P2 65 %
TROPIC02	19	4349	220.0	IN_H2SO4_BCR	16	50.0	0, P2 100 %
TROPIC02	22	4352	220.0	IN_H2SO4_Bkgd	1.5	50.5	0, P2 70 % 360, P2 50 %

Continued on next page

Table D.0.1 (Continued) Key information of expansion experiments conducted at the [AIDA](#) cloud chamber facility. The list excludes 'reference activations', which are quick expansions to clean ice-active contaminations from the chamber. A similar list for the reference activations can be found in [Table D.0.2](#). Note that this table provides unique information, which is not represented in the [AIDA](#) database. The database structure isn't designed to support multiple aerosol number concentrations and varying pump rates.

campaign	exp. num	exp. ID	temp. in K	aerosol type	n_{INP} in cm⁻³	n_{ASP} in cm⁻³	abs. timestamp in sec., rel. pump power
TROPIC02	23	4353	210.0	IN_H2SO4_BCR	2.2	49.8	0, P2 70 % 480, P2 50 %
TROPIC02	24	4354	210.0	IN_H2SO4	0.2	52.0	0, P2 60 % 540, P2 reduced power
TROPIC02	25	4355	210.0	IN_H2SO4_BCR	12	50.0	0, P2 100 %
TROPIC02	26	4356	205.0	IN_H2SO4	0	49.0	0, P2 80 % 330, P2 50 %
TROPIC02	27	4357	205.0	IN_H2SO4	0	50.0	0, P2 100 %
TROPIC02	28	4358	205.0	IN_H2SO4_BCR	4	45.0	0, P2 78 % 401, P2 50 %
TROPIC02	29	4359	230.0	IN_H2SO4_BCR	3	49.0	0, P2 60 % 208, P2 70 % 253, P2 80 % 510, P2 50 %
TROPIC02	30	4360	220.0	IN_H2SO4	0	47.0	0, P2 100 % 295, P2 50 % 640, P2 60 %
TROPIC02	31	4361	205.0	IN_H2SO4_Bkgd	1.4	51.6	0, P2 70 % 370, P2 50 %

Continued on next page

Table D.0.1 (Continued) Key information of expansion experiments conducted at the [AIDA](#) cloud chamber facility. The list excludes 'reference activations', which are quick expansions to clean ice-active contaminations from the chamber. A similar list for the reference activations can be found in [Table D.0.2](#). Note that this table provides unique information, which is not represented in the [AIDA](#) database. The database structure isn't designed to support multiple aerosol number concentrations and varying pump rates.

campaign	exp. num	exp. ID	temp. in K	aerosol type	n _{INP} in cm ⁻³	n _{ASP} in cm ⁻³	abs. timestamp in sec., rel. pump power
TROPIC02	33	4363	205.0	IN_H2SO4_BCR	13.6	52.0	0, P2 100 % 315 P2 50 % 360, P2 40 % 475, P2 small variations
TROPIC02	35	4365	205.0	IN_H2SO4_BCR	0.5	46.5	0, P2 60 %

Source: This table is derived from the spreadsheet *exp_concentrations.ods* which can be found in the AWICIT-specific branch of the [aida_experiment_analysis](#) git repository [69].

Table D.0.2 Key information of reference expansion experiments conducted at the [AIDA](#) cloud chamber facility. In addition to their initial purpose removing ice-active background contaminations from the chamber, they were also used as a reference to fit the water vapor fluxes between ice-covered parts of the chamber wall and the gas phase. This table complements [Table D.0.1](#), which contains all other expansions with a scientific objective.

campaign	exp. num.	exp. ID	temp. in K	abs. timestamp in sec., rel. pump power
AWICIT01B	1	3590	210.2	0, P2 80 %
AWICIT01B	4	3593	NaN	0, P2 80 %
AWICIT01B	8	3597	210.0	0, P2 80 %
AWICIT01B	19	3608	230.3	0, P2 80 %
AWICIT01B	22	3611	NaN	0, P2 80 %
AWICIT01B	24	3613	NaN	0, P2 80 %
AWICIT01B	29	3618	NaN	0, P2 80 %
AWICIT01B	38	3627	210.0	0, P2 80 %
AWICIT02	1	3692	230.0	0, P2 80 %
AWICIT03	5	3739	230.0	NaN
AWICIT03	7	3741	220.0	NaN
AWICIT03	10	3744	220.0	NaN
AWICIT03	14	3748	210.0	NaN
AWICIT03	17	3751	210.0	NaN
AWICIT04	3	3864	230.0	0, P2 100 %
AWICIT04	14	3875	221.1	0, P2 100 %
AWICIT04	25	3886	210.0	0, P2 100 %
AWICIT04	32	3893	230.0	0, P2 100 %
AWICIT05	5	3987	220.0	NaN
AWICIT05	12	3994	210.0	0, P2 100 %
AWICIT05	22	4004	220.0	0, P2 100 %
AWICIT05	24	4006	220.0	0, P2 100 %
AWICIT05	26	4008	220.0	0, P2 100 %
AWICIT05	31	4013	210.0	0, P2 100 %
AWICIT05	33	4015	210.0	0, P2 100 %
AWICIT05	37	4019	210.0	0, P2 100 %

Continued on next page

Table D.0.2 (Continued) Key information of reference expansion experiments conducted at the AIDA cloud chamber facility. In addition to their initial purpose removing ice-active background contaminations from the chamber, they were also used as a reference to fit the water vapor fluxes between ice-covered parts of the chamber wall and the gas phase. This table complements Table D.0.1, which contains all other expansions with a scientific objective.

campaign	exp. num.	exp. ID	temp. in K	abs. timestamp in sec., rel. pump power
AWICIT05	38	4020	210.0	0, P2 80 %
AWICIT05	39	4021	210.0	0, P2 100 %
AWICIT05	41	4023	210.0	0, P2 100 %
AWICIT05	42	4024	210.0	0, P2 100 %
AWICIT05	46	4028	230.0	0, P2 100 %
AWICIT05	48	4030	220.0	0, P2 100 %
AWICIT05	51	4033	220.0	0, P2 100 %
AWICIT06	6	4051	220.0	0, P2 100 %
AWICIT06	9	4054	220.0	0, P2 100 %
AWICIT06	13	4058	210.0	0, P2 100 %
AWICIT06	17	4062	210.0	0, P2 100 %
TROPIC02	1	4331	230.0	NaN
TROPIC02	2	4332	230.0	NaN
TROPIC02	6	4336	220.0	0, P2 100 %
TROPIC02	8	4338	220.0	0, P2 100 %
TROPIC02	11	4341	210.0	0, P2 100 % + P.B. on 175, P2 100 %
TROPIC02	15	4345	200.0	0, P2 100 %
TROPIC02	17	4347	200.0	0, P2 100 %
TROPIC02	20	4350	220.0	0, P2 100 %
TROPIC02	21	4351	220.0	0, P2 100 %
TROPIC02	32	4362	205.0	0, P2 100 %
TROPIC02	34	4364	205.0	0, P2 100 %

Source: This table is derived from the spreadsheet *exp_concentrations.ods* which can be found in the AWICIT-specific branch of the *aida_experiment_analysis* git repository.